UNIVERSITY OF CALIFORNIA

Los Angeles

Improvements and Applications of Multiparametric Mapping with Magnetic Resonance Multitasking

A dissertation submitted in partial satisfaction of the requirements for the degree Doctor of Philosophy in Bioengineering

by

Tianle Cao

2023

ABSTRACT OF THE DISSERTATION

Improvements and Applications of Multiparametric Mapping
with Magnetic Resonance Multitasking

by

Tianle Cao
Doctor of Philosophy in Bioengineering
University of California, Los Angeles, 2023
Professor Debiao Li, Chair

Current clinical magnetic resonance (MR) acquisitions primarily rely on qualitative or 'weighted' images and diagnosis is made by subjective assessment of regional signal intensity (hyperintense or hypointense). However, MR signal for the same material can vary due to different scanners and different protocols, which hinders objective evaluation of disease severity. In contrast, quantitative MRI provides objective information for tissue characterization, offering enhanced inter-session and inter-site reproducibility. It enables improved pathology detection and disease monitoring and has better sensitivity to mild or diffuse tissue alterations compared to qualitative imaging. The combination of multiple biomarkers provides more comprehensive information and shows great promise for risk assessment and early detection.

Despite these advantages, the clinical application of multiparametric MRI has been limited due to the prolonged scan times for acquiring different biomarkers, motion artifacts, and

misregistration between parametric maps. MR Multitasking presents a promising approach for motion-resolved, multi-parametric mapping. However, it has yet to exploit the multi-echo information (magnitude and phase) for T_2*, susceptibility, and fat fraction mapping, which necessitates further technical development. This includes flow compensation for more accurate susceptibility mapping, achieving adequate temporal resolution for motion tracking, and improving imaging efficiency for multi-echo readouts. In addition, MR Multitasking demands further improvement in quantitative performance (precision and repeatability) and scan time for practical applications.

The dissertation will be focused on technical developments of MR Multitasking to enable comprehensive tissue characterization and to improve quantitative performance. The first objective is to develop a technique for three-dimensional, whole-brain simultaneous T_1, T_2, T_2*, and susceptibility mapping. The proposed method is evaluated on phantoms and human subjects. The second objective involves further technical development to achieve free-breathing, non-ECG, simultaneous myocardial T_1, T_2, T_2*, and FF mapping in a 2.5-min scan. Lastly, a novel reconstruction approach is introduced to improve precision and repeatability and shorten scan time. The approach is evaluated with numerical simulations and healthy subjects.

The dissertation represents a step toward motion-resolved, comprehensive tissue characterization within a clinically feasible scan time and without the need for extra physiological monitoring. It lays the groundwork for future clinical use of quantitative multiparametric MRI.

The dissertation of Tianle Cao is approved.

Holden H. Wu

Kim-Lien Nguyen

Anthony G. Christodoulou

Yibin Xie

Debiao Li, Committee Chair

University of California, Los Angeles

2023

Dedicated to the ones who supported and inspired me in my youth:

My beloved parents: Xinfang Cao and Yu Cai

My respected teachers: Qiang Li, Guoqing Han, Peng He, and Ping Wang.

I wouldn't have made it this far without your help.

TABLE OF CONTENTS

LIST OF FIGURES

LIST OF TABLES

ACKNOWLEDGEMENTS

The past five years has been an extensive yet fulfilling journey in my life, and I hope to express my deepest gratitude to many people for their unconditional support.

I am incredibly fortunate to be mentored by Dr. Debiao Li, a true luminary in the field of MRI research. I have always been impressed and influenced by his passion, dedication, and profound insights. He is an exceptional mentor who provided me with invaluable research skills and granted me the freedom to explore and grow, especially in the past two years. His commitment to fostering a collaborative environment within our institute, to providing abundant resources and to simplifying research workflows, has paved the way for the smooth advancement of my projects.

I wish to extend my heartfelt appreciation to Dr. Anthony G. Christodoulou, whose expertise and patience have been invaluable to me. Anthony has the most solid knowledge and skills in signal processing and MR physics among all people I have ever met. He shared with me his insights and knowledge, providing me the opportunity to solve MRI challenges using math tools -- something I have been looking forward to since my early days as a junior student. I am also grateful for Anthony's ongoing support in my future career and for his encouraging feedback throughout the journey. Although never officially documented, Anthony has been another mentor to me. and I will forever cherish the delightful memories of the moments we spent discussing research and debugging code together.

During my time as a junior student in the university, I got the chance to visit Debiao's lab and to attend the group meeting, where I met Dr. Yibin Xie. I expected such encounters to be routine for prospective students, yet I was pleasantly surprised when Yibin recognized me upon joining the group the following year. Throughout my PhD, Yibin has been a supportive elder brother, always ready to offer guidance whenever I had questions. His profound knowledge in MRI and

expertise in sequence programming make him the first person I would talk to whenever I encountered issues with my sequences. I am deeply thankful to all his invaluable guidance.

I would like to thank Dr. Holden H. Wu, my former instructor at UCLA for MRI courses and my current committee members. As a student, I enjoyed Holden's classes for the clarity, conciseness, and involvement. I still find myself referring to many of his previous slides even today. As a committee member, Holden also provided helpful suggestions and insightful discussions, which significantly benefited my project and my thesis.

Though Dr. Kim-Lien Ngyuen and I have known each other for the shortest time among all my committee members, she has offered me as much support and mentorship. Lien provided opportunities to validate my technique on patients and offered invaluable assistance in designing studies, both of which played a crucial role in revising my papers. Beyond her clinical expertise, she generously offered me valuable suggestions about potential career paths. Lien's warm and approachable demeanor made her a pleasure to work with, and I deeply appreciate her kind assistance, not only in research matters but also in other aspects, like offering to route the e-form via her Adobe Acrobat account when we were working on the committee reconstitution form.

Many thanks to Dr. Ruan Dan, Dr. Peng Hu, and Dr. Kyung Sung, who were my instructors at UCLA, for their excellent jobs in teaching. I hope to give special thanks to Dr. Kyung Sung. He mentored my summer internship and offered all his patience and support to someone who had little knowledge about MRI at that time. He also provided valuable advice that has guided my career and my life.

I feel privileged to have collaborated with the brilliant minds at Biomedical Imaging Research Institute, including fellow graduate students (Xinheng Zhang, Shihan Qiu, Zihao Chen, Chaowei Wu, Haoran Sun, Karandeep Cheema, Zheyuan Hu, and Zengtian Deng), past students (Dr. Zhehao

Hu, Dr. Pei Han, Dr. Sen Ma, Dr. Nan Wang, Dr. Yuhua Chen, Dr. Zhengwei Zhou, and Dr. Jaime Shaw), postdoctoral scientists (Dr. Hsu-Lei Lee, Dr. Xianglun Mao who is now with GE, Dr. Lingceng Ma, and Dr. Xi Chen), faculties (Dr. Zhaoyang Fan who is now with USC, Dr. Ivan Cokic, Dr. Alan Kwan, Dr. Janet Wei, and Dr. Hsin-Jung Yang), MRI technologists (Laura Smith, Edward Gill, Irene Lee, and Mike Ngo), and our support research staffs (Joceline Mota, Grant Dagliyan, Natalin Aroyan, De Leon Rosalia, Kelli Dejohn, Marsia Lopez, Laura Chey, Catherine Ubaldo-Prado, Hyae Lee, Adis Asaturyan, and Ryan Goodcase). I must offer a special thanks to Xinheng for teaching me how to make a phantom and generously sharing his own with me. I also hope to acknowledge Sen and Nan, who have continuously offered me invaluable assistance in research and life matters since I joined the lab. And I have always enjoyed the fruitful discussions with Lei.

Finally, I owe a debt of gratitude to my parents, Xinfang Cao and Yu Cai, who brought me to this world and support me throughout my life. I also cherish the companionship of my beloved sister, Wenting Cai, who has been there for me since my early years.

VITA

Education:

- M.S., Department of Bioengineering, University of California, Los Angeles (2020)
- B.S., Department of Biomedical Engineering, Tsinghua University, Beijing, China (2018)

Journal Publications:

- **Cao T**, Wang N, Kwan AC, Lee HL, Mao X, Xie Y, Nguyen KL, Colbert CM, Han F, Han P, Han H. Free-breathing, non-ECG, simultaneous myocardial T1, T2, T2*, and fat-fraction mapping with motion-resolved cardiovascular MR multitasking. Magnetic Resonance in Medicine. 2022 Oct;88(4):1748-63.
- **Cao T**, Ma S, Wang N, Gharabaghi S, Xie Y, Fan Z, Hogg E, Haacke EM, Tagliati M, Christodoulou AG, Li D. Three-dimensional Simultaneous Brain Mapping of T1, T2, T2*, and Magnetic Susceptibility with MR Multitasking. Magnetic Resonance in Medicine. 2021 Oct 27.
- Sheagren C, **Cao T**, Patel J, Chen Z, Lee HL, Christodoulou AG, Wright G, Motion-Compensated T1 Mapping in Cardiovascular Magnetic Resonance Imaging: A Technical Review. Frontiers in Cardiovascular Medicine, In Press.
- Wang N, **Cao T**, Han F, Xie Y, Zhong X, Ma S, Kwan A, Fan Z, Han H, Bi X, Noureddin M. Free breathing multitasking multi-echo MRI for whole-liver water-specific T1, proton density fat fraction, and R2* quantification. Magnetic Resonance in Medicine. 2021 Aug 21.
- Mao X, Lee HL, Hu Z, **Cao T**, Han F, Ma S, Serry F, Fan Z, Xie Y, Christodoulou AG, Li D. Simultaneous Multi-slice Cardiac MR Multitasking for Motion-Resolved, Non-ECG, Free-Breathing T1-T2 Mapping. Frontiers in Cardiovascular Imaging. 2022 Mar 4.

- Han P, Cheema K, Lee HL, Zhou Z, **Cao T**, Ma S, Wang N, Han H, Christodoulou AG, Li D. Whole-brain steady-state CEST at 3 T using MR Multitasking. Magnetic Resonance in Medicine. 2021 Nov 29.
- Han P, Cheema K, **Cao T**, Lee HL, Han F, Wang N, Han H, Xie Y, Christodoulou AG, Li D. Free-breathing 3D CEST MRI of human liver at 3.0 T. Magnetic Resonance in Medicine. 2023 Feb 1.

Selected Conference Proceedings:

- Simultaneous quantitative mapping of T1, R2* and susceptibility with magnetic resonance multitasking. In Proceedings of the Annual Meeting of ISMRM, Paris, France, 2020. Abstract 0881.
- Non-ECG, free-breathing T1/T2/T2*/fat-fraction mapping for comprehensive myocardial tissue characterization with MR Multitasking. In Proceedings of 25th Annual SCMR International Conference, Virtual meeting, 2022. Abstract 180.
- Alternating Low-Rank Tensor Reconstruction for Improved Multi-Dimensional MRI with MR Multitasking. In Proceedings of the Annual Meeting of ISMRM, Toronto, Canada, 2023. Abstract 5881.

Recognitions:

- Young Investigator Award 1st place, Overseas Chinese Society of MRM (OCSMRM)

June 2023

- Editorial's pick of October, MRM

Oct 2022

- Early Career Award, Society for CMR (SCMR)

Feb 2022

CHAPTER 1 Introduction

1.1 Motivation

1.1.1 Qualitative MRI

MRI offers flexible tissue contrast and has become a fundamental tool for clinical diagnosis. In current practice, clinicians and radiologists typically read and analyze various contrast weighted images, such as T_1-weighted, T_2-weighted, and/or diffusion-weighted images, to identify hyperintense or hypointense regions, as focal pathologies often manifest with distinctive contrast from surrounding normal tissues. However, there are certain limitations associated with this routine: 1) Identifying diffuse diseases becomes challenging since all the imaged tissue will have similar contrast in such cases; 2) The contrast-weighted images lack quantifiable units, hindering longitudinal tracking of disease and treatment; 3) Qualitative MRI has limited sensitivity to subtle tissue alterations, especially during the early stages of pathology.

1.1.2 Quantitative and multi-parametric MRI

In contrast, quantitative MRI directly measures underlying tissue properties and is promising for objective tissue characterization and disease diagnosis. Parametric mapping of T_1 , T_2 , and T_2* is capable of detecting fibrosis (1, 2), edema (3-5), and iron overload (6). As a novel biomarker, susceptibility has gained increased interest and shows superior sensitivity and specificity than T_2* in differentiating patients with multiple sclerosis (7), Parkinson's disease (8), and glioblastoma (9) from healthy controls. Finally, fibro-fatty infiltration is a sign for arrhythmogenic right ventricular dysplasia (ARVD), and is also evident in chronic myocardial infarction (MI) and other nonischemic cardiomyopathies (10), which has motivated research on water/fat imaging and fat fraction mapping. Combination of multiple parameters can further enhance diagnostic

performance and sensitivity to tissue alterations. For instance, combining R_2* and fractional anisotropy has been show to enhance the sensitivity and specificity in differentiating Parkinson's disease (PD) patients from healthy controls (11). while the combination of T_1, T_2, and $T_{1\rho}$ offers superior diagnostic accuracy for multiple sclerosis patients (12). In cardiac imaging, the combination of native T_1, T_2, and extracellular volume fraction (ECV) has shown predictive value for acute cardiac allograft rejection (13).

1.1.3 Technical challenges of multi-parametric MRI

Despite potential benefits of multi-parametric MRI, certain technical challenges remain to be addressed before wider applications in the clinical routine. At present, multiparametric mapping typically requires separate scans for separate biomarkers. In some cases, even a single parameter may require multiple scans to collect sufficient data for fitting a signal model. The need for comprehensive tissue characterization may result in significantly prolonged scan time and complicated imaging workflows, which is not feasible in a clinical routine considering patient care and cost. Inter-scan misregistration/motion can lead to misaligned maps, complicating post-processing workflows and hampering joint analysis of multiple parameters. Physiological motion, such as respiratory and cardiac motion, can introduce motion artifacts, necessitating breath-holding, and ECG gating (retrospective or prospective) for studying moving organs such as liver and heart. In addition, random movements can also happen for static organs like brain (14). The resulting blurring and ghosting artifacts may lead to a loss of valuable diagnostic information.

Recent technical developments have enabled simultaneous, multiparametric mapping in brain (15-20), myocardium (21-23), and other organs. However, these techniques generally cannot handle motion (15, 16, 18-21) or can only handle part of the motion (e.g. respiratory motion only) (22, 23). The MR Multitasking framework, which leverages spatial and temporal correlations using

low-rank tensor (LRT) constraints, is a promising technique for fully motion-resolved, multi-parametric mapping. It was originally proposed for free-breathing, non-ECG myocardial T_1 and T_2 mapping (24) and has been extended for a wider range of applications including simultaneous brain T_1, T_2, apparent diffusion coefficient (ADC) mapping (25) and abdomen DCE imaging (26). However, extraction of T_2*, susceptibility, and fat fraction using MR Multitasking remains unexplored, and further improvements are needed to achieve quantitative performance and scan times comparable to clinical standards.

1.2 Objective

To overcome the limitations of conventional techniques and recent techniques, we aim to work towards a motion-resolved, multi-parametric mapping technique that enables comprehensive tissue characterization, provides reliable quantitative measurements, and is feasible in a clinical routine. As a starting point towards this long-term goal, this dissertation covers technical developments including:

1) The development a 3D whole-brain simultaneous T_1, T_2, T_2*, and susceptibility mapping method using MR Multitasking and validations on phantoms and healthy subjects. The work enables extraction of multi-echo information and potentially facilitates comprehensive tissue characterization.

2) The development of a free-breathing, non-ECG, simultaneous myocardial T_1, T_2, T_2*, and fat-fraction mapping technique and evaluate it on static and motion phantoms and on human subjects. It retains the motion-resolving capability of Multitasking framework with multi-echo readouts and makes technical improvements to keep a clinically feasible scan time.

3) The development of a novel low-rank tensor reconstruction method to improve quantification and acquisition time of cardiovascular MR Multitasking, evaluated with numerical simulations

and healthy subjects. The technique achieves significantly better precision and repeatability compared to the previous approach and will improve clinical translations of MR Multitasking.

1.3 Organization of the Dissertation

CHAPTER 2 provides introductions for commonly used tissue parameters in MRI and classical approaches for quantifying different biomarkers. It also reviews previous technical developments on simultaneous multi-parametric mapping and discusses the potential limitations. Finally, it gives a general introduction to the MR Multitasking framework.

CHAPTER 3 describes 3D whole-brain simultaneous T_1, T_2, T_2*, and susceptibility mapping technique using MR Multitasking. In the chapter, we show the sequence implementation for this technique and perform preliminary evaluations by comparing with conventional single-parametric mapping techniques for corresponding biomarkers. The agreement is assessed on phantom and healthy subjects using intra-class correlation coefficients and coefficient of variation. We also demonstrate the feasibility of contrast-weighted image synthesis using multi-parametric maps from the technique.

CHAPTER 4 presents a technique for free-breathing, non-ECG, simultaneous myocardial T_1, T_2, T_2*, and FF mapping. We propose a new sequence which improves temporal resolution and imaging efficiency. The technique is evaluated on static and motion phantoms and healthy volunteers with conventional breath-held, ECG-triggered references. The image quality is assessed by an imaging cardiologist. The technique is further incorporated into the clinical protocol for patients with post-acute sequela of COVID and patients with ischemic heart diseases (IHD) to evaluate the clinical utility.

CHAPTER 5 develops a novel reconstruction approach for low-rank tensor constraints. MR Multitasking for better image quality and shorter scan time. The technique utilizes the entire k-t

dataset acquire for estimating temporal and spatial components. Its precision and repeatability are evaluated against the previous reconstruction approach on numerical simulations and healthy subjects for different scan lengths.

Finally, CHAPTER 6 provides discussions with conclusions of the dissertation and future directions.

The work in CHAPTER 3 and CHAPTER 4 have been published as journal articles, and the manuscript for the work in CHAPTER 5 was under preparation by the time the dissertation was written.

CHAPTER 2 Background

2.1 Physics of Tissue Parameters and Quantification

This section will review some commonly used MRI-based biomarkers for tissue characterization, describe the underlying mechanisms and commonly used approaches for quantification.

2.1.1 T_1 relaxation time

When the longitudinal magnetization M_z is perturbed, it will recover to the initial equilibrium state via the exchange of energy to the surrounding "lattice", a process known as spin-lattice interaction. The T_1 relaxation time is an exponential time constant describing magnetization recovery to thermal equilibrium. Specifically, T_1 is the amount of time required for the magnetization to recover to $1 - e^{-1}$ or ~63% of its initial thermal equilibrium value when starting from zero longitudinal magnetization. The T_1 value depends on the distribution of energy across the Larmor frequency Ω of the protons interacting to produce the longitudinal recovery. Therefore, different field strengths (27, 28) and local disruptions of the Larmor frequency will change T_1.

One approach for T_1 mapping is to acquire multiple T_1-weighted images during the recovery process to fit for the underlying time constant T_1 in each voxel, as shown in Figure 2.1. Without loss of generalizability, T_1 relaxation can be modelled as:

$$M_z(t) = M_z^0 - (M_z^0 - AM_z^0)e^{-t/T_1}, \tag{2.1}$$

where $M_z(t)$ is the signal intensity of a voxel given the time t after the perturbation, and M_z^0 is the magnitude of the equilibrium state. The constant A describes the ratio between the longitudinal magnetization after the perturbation and the equilibrium magnetization. In the case that an ideal inversion pulse is used to perturb the magnetization, $A = -1$. Similarly, $A = 0$ when an ideal

saturation pulse is used. As real-world preparation pulses are subject to field imperfections and are never ideal, Equation (2.1) is generally used with a three-parameter fit for M_z^0, T_1, and A so that the pulse efficiency can be considered. Inversion recovery turbo spin echo (IR-TSE), modified Look–Locker Imaging (MOLLI) (29), and saturation recovery single-shot acquisition (SASHA) (30) are example T_1 mapping techniques built upon the same theory.

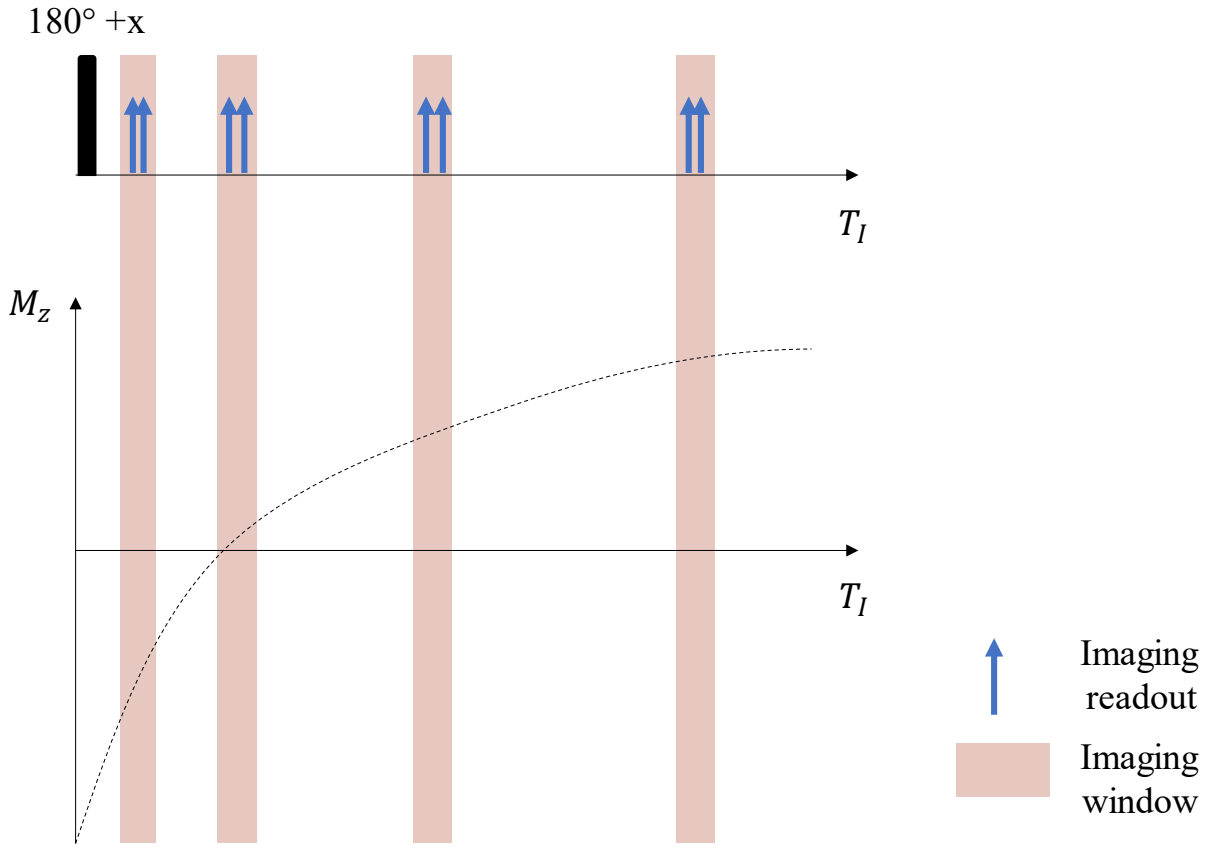

Figure 2.1: An illustration of sequence diagram used for T_1 mapping. An inversion pulse is applied, followed by imaging readouts such as FLASH or bSSFP to acquire multiple T_1-weighted images.

T_1 mapping can also be performed by acquiring multiple steady state FLASH images at different flip angles (α). The signal equation is derived as (31):

$$S(\alpha, T_1) = \mathrm{M}_0 \sin(\alpha) \frac{1 - e^{-T_R/T_1}}{1 - \cos(\alpha) e^{-T_R/T_1}}, \tag{2.2}$$

where TR is the repetition time and M_0 is equilibrium magnetization proportional to spin density. By varying α and keeping TR as constant, a curve can be generated for T_1 mapping, i.e.:

$$\frac{S}{\sin(\alpha)} = \frac{S}{\tan(\alpha)} e^{-T_R/T_1} + M_0(1 - e^{-T_R/T_1}) , \quad (2.3)$$

which is a line with slope e^{-T_R/T_1} and intercept $M_0(1 - e^{-T_R/T_1})$ and allows efficient fitting.

2.1.2 T_2 relaxation time

The longitudinal magnetization, once tipped onto the transverse plane, will start to dephase and decay. The T_2 relaxation time is the exponential time constant describing the "irreversible" decay of transverse magnetization M_{xy}. Specifically, T_2 is the time needed for the transverse magnetization to reach e^{-1} or ~37% of its initial value.

Similar to T_1 mapping, T_2 quantification requires multiple T_2-weighted images to fit the exponential curve. One common approach for this purpose is to use the turbo(fast) spin echo sequence, as illustrated in Figure 2.2. The T_2 values can be fitted for each voxel through the following two-parameter model:

$$M_{xy}(t) = M_{xy}^0 e^{-t/T_2}, \quad (2.4)$$

where M_{xy}^0 is the initial magnetization after excitation and t is the echo time. Alternatively, T_2 mapping can be performed with T_2-prepared FLASH (usually for 3T cardiac imaging) or bSSFP (usually for 1.5T cardiac imaging). In those approaches, T_2 preparation modules with varied preparation durations are used to create multiple T_2 weightings and the fitting can still be done with Equation (2.4), by defining t as T_2 preparation duration.

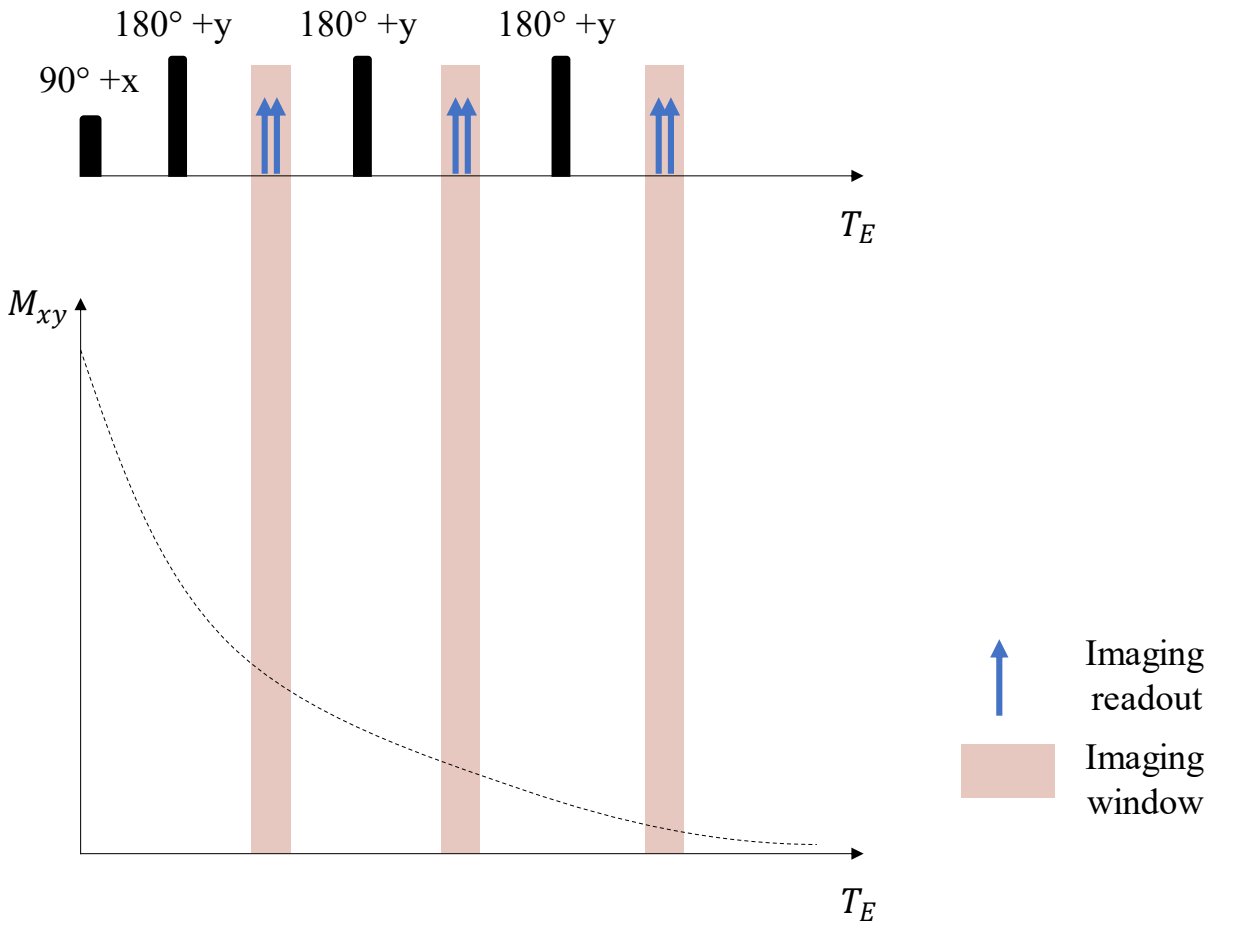

Figure 2.2: An illustration of turbo spin echo for T_2 mapping. The longitudinal magnetization is tipped into the transverse plane with a 90° excitation pulse and the magnetization starts to decay and dephase. 180° refocusing pulses are then used to rephase the spins and T_2-weighted signal are created.

2.1.3 T_2* relaxation time

T_2* relaxation time is another time constant describing the decay of transverse magnetization. Compared to T_2, T_2* describes to the "reversible" dephasing caused by loss of spin coherence. This process will be reversed when using the 180° refocusing pulses as in Figure 2.2, which removes the impact of field inhomogeneity on the spin phase. The relationship between T_2 and T_2* is described as:

$$\frac{1}{T_2^*} = \frac{1}{T_2} + \gamma \Delta B_0, \tag{2.5}$$

where γ is the gyromagnetic ratio and ΔB_0 is the field inhomogeneity across a single voxel. From Equation (2.5), it can also be inferred that T_2^* is always shorter than T_2. T_2^* mapping is typically performed using multi-echo gradient echo, which acquires multiples T_2^*-weighted images after the excitation pulse. The T_2^* values are then fitted with a two-parameter model:

$$\left|M_{xy}(t)\right| = \left|M_{xy}^0\right| e^{-t/T_2^*}, \tag{2.6}$$

where t is the echo time. An illustration of sequence and signal behavior is shown in Figure 2.3.

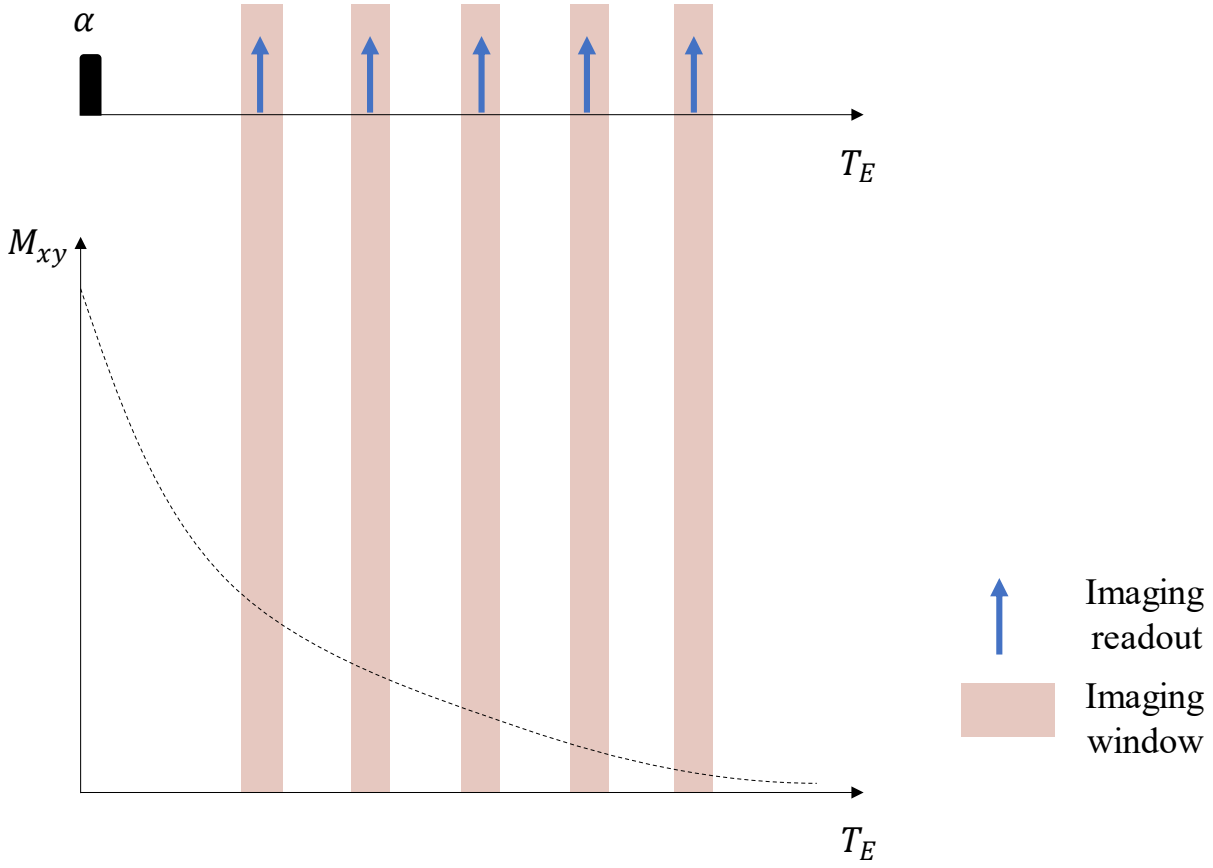

Figure 2.3: T_2^* mapping with multi-echo gradient echo.

2.1.4 Magnetic susceptibility

When a material interacts with an external magnetic field, an internal magnetization or polarization will be created which may be in parallel with or opposed to the external field. The magnetic susceptibility χ is a measure of the internal polarization (and its direction) under a unit magnetic field. Diamagnetic substances such as water, fat, and calcium have $\chi < 0$, whereas paramagnetic substances such as iron and gadolinium have $\chi > 0$.

Quantitative susceptibility mapping is typically performed with multi-echo gradient echo sequences (32, 33), with a similar diagram as shown in Figure 2.3. The main difference is that T_2* values are primarily determined by magnitude images, whereas susceptibility is primarily extracted from the phase images. In a left-handed system, the image phase $\phi(\boldsymbol{r}, T_E)$ at voxel location $\boldsymbol{r}$ and at echo time T_E can be written as:

$$\phi(\boldsymbol{r}, T_E) = \gamma \Delta B_z(\boldsymbol{r}) T_E, \tag{2.7}$$

where $\Delta B_z(\boldsymbol{r})$ is the field variations along z direction. Assuming magnetic susceptibility $\chi \ll 1$ and a dipole field, $\Delta B_z(\boldsymbol{r})$ can be derived as (32):

$$\Delta B_z(\boldsymbol{r}) = B_0[\chi(\boldsymbol{r}) * G(\boldsymbol{r})], \tag{2.8}$$

where $*$ denotes the convolution operation, and $G(\boldsymbol{r})$ is the Green's function given as:

$$G(\boldsymbol{r}) = \frac{1}{4\pi} \frac{3\cos^2\theta - 1}{r^3}. \tag{2.9}$$

Here θ is the angle between $\boldsymbol{r}$ and $\boldsymbol{z}$. The convolution in Equation (2.8) can be avoided using the convolution theorem, i.e.,

$$\Delta B_z(\boldsymbol{r}) = B_0 \mathcal{F}^{-1}[\chi(\boldsymbol{k}) \cdot G(\boldsymbol{k})], \tag{2.10}$$

where $\mathcal{F}^{-1}$ is the inverse Fourier transform, and $\chi(\boldsymbol{k})$ and $G(\boldsymbol{k})$ are Fourier transforms of $\chi(\boldsymbol{r})$ and $G(\boldsymbol{r})$, respectively.

Susceptibility can be obtained simultaneously with T_2* from a multi-echo GRE sequence. In principle, taking the phase images of a multi-echo GRE acquisition and combining Equations (2.7) - (2.9) would obtain $\chi(\boldsymbol{r})$. However, this process is not trivial in practice because: a) there are intrinsic ambiguities in phase calculations and any phase would be wrapped into the range of $[-\pi, \pi)$, leading to artificial jumps of $N \cdot 2\pi$ (N is any integer) from voxel to voxel. b) $\Delta B_z(\boldsymbol{r})$ has contributions from both local field (related to susceptibility) and background field (inhomogeneity due to imperfect shimming), and the impact from the latter needs to be removed. c) There are multiple singularities in $G(\boldsymbol{k})$ that makes Equation (2.10), and its equivalence Equation (2.8), ill-posed. Various algorithms have been proposed to address the challenges and a detailed discussion of these approaches would be beyond the scope of this section. Interested readers are hereby referred to these reviews (32, 33).

2.1.5 Fat-fraction

The protons in fat(triglycerides) are better shielded and resonant slower than those in the water molecules. The difference in resonance frequencies Δf is approximately -3.5 ppm (-220 Hz at 1.5T and -450Hz at 3T)(34). The most direct way to measure the fat content is MR spectroscopy (MRS), which plots the proton signal as a function of resonance frequency in a voxel. The peaks corresponding to water and fat signal are distinct due to different resonant frequencies and can be identified using prior knowledge. The area under the two peak denotes the corresponding signal S_w and S_F, and fat-fraction can be calculated as:

$$\eta = \frac{S_F}{S_F + S_w}. \tag{2.11}$$

MRS technique provides reliable fat-fraction estimates, but it has limited spatial coverage and scanning efficiency (a single voxel at each time). Other alternatives for FF include chemical-shift

based MRI, which typically acquire multiple images at different echo times and are known as Dixon techniques. The following equation describes signal behavior in a voxel with both water and fat compartments:

$$\mathrm{S}(\mathrm{T_E}) = \left(S_w + S_F e^{i2\pi\Delta f\, T_E}\right) e^{(i2\pi\gamma\Delta B_0 - 1/T_2^*)T_E}, \tag{2.12}$$

where S_w and S_F are the corresponding water and fat signal. Equation (2.12) assumes a common T_2* between water and fat. This is generally valid as iron often coexists with fat in pathology (35, 36) and will dominate the T_2* values in that voxel. Equation (2.12) can be refined by better modelling the fat spectrum, which contains multiple peaks with distinct resonant frequencies and relative amplitudes (37). Taking fat spectrum as a priori, S_w, S_F, ΔB_0, and T_2* in Equation (2.12) could be estimated using a multi-echo acquisition and some nonlinear estimation methods such as IDEAL (38), VARPRO (39), adaptive multi-step fitting (40), and graph cut (41). A simplified pipeline for this process is shown in Figure 2.4. In practice, it was shown that six echoes achieved a good balance between efficiency and reliability (42).

It should be noted that S_w and S_F solved from Equation (2.12) are mixture of both proton signal and T_1-weightings from water and fat. As fat has shorter T_1 compared to that of water, it results in a relative amplification of fat-fraction known as T_1 bias. One common strategy to reduce T_1 bias is to use a low flip angle (43).

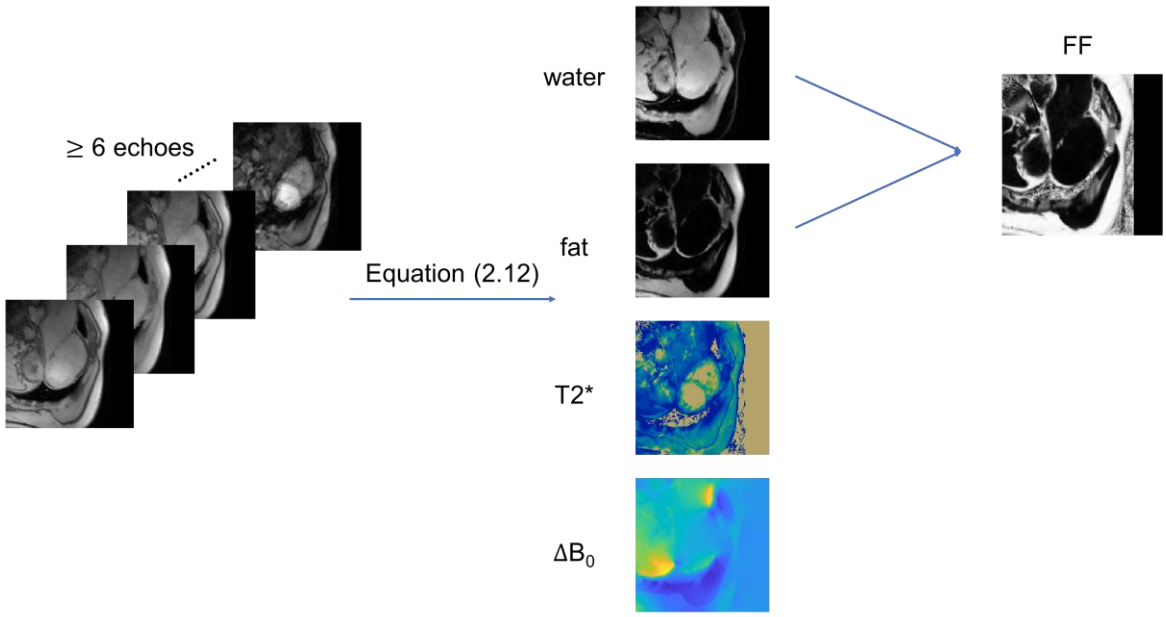

Figure 2.4: Processing workflow for FF with multi-echo gradient echo.

2.2 Multiparametric Mapping

Early attempts at whole-brain T_1 and T_2 mapping included techniques included techniques such as DESPOT1 and DESPOT2 (44). The technique utilized steady state FLASH sequences acquired at multiple flip angles for T_1 mapping. For T_2 mapping, balanced steady state free precession (bSSFP) sequences with T_2/T_1 contrasts were acquired at multiple flip angles. And T_2 values were obtained based on previously determined T_1 values. In practice, it was found that two flip angles for FLASH and bSSFP were sufficient, enabling clinical feasible scan times. Additionally, Haacke et al. (15-17) combined the dual flip angle FLASH approach with multi-echo acquisitions, achieving whole-brain T_1, T_2*, and susceptibility mapping within 5 minutes. However, both techniques rely on multiple acquisitions and misregistration issues between successive scans could potentially confound the quantification results.

Recent technical advances have enabled simultaneous multiparametric mapping in a single scan. Ma et al. proposed the MR fingerprinting (MRF) technique in 2014 (45), which achieved

single-slice joint T_1/T_2 mapping in a 12-second scan. MRF assumes that tissues with distinct parameters have unique signal evolutions using appropriate preparation pulses and acquisition parameters (TR, TE, flip angle, etc.). A dictionary can be pre-constructed with signal evolutions from all feasible tissue parameter combinations, and the acquired signal from each voxel is matched to the dictionary to estimate the underlying tissue parameters (46). MRF is not limited to T_1/T_2 mapping and is now one of the most used parametric mapping frameworks, covering $T_1\rho$ (47), T_2* (48), perfusion (49), CEST (50), magnetization transfer (51), and fat-fraction (52) quantification. However, MRF is sensitive to motion, especially when it occurs in the middle of the scan (53). To address this issue, motion freezing strategies such as breath-holding and/or ECG-triggering for liver and cardiac MRF (47, 52). Alternatively, external motion monitors (54-56) such as respiratory bellows and ECG signal can be used for retrospective motion identification, but it may only provide a relative motion measurement and may be prone to errors (57).

In addition, multi-echo two inversion-contrast magnetization-prepared rapid gradient echo sequence (ME-MP2RAGE) used two different inversion times (18-20), each with a unique flip angle and with ME-FLASH readouts for T_1, T_2*, and susceptibility quantification. Akçakaya et al. combined saturation and T_2 preparation pulses, varying the saturation time and T_2 preparation time to generate co-registered T_1 and T_2 maps for a single slice in a 13-heartbeat breath-hold (58). Kellman et al. achieved joint post-contrast T_1 and T_2 mapping in a single 45-heartbeat free-breathing multiparametric SASHA scan (59). However, these techniques are still sensitive to random and/or physiological motion.

2.3 MR Multitasking for Motion-resolved, Multiparametric Mapping

In 2018, the MR Multitasking framework for motion-resolved, simultaneous multiparametric mapping was developed by Christodoulou et al (60). It addresses the challenge of resolving

overlapping temporal dynamic processes, including physiological processes (e.g., cardiac, and respiratory motion) and physical processes (e.g., relaxation), by modelling them as different time dimensions and leveraging spatiotemporal correlations. The framework utilizes a low-rank tensor method to efficiently recover and store the underlying images and distinguishes itself from MRF with motion-resolving capability.

2.3.1 Low-rank tensor imaging framework

Consider a multi-dimensional image function $I(\boldsymbol{r}, t_1, t_2, \dots, t_d)$ with 1 spatial dimension denoted by $\boldsymbol{r}$ and d temporal dimensions denoted by $t_1, t_2, \dots, t_d$, such as cardiac motion dimension and T_1 relaxation dimension. The multi-dimensional image can be discretized as a $d+1$ way tensor $\mathcal{X}$ with size $[N_0, N_1, N_2, \dots, N_d]$. It is challenging to recover such a tensor due to the well-known "curse of dimensionality", which makes scan time grow exponentially with the number of dimensions d. However, the degrees of freedom in $\mathcal{X}$ can be significantly reduced by leveraging the spatiotemporal correlations (61), which allows accelerated acquisitions whose scan time grows linearly rather than exponentially with increased number of dimensions.

The Tucker form (62) of the low-rank tensor decomposition is employed, which factorizes $\mathcal{X}$ into the product of a core tensor $\mathcal{G}$ and $d+1$ factor matrices corresponding to 1 spatial dimension and d temporal dimensions:

$$\mathcal{X} = \mathcal{G} \times_1 \boldsymbol{U}_{\boldsymbol{r}} \times_2 \boldsymbol{U}_{t_1} \times_3 \boldsymbol{U}_{t_2} \times_4 \cdots \times_{d+1} \boldsymbol{U}_{t_d}. \tag{2.13}$$

Here $\times_i$ denotes the ith mode tensor matrix product (63), the factor matrix $\boldsymbol{U}_{\boldsymbol{r}}$ has size $[N_0, L_0]$ and contains L_0 basis functions for N_0 voxels each, the factor matrix $\boldsymbol{U}_{t_i}$ has size $[N_i, L_i]$ and contains L_i basis functions for N_i time points (time bins) each, and the core tensor has size $[L_0, L_1, L_2, \dots, L_d]$ and governs the interaction between all the factor matrices. For all dimensions, $L_i \leq N_i$. An example for low-rank tensor decomposition is shown in Figure 2.5. Note that the

factorization in Equation (2.13) reduces degrees of freedom from $N_0N_1N_2\cdots N_d$ to $L_0L_1L_2\cdots L_d + L_0N_0 + L_1N_1 + \cdots L_dN_d$. And the recovery of the tensor $\mathcal{X}$ is now equivalent to the recovery of the core tensor and factor matrices. Certain temporal dimensions, such as the one corresponding to inversion recovery, can be predetermined by building a dictionary and performing SVD on it, which will further reduce the degrees of freedom.

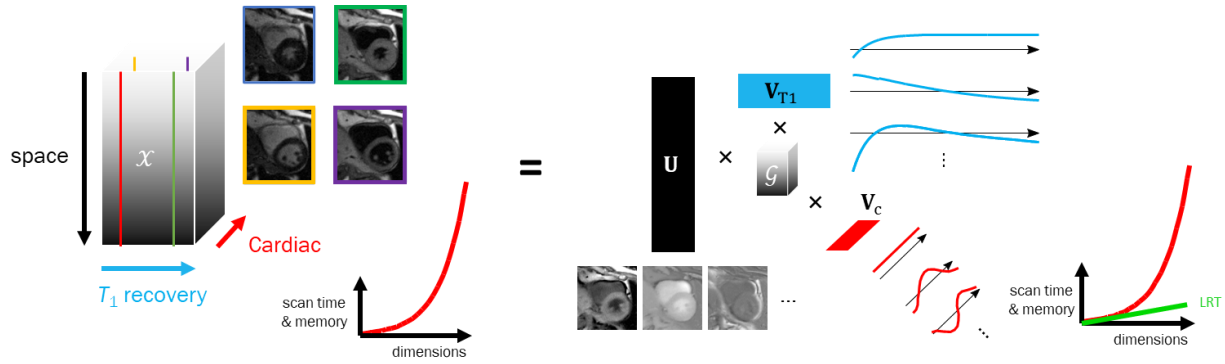

Figure 2.5: Illustration of a 3-way tensor with 1 spatial dimension, 1 temporal dimension corresponding to T_1 recovery, and 1 temporal dimension corresponding to cardiac motion. It can be factorized into the product of a core tensor and 3 factor matrices, which significantly reduces required scan time and memory. Images courtesy to Dr. Sen Ma.

2.3.2 Sequence design and image reconstruction

MR Multitasking performs data collection in a continuous acquisition with intermittent magnetization preparation pulses such as IR, T_2 prep, or diffusion prep. Two datasets are collected in an interleaved way: the training data is acquired at kspace center and is used for resolving temporal information; the imaging data is collected using an incoherent sampling pattern (e.g., radial golden angle) and is used for resolving spatial information. A generic sequence diagram for MR Multitasking is shown in Figure 2.6. The scan runs without synchronizing to respiratory or ECG signal and does not require this information retrospectively for image reconstruction.

In general, MR image reconstruction workflow has the following steps: (1) real-time reconstruction and motion binning; (2) training dataset completion; (3) temporal basis function and core tensor estimation from training data; (4) spatial factor estimation from imaging data.

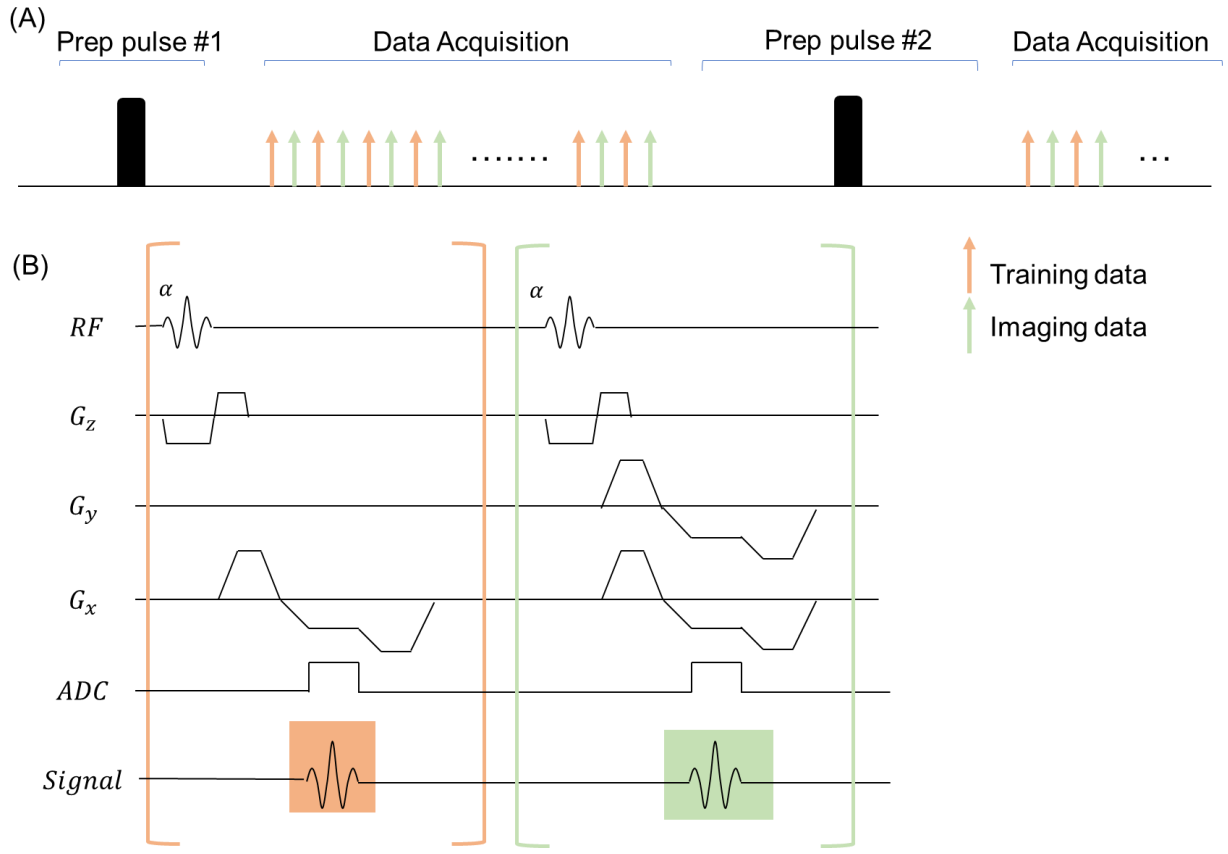

Figure 2.6: (A) An example MR Multitasking sequence, which cycles through different preparation modules and performs data collection during the gap between preparations. The training and imaging data is collected in an interleaved way. (B) The training data is acquired at k-space center line (k_y=0) for resolving temporal information, while imaging data is acquired with an incoherent sampling pattern (such as golden angle radial trajectory) for resolving spatial information.

The first step for image reconstruction is ungated (real-time) reconstruction for motion identification. Here the images are modelled as a low-rank matrix with 1 spatial dimension and 1 generalized time dimension corresponding to the elapsed time since the start of the scan. Real-time temporal basis $\boldsymbol{\Phi}_{\mathbf{rt}}$ are obtained from SVD of the training data, and the spatial factors $\boldsymbol{U}$ are estimated through a least-squares fitting to the imaging data, i.e.:

$$\widehat{\mathbf{U}} = \arg\min_{\boldsymbol{U}} \left\| \mathbf{d}_{\text{img}} - \Omega(\mathbf{FSU}\boldsymbol{\Phi}_{\mathbf{rt}}) \right\|_2^2. \tag{2.14}$$

Here **F** denotes Fourier transform, **S** is the sensitivity map, and $\Omega(\cdot)$ is the sampling operator for imaging data. Following this step, real-time images are generated which shows motion and changing tissue contrast throughout the scan. An example real-time image for cardiac T_1 mapping is shown in Figure 2.7, which experiences cardiac and respiratory motion and contrast changes throughout the scan. A modified k-means clustering algorithm as previously described (60) is then used to automatically place the corresponding images into different motion states (such as different cardiac bins and respiratory bins).

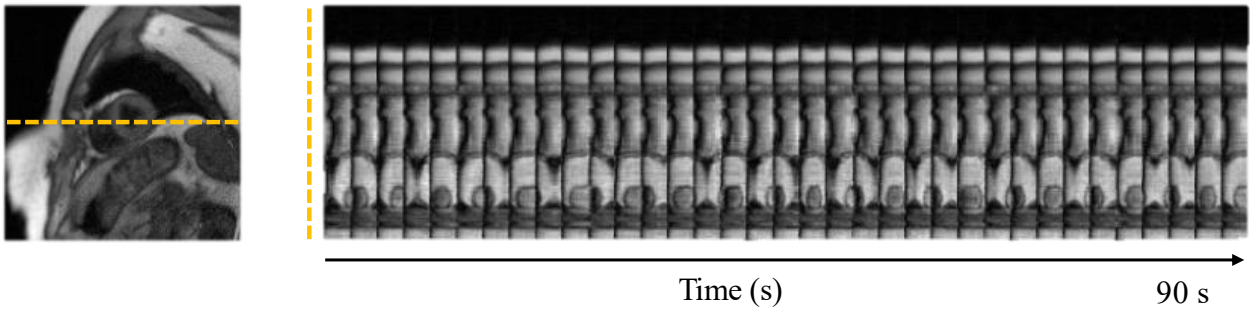

Figure 2.7: Example real-time images showing the time profile of a horizontal line (yellow line) throughout the 90-second scan.

The training tensor $\mathcal{D}_{tr}$, as expressed in $(\boldsymbol{k}, t_1, t_2, \ldots, t_d)$ -space, is undersampled along temporal dimensions. A small-scale, low-rank tensor completion algorithm is used by solving the following optimization problem:

$$\widehat{\mathcal{D}}_{\text{tr}} = \arg\min_{\mathcal{D}_{\text{tr}}} \|\mathbf{d}_{\text{tr}} - \Omega_{\text{tr}}(\mathcal{D}_{\text{tr}})\|_2^2 + \lambda \sum_{i=1}^{d} \left\| \mathbf{D}_{\text{tr},(i)} \right\|_* + R_{\text{t}}(\mathcal{D}_{\text{tr}}). \tag{2.15}$$

where $\mathbf{d}_{\text{tr}}$ is the collected training data, $\Omega_{\text{tr}}(\cdot)$ is the sampling operator for the training dataset, $\mathbf{D}_{\text{tr},(i)}$ is the mode-i unfolding of the complete training tensor, $\|\cdot\|_*$ denotes the matrix nuclear norm, and $R_{\text{t}}(\cdot)$ is an optional temporal regularizer, such as temporal total variation (TV). Once

the training data is completed, the individual temporal basis $\boldsymbol{U}_{t_1}, \boldsymbol{U}_{t_2}, \ldots, \boldsymbol{U}_{t_d}$ and core tensor $\mathcal{G}$ can be extracted from high-order SVD of the training dataset.

Finally, the spatial coefficients $\boldsymbol{U}_{\boldsymbol{r}}$ are determined by:

$$\widehat{\mathbf{U}} = \arg\min_{\mathbf{U}} \left\| \mathbf{d}_{\text{img}} - \Omega\left(\widehat{\Phi} \times_1 \mathbf{FSU}\right) \right\|_2^2 + \lambda R_{\text{s}}(\mathbf{U}), \tag{2.16}$$

for known temporal factor tensor $\widehat{\Phi} = \mathcal{G} \times_2 \boldsymbol{U}_{t_1} \times_3 \boldsymbol{U}_{t_2} \times_4 \cdots \times_{d+1} \boldsymbol{U}_{t_d}$, where $\mathbf{d}_{\text{img}}$ is the imaging data, and $R_{\text{s}}(\cdot)$ is an optional regularization such as wavelet sparsity. The reconstructed image tensor is given by the product $\mathcal{X} = \widehat{\Phi} \times_1 \widehat{\mathbf{U}}$.

CHAPTER 3 Three-dimensional simultaneous brain mapping of T_1, T_2, T_2*, and magnetic susceptibility

3.1 Introduction

MRI offers flexible contrast between different brain tissues based on their distinct physical properties including proton density, longitudinal relaxation time (T_1), transverse relaxation times (T_2, T_2*), and magnetic susceptibility (χ). Compared to qualitative or contrast-weighted images, quantitative imaging provides objective information for tissue characterization and clinical diagnosis. Direct measurement of the above parameters facilitates pathology detection such as tumor (64), ischemia (65), multiple sclerosis (66, 67), and Parkinson's disease (68, 69). Compared to single parameter mapping, multiparametric approaches offer the potential for more comprehensive tissue characterization and more accurate diagnosis. It has been shown that the combination of R2* and susceptibility is useful to characterize heterogeneity in MS lesions (70). Additionally, combined use of R2* and fractional anisotropy has enhanced the sensitivity and specificity in differentiating Parkinson's disease (PD) patients from healthy controls (11).

In practice, multiparametric mapping typically requires separate scans. Different methods, including inversion recovery spin echo (IRSE), variable flip angle (VFA) (71), multi-echo spin-echo (72), and multi-echo GRE (33, 73-75), have been proposed to measure T_1, T_2, T_2*, and susceptibility independently. Separate acquisitions may result in prolonged scan time, complicated imaging workflows, and misaligned parameter maps due to inter-scan misregistration. Recent technical developments have enabled simultaneous, multiparametric mapping. STrategically Acquired Gradient Echo (STAGE) (15-17) achieves T_1, T_2*, and quantitative susceptibility mapping (QSM) using two multi-echo GRE sequences with different flip angles, but lacks T_2

quantification and requires B1 inhomogeneity correction. Multi-Echo (ME) Magnetization-Prepared 2 RApid Gradient Echoes (MP2RAGE) (18-20) uses two different inversion times each with a unique flip angle and with multi-echo GRE readouts for T_1, T_2*, and susceptibility quantification. However, the evolution of the magnetization during the long acquisition window results in distortion of the point-spread function and causes blurring (76, 77). In addition, it does not perform flow compensation and would therefore be subject to phase errors from flow effects (33). Recent MR fingerprinting work combines the existing balanced SSFP methods with varied RF excitation phases for simultaneous quantification of T_1, T_2, and T_2*, yet is limited by 2D acquisition, banding artifacts, and long acquisition time (35s per slice) (78).

In this work, we develop a new technique for 3D whole-brain simultaneous T_1, T_2, T_2*, and susceptibility quantification in a single 9.1 min scan, based on the MR Multitasking framework. Hybrid T_2-IR preparations generate different T_1 and T_2 weightings, while multi-echo GRE readouts with full flow compensation for all echoes generate different T_2* weightings. The underlying image is modeled as a six-dimensional low rank tensor (LRT) with three spatial dimensions and three temporal dimensions modelling T_1, T_2, and T_2* relaxations. In addition, we also show six contrast-weighted images that can be generated from the T_1/T_2/T_2*/susceptibility maps. The agreement between the proposed method and conventionally accepted quantitative reference mapping techniques for each tissue property is evaluated in phantom and volunteer studies.

3.2 Methods

3.2.1 Pulse sequence framework

3.2.1.1 Pulse sequence

Figure 3.1 shows the proposed sequence diagram. T_1 and T_2 weightings are generated by cycling through T_2-IR preparations with four different preparation durations (τ, with $\tau = 0$ corresponding to a standard IR pulse). Multi-echo GRE readouts with different echo times (T_E) produce different T_2* weightings and images with different susceptibility contributions. FLASH excitations fill the entire recovery period to acquire readouts at multiple inversion times (T_I).

Flow induced phase variation can be a potential source of error when quantifying susceptibility (33). Available multi-echo sequences typically only perform flow compensation on the first echo (79). Failure to compensate the flow may lead to arbitrary phase inside the vessels and non-local artifacts in susceptibility maps (80, 81). In this work, we adopt a previously proposed flow compensation scheme (81) for 3D monopolar multi-echo acquisition, where extra bipolar pairs are implemented along both phase encoding and partition encoding directions (Figure 1B). In the readout direction, insertion of an appropriate gradient before the first echo can naturally achieve the flow compensation at the center of each echo.

Two interleaved subsets of data are collected during a continuous acquisition (Figure 1C): training data $\mathbf{d}_{\text{tr}}$ which frequently repeat one $\mathbf{k}$-space trajectory with a high temporal sampling rate, and imaging data $\mathbf{d}_{\text{img}}$ which sparsely sample $(\mathbf{k}, t)$-space with greater $\mathbf{k}$-space extent for high spatial resolution. The imaging data densely sample $(\mathbf{k}, t)$-space for the chosen $\mathbf{k}$-space trajectory, and will therefore allow the calculation of a highly temporally-resolved subspace of plausible contrast-weighting evolutions during image reconstruction; in this work, $\mathbf{d}_{\text{tr}}$ was collected at the central $\mathbf{k}$-space line $k_y = k_z = 0$) every 4 readouts (~ 80ms). The imaging data

then allow high-resolution calculation of voxelwise contrast-weighting evolution within the temporal subspace; here, $\mathbf{d}_{\text{img}}$ was collected using a 3D randomly-ordered trajectory with Gaussian density distribution along both partition and phase encoding directions in order to provide incoherent $(\mathbf{k}, t)$-space sampling.

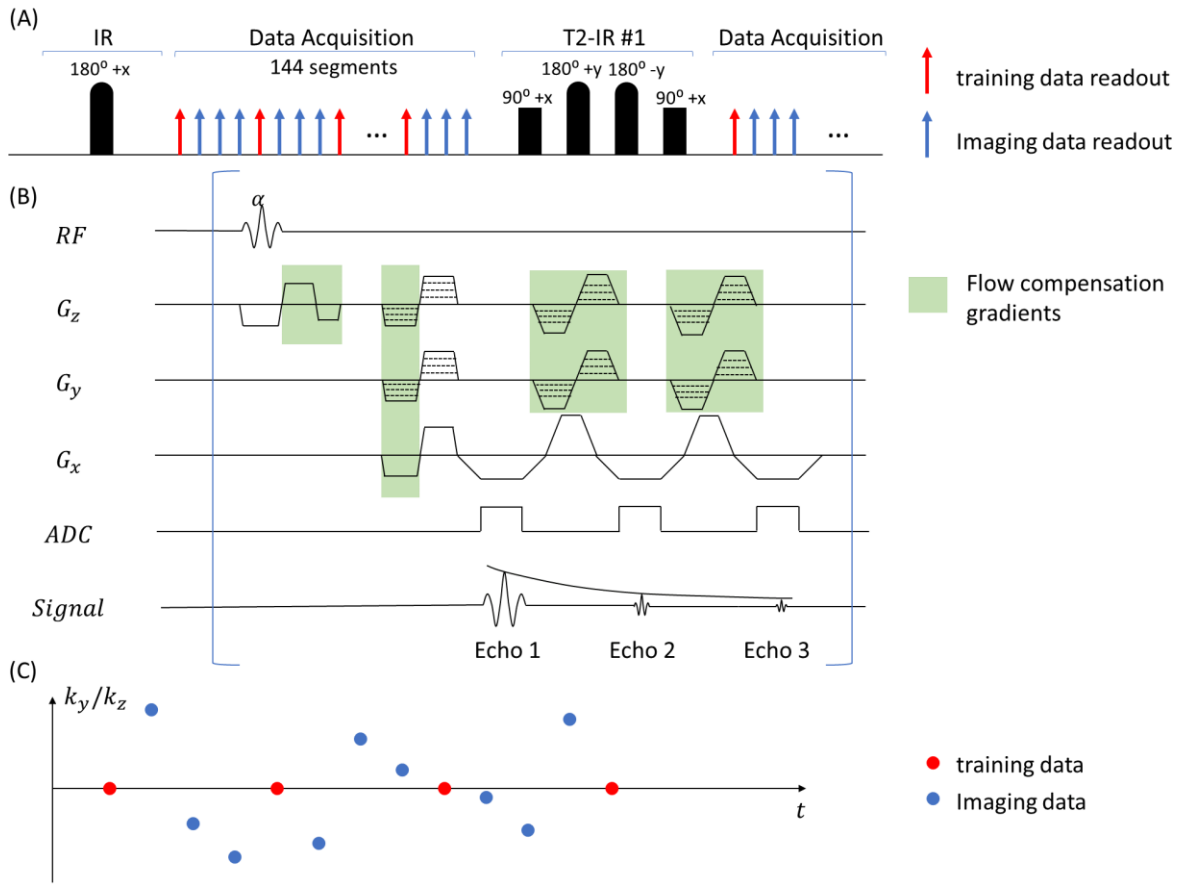

Figure 3.1: (A) Sequence diagram for the proposed multitasking $T_1/T_2/T_2^*$ mapping framework. Hybrid T_2prep/IR (T_2-IR) preparation modules were followed by 144 multi-echo GRE readouts, which enable collection of k-space lines with different $T_1/T_2/T_2^*$ contrasts. The training data was acquired every 4 readouts. (B) Illustration of readout module. After each α pulse, a total of 3 echoes, each of them fully flow compensated along all directions, were collected in a monopolar way. In the readout direction, each echo is refocused, and flow compensation is naturally achieved at the center of each echo after inserting an appropriate moment nulling gradient before the first echo. In the phase/partition encoding direction, however, bipolar gradient pairs were added for all later echoes. (C) Simplified illustration of k-space sampling pattern. Cartesian acquisition with random Gaussian distribution was adopted along k_y and k_z axis. k-Space center was acquired every 4 readouts and would serve for tracking temporal dynamics.

3.2.1.2 Image model

The Multitasking framework models the underlying image as a 6D image $x(\mathbf{r},\tau,T_I,T_E)$ with 3 spatial dimensions indexed by $\mathbf{r}=[x,y,z]$, and 3 temporal dimensions τ, T_{I}, and T_{E}. Here τ is the T_2-IR prep duration, T_I is the inversion time, and T_E is the echo time. Acquisition of image x at the Nyquist rate would suffer from the curse of dimensionality and result in an impractical scan time. However, x can still be recovered from highly undersampled data by exploiting the spatial-temporal correlation throughout the image. Specifically, this correlation allows x to be decomposed into the following partially separable form (82):

$$x(\mathbf{r},\tau,T_I,T_E)=\sum_{l=1}^{L}u_l(\mathbf{r})\phi_l(\tau,\mathrm{T_I},T_E), \tag{3.1}$$

where $\{u_l(\mathbf{r})\}_{l=1}^{L}$ are the spatial basis functions and $\{(\phi_l(\tau,T_I,T_E)\}_{l=1}^{L}$ are temporal functions spanning a multi-dimensional temporal subspace. The temporal functions ϕ themselves can also be decomposed in terms of individual bases along each temporal dimension, e.g.:

$$\phi_l(\tau,\mathrm{T_I},T_E)=\sum_{m=1}^{M}\sum_{n=1}^{N}\sum_{p=1}^{P}g_{lmnp}\,v_m(\tau)w_n(\mathrm{T_I})q_p(\mathrm{T_E}), \tag{3.2}$$

where $\{v_m(\tau)\}_{m=1}^{M},\{w_n(T_{\mathrm{I}})\}_{n=1}^{N},\{q_p(T_{\mathrm{E}})\}_{p=1}^{P}$ are temporal basis functions for T_2, T_1, and T_2* relaxation dimensions and where g_{lmnp} are elements of a core tensor $\mathcal{G}$ (83). The combination of Equations (3.1) and (3.2) implies that a discretized image tensor $\mathcal{X}$ with elements $x_{ijks}=x(\mathbf{r}_i,\tau_j,T_{\mathrm{I},k},T_{\mathrm{E},s})$ can be decomposed in Tucker form (62, 63) as follows:

$$\mathcal{X}=\mathcal{G}\times_1\mathbf{U}\times_2\mathbf{V}\times_3\mathbf{W}\times_4\mathbf{Q}, \tag{3.3}$$

where the $\times_i$ operator denotes the ith mode product (63), the columns of $\mathbf{U}$ contain the spatial basis functions such that $\mathbf{U}_{i,l}=u_l(\mathbf{r}_i)$, and the columns of $\mathbf{V}$, $\mathbf{W}$, and $\mathbf{Q}$ contain the temporal basis

functions for each corresponding dimension such that $\mathbf{V}_{j,m} = v_m(\tau_j)$, $\mathbf{W}_{k,n} = w_n(T_{\mathrm{I},k})$, $\mathbf{Q}_{s,p} = q_p(T_{\mathrm{E},s})$. By separating the temporal factors **V**, **W**, and **Q** from the spatial factor **U**, the model in Equation (3.3) partially decouples conflicting temporal and spatial resolution sampling requirements: the high-speed training data in $\mathbf{d}_{\mathrm{tr}}$ can be used to determine the temporal factors, and the $\mathbf{d}_{\mathrm{img}}$ (which extensively covers k-space) can be used to determine **U** with high spatial resolution. The end result is an $\mathcal{X}$ that is both highly spatially- and temporally-resolved.

3.2.1.3 Image reconstruction

Equation (3.3) implies that the 4-way tensor $\mathcal{X}$ can be recovered from undersampled $(\mathbf{k}, \tau, T_{\mathrm{I}}, T_{\mathrm{E}})$-space data via low-rank tensor completion. For example, this could in principle be done by solving the following optimization problem:

$$\widehat{\mathcal{X}} = \arg\min_{\mathcal{X}} \left\| \mathbf{d}_{\mathrm{img}} - \Omega(\mathcal{X} \times_1 \mathbf{FS}) \right\|_2^2 + \lambda \sum_{i=1}^{4} \left\| \mathbf{X}_{(i)} \right\|_* + R(\mathcal{X}), \tag{3.4}$$

where $\mathbf{d}_{\mathrm{img}}$ is the imaging data, $\Omega(\cdot)$ is the sampling operator, **F** represents the Fourier transform, **S** applies sensitivity maps, λ is the rank regularization parameter, $\mathbf{X}_{(i)}$ denotes the *i*-mode matrix unfolding of $\mathcal{X}$ (i ranges from 1 to 4 as $\mathcal{X}$ is a 4-way tensor), $\|\cdot\|_*$ denotes the matrix nuclear norm, and $R(\cdot)$ is an optional regularizer which can be employed to enforce complementary image properties such as transform sparsity.

Although Equation (3.4) can be a potential solution, implementing it can be impractical owing to the large memory consumption in storing and operating upon the entire $\mathcal{X}$ without taking advantage of the decomposition in Equation (3.3) (60). Instead of solving Equation (3.4), we employ a computationally-efficient practical alternative to reconstruct $\mathcal{X}$ in factored form, e.g., solving directly for an individual parameter such as **U**:

$$\widehat{\mathbf{U}} = \arg\min_{\mathbf{U}} \left\| \mathbf{d}_{\text{img}} - \Omega(\mathcal{G} \times_1 \mathbf{FSU} \times_2 \mathbf{V} \times_3 \mathbf{W} \times_4 \mathbf{Q}) \right\|_2^2 + \lambda R_{\text{s}}(\mathbf{U}), \tag{3.5}$$

for known temporal components $\mathcal{G}$, **V**, **W**, and **Q**, and where $R_{\text{s}}(\cdot)$ is a spatial regularizer, chosen as a total variation (TV) penalty for this study. Note that the required "prior" knowledge of temporal components can be obtained in two steps: (1) predetermine the T_1 recovery basis functions in **W** from a dictionary of IR signal curves; and (2) estimate the T_2 relaxation basis functions in **V,** T_2* relaxation basis function in **Q**, and core tensor $\mathcal{G}$ from the training data $\mathbf{d}_{\text{tr}}$.

In the first step, we generate a dictionary of physically feasible IR-GRE signal curves for a range of feasible T_1 and B_1 inhomogeneity values based on the Bloch equations (60). The dictionary consists of 101 T_1 values logarithmically spaced from 100 ms to 3000 ms, 24 flip angles equally spaced between 0.5° to 12°, and 21 inversion efficiency factors equally spaced between -1 (perfect inversion) and -0.5. The T_1 recovery basis functions in **W** are estimated from the singular value decomposition (SVD) of this training dictionary.

In the second step, the training tensor $\mathcal{D}_{\text{tr}}$, as expressed in $(\mathbf{k}, \tau, T_{\text{I}}, T_{\text{E}})$-space, can still be incomplete. However, it has much smaller size than the imaging data and can be recovered in a similar fashion as in Equation (3.4):

$$\widehat{\mathcal{D}}_{\text{tr}} = \arg\min_{\mathcal{D}_{\text{tr}}} \|\mathbf{d}_{\text{tr}} - \Omega_{\text{tr}}(\mathcal{D}_{\text{tr}})\|_2^2 + \lambda \sum_{i=1}^{4} \left\| \mathbf{D}_{\text{tr},(i)} \right\|_*, \tag{3.6}$$

where $\mathbf{d}_{\text{tr}}$ is the training data, $\Omega_{\text{tr}}(\cdot)$ is the sampling operator for the training dataset, and $\mathbf{D}_{\text{tr},(i)}$ denotes the *i*-mode matrix unfolding of $\mathcal{D}_{\text{tr}}$ (i ranges from 1 to 4 as $\mathcal{D}_{\text{tr}}$ is a 4-way tensor). Note Equation (6) is practical to solve, as $\mathcal{D}_{\text{tr}}$ is of much smaller size than $\mathcal{X}$ and does not need to be encoded by the Fourier transform and coil sensitivities as in Equation (4). Once the completed $\widehat{\mathcal{D}}_{\text{tr}}$ has been recovered, the core tensor $\mathcal{G}$, T_2 basis functions **V**, and T_2* basis functions **Q** can be extracted by truncating the high-order SVD (HOSVD)(84) of $\widehat{\mathcal{D}}_{\text{tr}}$. This allows the spatial basis $\widehat{\mathbf{U}}$

to be solved as described in Equation (3.5). The final reconstructed tensor is then given by the product $\widehat{\mathcal{X}} = \widehat{\Phi} \times_1 \widehat{\mathbf{U}}$.

In this work we follow the approach in Equations (3.5) and (3.6). The low-rank tensor modelling of the image series and reconstruction workflow can be found in Figure 3.2.

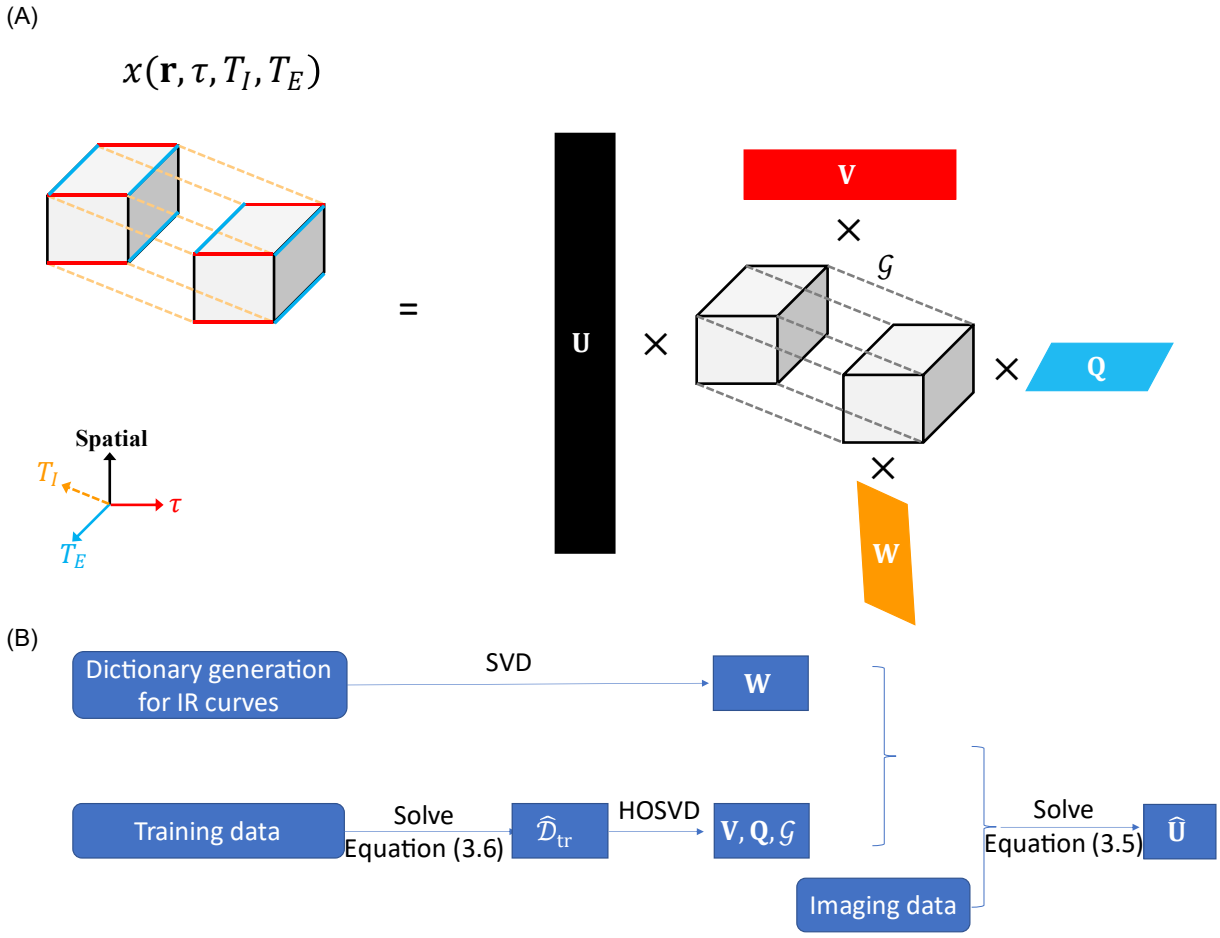

Figure 3.2: (A) Illustration of multiple temporal dimensions of the low-rank tensor for simultaneous T_1, T_2, T_2*, and susceptibility mapping. The image tensor contains spatial, T_2IR preparation duration τ, inversion time T_I, echo time T_E dimensions, with size $[N_x \cdot N_y \cdot N_z, 4, 144, 3]$. The low-rank tensor structure can be explicitly expressed through tensor factorization between 4 sets of basis functions ($\mathbf{U}$ with size $[N_x \cdot N_y \cdot N_z, L]$, V with size $[4, M]$, $\mathbf{W}$ with size $[144, N]$, $\mathbf{Q}$ with size $[3, P]$) assigned to each dimension and a core tensor ($\mathcal{G}$ with size $[L, M, N, P]$) governing the interaction between different basis functions. (B) Reconstruction workflow. The reconstructed tensor is given by $\widehat{\mathcal{X}} = \mathcal{G} \times_1 \mathbf{U} \times_2 \mathbf{V} \times_3 \mathbf{W} \times_4 \mathbf{Q}$.

3.2.1.4 Parameter quantification

Multiparametric fitting was based on the following equation at a given T_2-IR preparation time (τ), nth readout index since preparation (i.e., n=1, 2, …, N_{seg}, where N_{seg} denotes the number of segments within one recovery period, such that $T_I = nT_R$) and echo time (T_E):

$$S = A\frac{1 - e^{-T_R/T_1}}{1 - e^{-T_R/T_1}\cos\alpha}\Big[1 + \left(B\,e^{-\tau/T_2} - 1\right)\left(e^{-T_R/T_1}\cos\alpha\right)^n\Big]e^{-T_E/T_2^*}\,e^{j2\pi\Delta B_0 T_E}\sin\alpha, \tag{3.7}$$

where A absorbs proton density (equilibrium magnetization M_0) and receiver coil sensitivity, B represents the effective inversion efficiency independent of T_2 (with B = -1 being perfect), ΔB_0 describes the effect of static field inhomogeneity in Hz, T_R is the repetition time, and α denotes the flip angle. Nonlinear least squares-fitting was performed on the three-way tensor reconstructed at each voxel using Equation (3.7) for A, T_1, T_2, T_2^*, B, and ΔB_0.

Magnetic susceptibility was estimated using the multi-echo images at different echo time T_E of the last inversion time ($n = N_{\text{seg}}$), closest to the GRE steady-state contrast. Phase images at different echo times were unwrapped using the quality guided 3D phase unwrapping algorithm (85). After that, brain regions were masked with a brain extraction tool (BET) (86) and background field was removed using Sophisticated Harmonic Artifact Reduction for Phase data (SHARP) (87). Individual QSM images were generated at each echo using iterative susceptibility weighted Imaging and mapping (iSWIM) method (88, 89) with 4 iterations and threshold of 0.15. Finally, they were combined using a weighted averaging method (90):

$$\chi = \frac{\sum_{i=1}^{3} M_i^2 \chi_i}{\sum_{i=1}^{3} M_i^2}, \tag{3.8}$$

where χ_i is the susceptibility estimated at echo time $T_{E,i}$, and $M_i = T_{E,i}e^{-T_{E,i}/T2^*}$.

3.2.2 Data acquisition

3.2.2.1 MR Multitasking imaging protocol

MRI experiments were performed on a 3T scanner (Biograph mMR, Siemens Healthineers, Erlangen, Germany) with a 20-channel head coil. Acquisition cycled through hybrid T_2IR modules with preparation times τ = 0, 30, 55, 80 ms. Within each readout module, three echo times at T_E = 5.0, 10.0, 16.25 ms were collected. The scan time for Multitasking was 9.1 min. Scan parameters for Multitasking were: field of view (FOV) = 276 × 207 mm^2, in-plane resolution = 0.7 × 1.4 mm^2, slice thickness = 2 mm. More detailed imaging protocol was summarized in Table 3.1.

Table 3.1: MR Multitasking T_1/T_2/T_2*/susceptibility mapping protocol

FOV (mm^2)	276 x 207	**Slab thickness (mm)**	144
In-plane resolution (mm^3)	0.7 x 1.4	**Slice thickness (mm)**	2
Scanning matrix	384 x 144	**Number of slices**	72
Recovery period (ms)	2780	**Number of segments**	144
T_R (ms)	19.3	**Echo time (ms)**	5, 10, 16.25
T_2 prep duration (ms)	0, 30, 55, 80	**Pixel BW (Hz/pixel)**	482
Flip angle (^{0})	8	**Number of recovery periods**	192
Scan time (min:sec)	9:08		

3.2.2.2 Phantom study

A standard $T_1/T_2/T_2^*$ phantom (Calimetrix, Madison, WI USA) was scanned for validation of the quantitative estimates of the tissue properties. Inversion-recovery spin echo (IR-SE), T_2-weighted spin echo (T_2-SE) and 3D multi echo gradient echo (ME-GRE) were used as the reference for T_1, T_2 and T_2^* respectively.

Another susceptibility phantom was constructed by embedding 5 different falcon tubes, each filled with different concentrations (0, 1, 3, 5, or 7 mmol/L) of gadolinium (OptiMARK, Liebel-Flarsheim Company, Raleigh, NC) solution, into a 1% agarose gel solution in a 1000 mL plastic container. The phantom was scanned with Multitasking and reference (ME-GRE) sequences.

Imaging parameters for all reference sequences are summarized in Table 3.2.

Table 3.2: Scan parameters for phantom study.

Phantom Study Protocols	
Imaging Protocol	**Scan Parameters**
IR-SE (116.8min)	FOV=276x207mm^2, in-plane resolution=1.4x1.4mm^2, slice thickness=5mm, 1 slice, TIs=[50, 210, 350, 500, 1000, 1500, 2400, 3000]ms
T_2-SE (102.2min)	FOV=276x207mm^2, in-plane resolution=1.4x1.4mm^2, slice thickness=5mm, 1 slice, TEs=[15, 25,45, 70, 100, 150, 200]ms
ME-GRE (3.5min)	FOV=276x207mm^2, in-plane resolution=0.7x1.4mm^2, slice thickness=2mm, 72 slices, TEs=[5, 10, 16.25]ms
Multitasking (6.9min)	FOV=276x207mm^2, in-plane resolution=0.7x1.4mm^2, slice thickness=2mm, 72 slices, τ=[0, 30, 55, 80]ms, TEs=[5, 10, 16.25]ms

3.2.2.3 In-vivo study

The in-vivo study was approved by the institutional review board at Cedars-Sinai Medical Center. Written informed consent from all subjects were obtained before the study. $N = 10$ healthy

volunteers (age: 41.9 ± 14.6) were recruited. The reference protocols included inversion recovery turbo spin echo (IR-TSE) for T_1 mapping, multi-echo spin echo (ME-SE) for T_2 mapping, and 3D fully flow-compensated multi-echo gradient echo (ME-GRE) for T_2*/QSM mapping, with a total scan time of 20 min. These references were chosen from previous work on T_1/T_2/T_2*/susceptibility mapping (19, 73, 91-95). Note that the T_1/T_2 mapping references were different from those used in the phantom study and had smaller spatial coverage to make scan time feasible. Detailed parameters are listed in Table 3.3. The slice positions of all scans matched with each other.

Table 3.3: Scan parameters for in-vivo study.

In vivo Study Protocols	
Imaging Protocol	**Scan Parameters**
IR-TSE (11.9min)	FOV=276x207mm^2, in-plane resolution=0.7x1.4mm^2, slice thickness=2mm, 24 slices, TIs=[50, 210, 350, 500, 1000, 1500, 2400, 3000]ms, GRAPPA factor=2
ME-SE (4.5min)	FOV=276x207mm^2, in-plane resolution=0.7x1.4mm^2, slice thickness=3.5mm, 40 slices, TEs=[14,28,42,56,70,84]ms, GRAPPA factor=2
ME-GRE (3.5min)	FOV=276x207mm^2, in-plane resolution=0.7x1.4mm^2, slice thickness=2mm, 72 slices, TEs=[5, 10, 16.25]ms
Multitasking (9.1min)	FOV=276x207mm^2, in-plane resolution=0.7x1.4mm^2, slice thickness=2mm, 72 slices, τ=[0, 30, 55, 80]ms, TEs=[5, 10, 16.25]ms

MR Multitasking reconstruction was performed using Equation (3.5) and (3.6), where TV was used as a regularizer. The ranks for spatial and T_1 dimensions were chosen from the -40 dB threshold on the normalized singular value curves of the training data and simulated dictionary, respectively. The rank for T_2 dimension was not truncated as the nuclear norm term in Equation (6) for training tensor completion already performed a soft constraint on the tensor ranks of those

dimensions. Finally, the multi-echo dimension was considered as full rank to account for both T_2* decay and B0 field inhomogeneity.

For comparison purposes, a compressed sensing reconstruction with TV regularizer, a non-regularized low-rank tensor reconstruction (i.e., Equation (3.5) with $\lambda = 0$), and our proposed TV-regularized low-rank reconstruction were performed for several representative T_1/T_2/T_2* contrast combinations on a healthy subject. For the compressed sensing reconstruction, the k-space data along the T_1 dimension were grouped into 8 different inversion times (more typical of conventional T_1 mapping techniques), leading to an acceleration factor of 12.

3.2.3 Image processing and assessment

3.2.3.1 Contrast-weighted image synthesis

Contrast-weighted images were synthesized by substituting the quantitative parameters into the signal equations for common MRI pulse sequences. The sequences used for synthesizing T_1, T_2-weighted, double inversion recovery (DIR), and T_2 fluid-attenuated inversion recovery (FLAIR) images are listed in Table 3.4.

Note that some contrast-weighted images may not need to be re-synthesized using signal equations if they are already available in the reconstructed image series prior to parameter fitting. For example, a T_1-weighted image can be directly obtained by choosing the reconstructed image at the desired inversion time.

For susceptibility-weighted images (SWI), phase masks are created from the high-pass filtered raw phase images and are multiplied by the magnitude images (96). True susceptibility-weighted images (tSWI) have also been generated by using susceptibility maps for the masking process (97). tSWI can enhance the contrast and overcome the limitation of SWI, where the phase images used for masking are dependent not only on susceptibility, but also on shape and orientation of the

structure of interest (97). Both SWI and tSWI are displayed using minimum intensity projections (MinIPs) with an effective slab thickness of 16mm (8 slices). Parameters used for masking are also listed in Table 3.4.

Table 3.4: The sequences and protocols used for synthesizing contrast-weighted images.

Protocols for image synthesis		
Contrast weighted image	**Sequence used for synthesis**	**Parameters used for synthesis**
T_1w	MPRAGE	TI = 960 ms, TR = 2000 ms, TE = 5 ms
DIR	Spin echo	GM: TI1 = 2384 ms, TI2 = 506 ms, TR = 20000 ms WM: TI1 = 3286 ms, TI2 = 861 ms, TR = 20000 ms CSF: TI1 = 1558 ms, TI2 = 449 ms, TR = 20000 ms
T_2w	Spin echo	TR = 8000 ms, TE = 80 ms
T_2-FLAIR	Spin echo	TI = 2000 ms, TR = 8000 ms, TE = 80 ms
SWI		n = 4 multiplications
tSWI		$\chi_1 = 0, \chi_2 = 0.45\ ppm$, n = 2 multiplications

3.2.3.2 Qualitative analysis

All reconstructions were performed on a Linux workstation with a 3.08-GHz dual 16-core Intel Xeon processor equipped with 256 GB RAM and running MATLAB 2016b (MathWorks, Natick, Massachusetts). After finishing the reconstruction, three slices located in the upper, middle and lower brain regions were selected for each healthy subject for multiparametric fitting using Equation (3.7). The generated T_1/T_2/T_2* maps were compared with the corresponding reference maps. Additionally, two slices around subcortical regions were chosen for qualitative evaluation of QSM, SWI, and tSWI.

3.2.3.3 Quantitative analysis

For the phantom study, $T_1/T_2/T_2$*/susceptibility measurements were calculated for each vial. Linear regression was preformed and intraclass correlation coefficients (ICCs) were calculated from a two-way mixed model and 95% confidence using IBM SPSS Statistics (Armonk, New York) to evaluate the agreement between Multitasking and the reference.

For the volunteer study, regions of interest (ROIs) were drawn for cortical GM and WM in both left and right hemisphere for all healthy volunteers. The segmentation was performed by thresholding raw reference/Multitasking images at approximately similar slice locations (12). Mean $T_1/T_2/T_2$* values of cortical GM and WM were calculated and compared between Multitasking and the references. In addition, three different subcortical areas (substantia nigra, red nucleus and globus pallidus) were manually labelled for comparison of susceptibility maps. Bland-Altman analysis was performed and coefficient of variations (CoVs) and ICCs from a two-way mixed model and 95% confidence were calculated to test the agreement between different methods. Two-way repeated measures analysis of variance (ANOVA) was performed using IBM SPSS Statistics (Armonk, New York) to determine the differences between Multitasking and reference.

3.3 Results

3.3.1 Phantom study

Multitasking $T_1/T_2/T_2$* maps showed good quality and qualitative agreement with the reference maps, as shown in Figure 3.3. Substantial correlation (R^2 = 0.997, 0.997, and 0.999 for $T_1/T_2/T_2$*, respectively) and excellent agreement (ICC = 0.991, 0.990, and 0.997 for $T_1/T_2/T_2$*, respectively) were found between Multitasking measurements and the reference measurements.

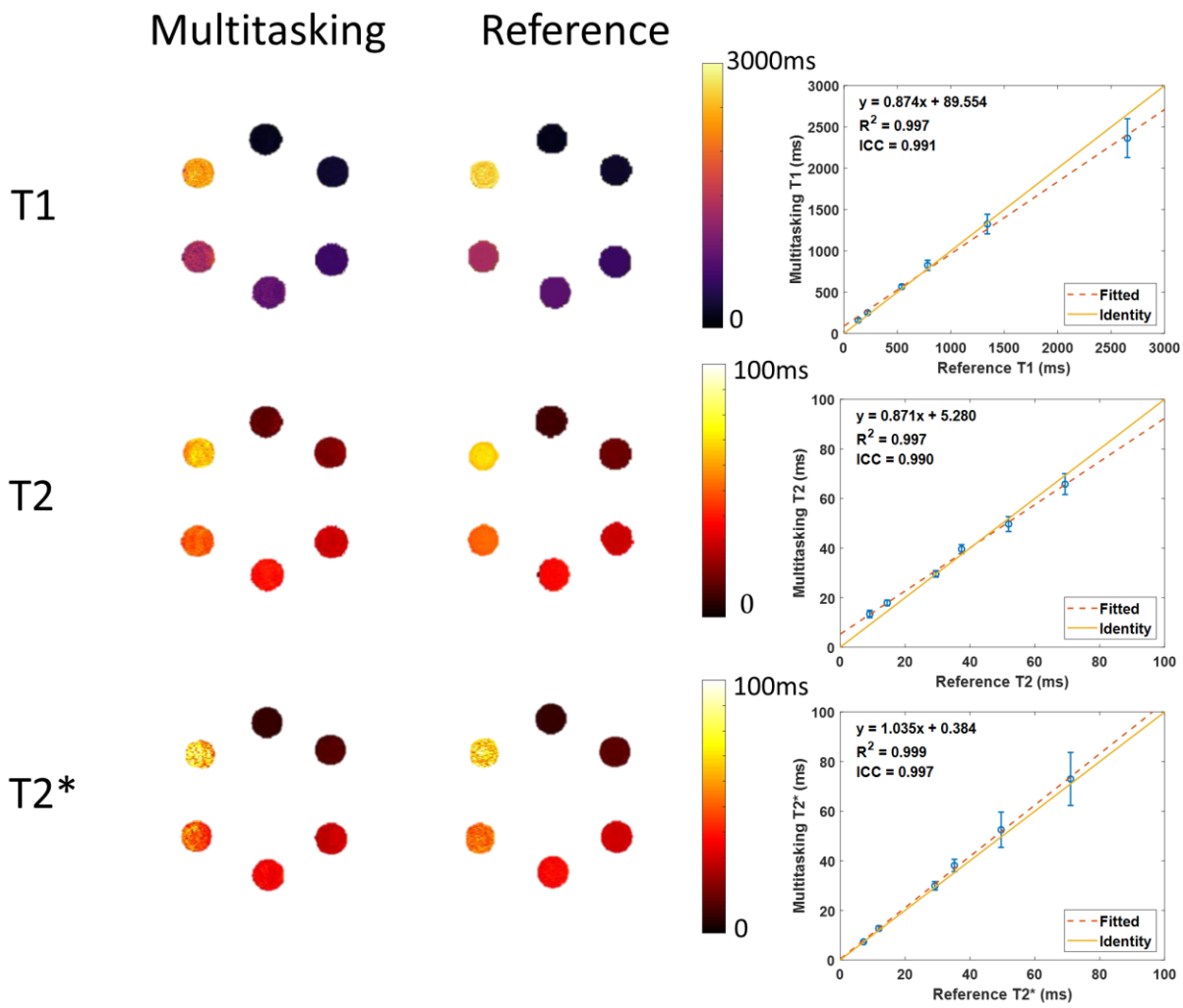

Figure 3.3: Comparison between Multitasking and references on a standard phantom. Multitasking shows comparable image quality and correlates well with the references, as denoted by R^2 and ICC. The solid line represents identity (y = x), and the dotted line represents linear regression fitting.

The susceptibility maps from Multitasking and reference were shown in Figure 3.4A, with the gadolinium (Gd) concentration (in mmol/L) of each vial labelled in the magnitude image. Both maps had good image quality and resembled each other. The correlation plot in Figure 3.4B showed good consistency between Multitasking and reference (R^2=0.988, ICC = 0.994). The susceptibility measurements from Multitasking also correlated well with the Gd concentration

(Figure 4C), yielding a slope of 0.338 ppm per mmol/L. This is consistent with previous literature on Gd phantom (0.326 - 0.350 ppm per mmol/L) (98-100).

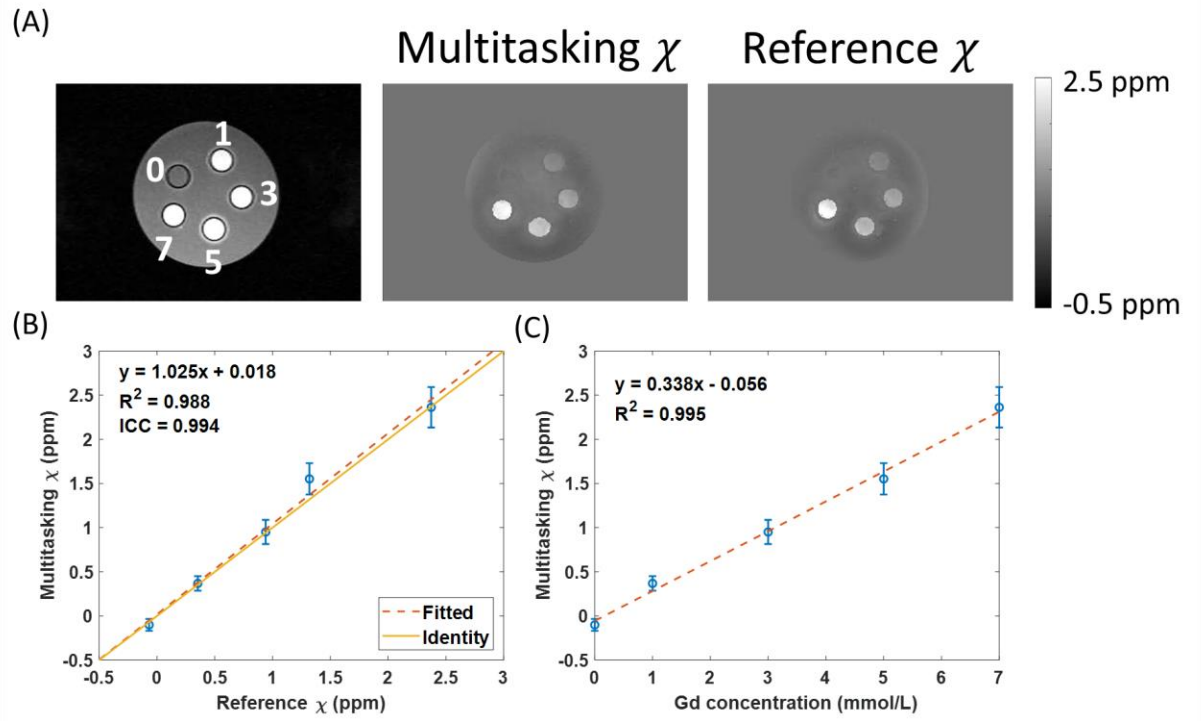

Figure 3.4: (A) Comparison of susceptibility map from Multitasking and references on a Gd phantom, with Gd concentration (in mmol/L) labelled for each tube in the magnitude image. (B) Multitasking susceptibility correlates well with the reference susceptibility, as denoted by R^2 and ICC. The solid line represents identity (y = x), and the dotted line represents linear regression fitting. (C) Multitasking susceptibility correlates well with the Gd concentration and yields a slope of 0.338 ppm per mmol/L. The dotted line represents linear regression fitting.

3.3.2 In-vivo study

Representative images with different contrast combinations reconstructed by compressed sensing only, low-rank only, and low-rank with compressed sensing (our proposed method) are in Figure 3.5. The high acceleration factor made reconstruction challenging for compressed sensing and the results showed poor image quality and aliasing artifacts. Low-rank tensor reconstruction generated aliasing-free images but were noisy, especially for images at short T_1. The proposed

reconstruction taking advantage of both the low-rank property and spatial regularization had the best image quality with minimal noise and aliasing.

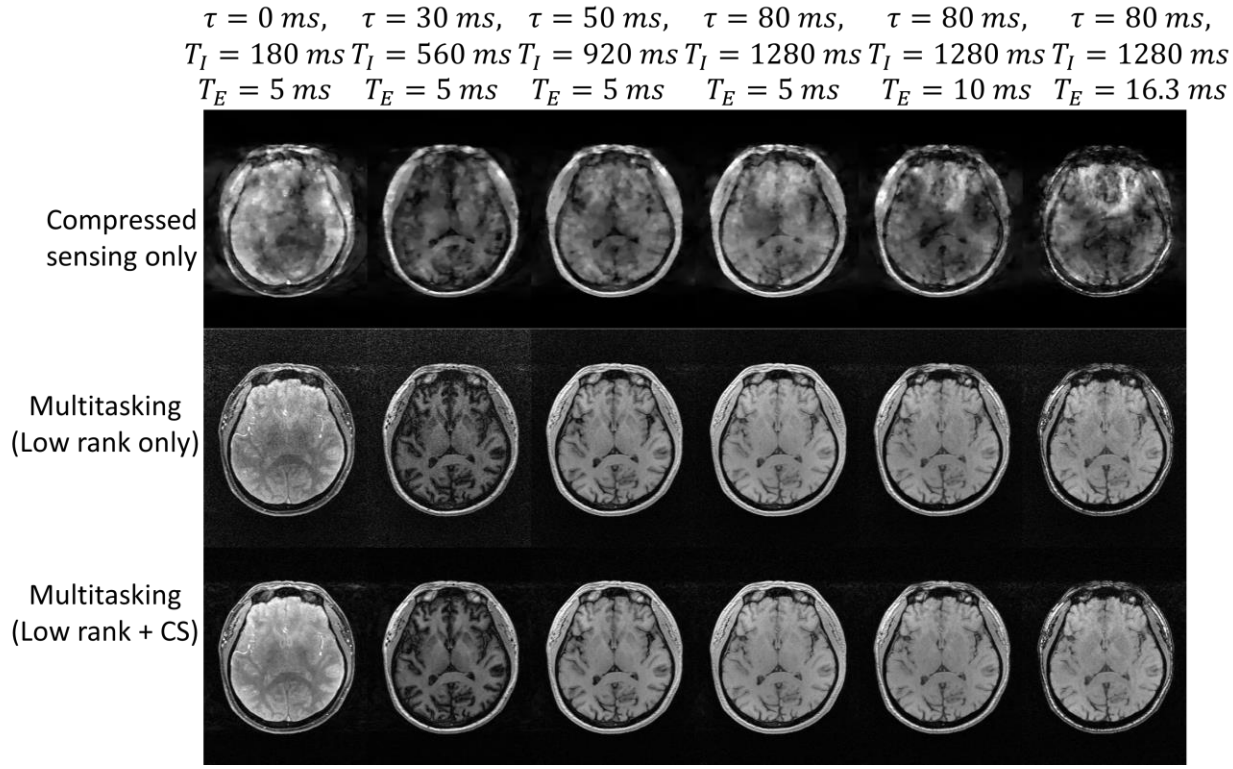

Figure 3.5: Comparison of compressed sensing reconstruction (1st row), low-rank tensor reconstruction (2nd row), and Multitasking reconstruction (3rd row) for representative contrast weightings. The high acceleration factor ($8 \cdot 4 \cdot 3 \cdot N_y \cdot N_z/144/192/3 = 12$) made reconstruction challenging for compressed sensing, leading to low-quality images corrupted by noise and aliasing artifacts. Results from low-rank reconstruction were free of aliasing but noisy. Among all, Multitasking showed best image quality by combing the low-rank tensor model and spatial regularization.

As shown in Figure 3.6, Multitasking generated co-registered multiparametric maps qualitatively matched with the reference ones. Bland-Altman plots for $T_1/T_2/T_2$* were shown in Figure 3.7A-C. Compared with reference methods, Multitasking values are 6% higher in T_1, 4% lower in T_2 and T_2*. Table 3.5 provided the results of two-way ANOVA, which showed significant differences among different methods for T_1, T_2, and T_2* ($P \leq 0.008$). The distributions of $T_1/T_2/T_2$* measurements from the two methods were summarized in Table 3.6. Despite the differences

between the two methods, all the values were still within the ranges from literature (GM T_1: 1209-1700 ms; WM T_1: 750-1110 ms; GM T_2: 71-132 ms; WM T_2: 56-84 ms; GM T_2*: 40-65 ms; WM T_2*: 44-52 ms).(101-107) Additionally, CoVs (< 5%) and ICCs (> 0.75) indicated the excellent consistency between Multitasking and reference techniques (108).

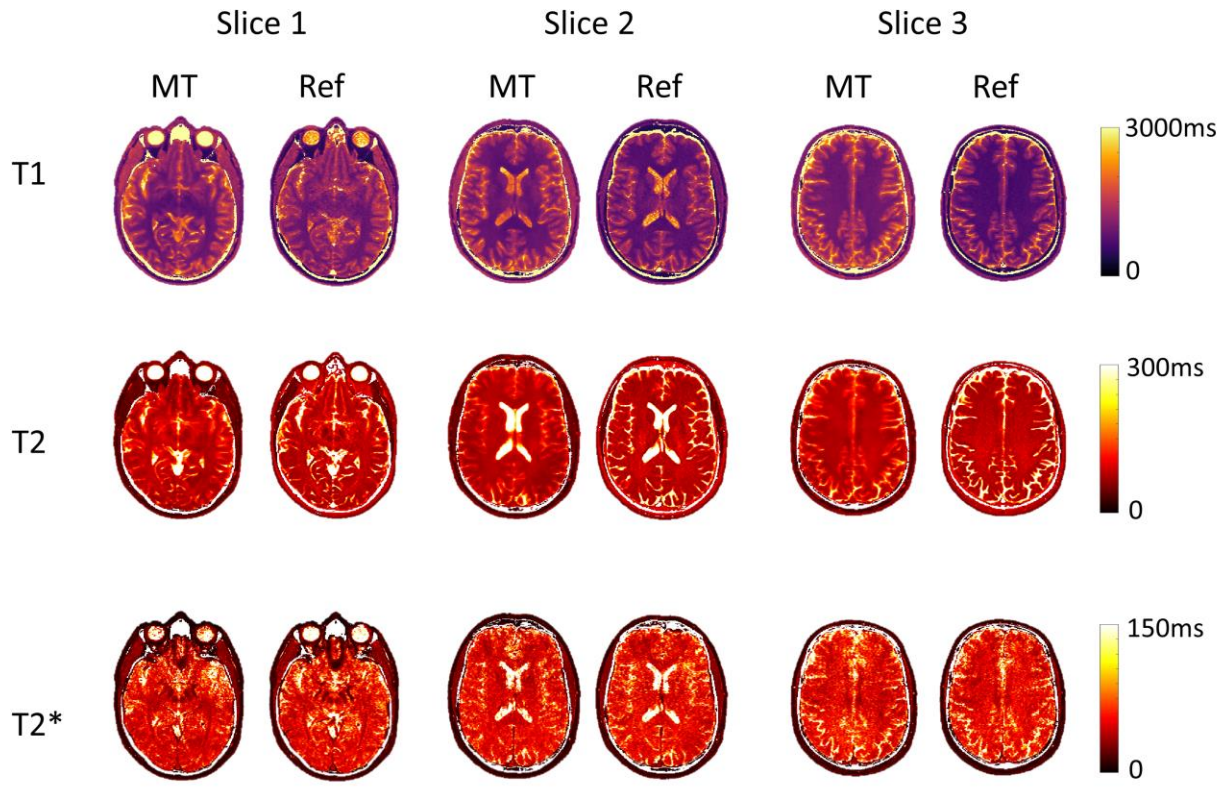

Figure 3.6: Representative in-vivo T_1/T_2/T_2* mapping at three slice locations using MR Multitasking (MT) and the corresponding reference (Ref) protocols for a healthy volunteer. Multitasking provides T_1/T_2/T_2* maps with good qualitative agreement with the references.

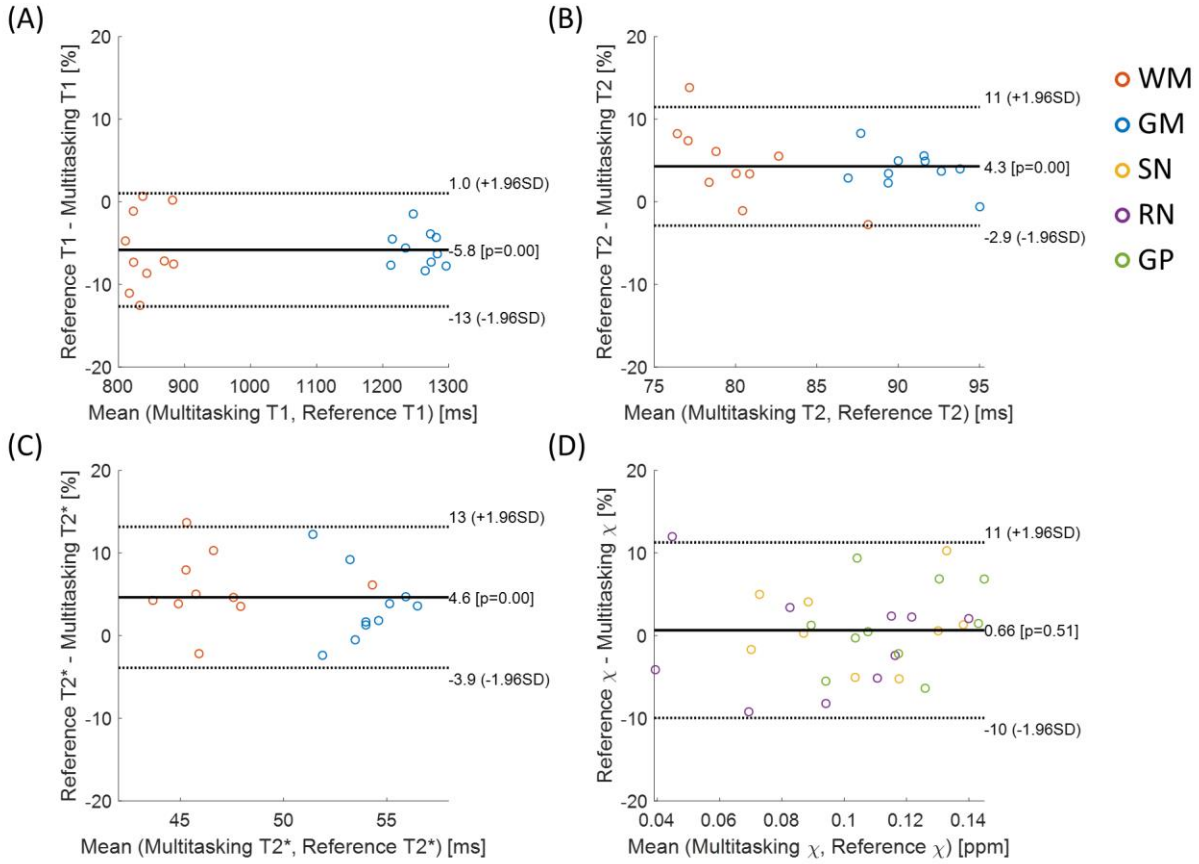

Figure 3.7: Bland - Altman plots comparing Multitasking (A) T_1, (B) T_2, (C) T_2*, and (D) susceptibility measurements with those of the references (N=10). The dotted lines represent 95% confidence level. The solid lines represent mean percentage differences.

Table 3.5: Two-way ANOVA test for T_1/T_2/T_2*/susceptibility. Significant differences were found between different tissues and different methods for T_1/T_2/T_2* measurements. No significant differences were found between different methods for susceptibility.

	Source	**Sum of Squares**	**Degrees of Freedom**	**F**	**P**
T_1	Method	0.037	1	34.455	<0.001
	Tissue	1.730	1	1611.406	<0.001
T_2	Method	1.280×10^{-3}	1	11.004	0.002
	Tissue	1.169×10^{-3}	1	100.421	<0.001

T_2*	Method	$5.252x10^{-5}$	1	7.757	0.008
	Tissue	$5.320x10^{-4}$	1	78.532	<0.001
QSM	Method	$1.244x10^{-5}$	1	0.016	0.900
	Region	$5.344x10^{-3}$	2	3.448	0.039

Table 3.6: T_1/T_2/T_2*/susceptibility measurements of N=10 healthy volunteers using Multitasking and the references along with ICC and CoV between different methods.

		Multitasking	**Reference**	**ICC**	**CoV**
T_1 (ms)	GM	1293.7 ± 35.1	1221.8 ± 29.5	0.950	4.77%
	WM	866.7 ± 30.8	817.0 ± 35.3		
T_2 (ms)	GM	89.0 ± 3.2	92.6 ± 2.4	0.781	3.94%
	WM	78.2 ± 5.0	81.8 ± 2.5		
T_2* (ms)	GM	53.1 ± 2.1	55.0 ± 1.8	0.794	4.45%
	WM	45.4 ± 3.0	48.1 ± 3.2		
QSM (ppm)	SN	0.108 ± 0.027	0.110 ± 0.029	0.981	3.79%
	RN	0.094 ± 0.034	0.093 ± 0.034		
	GP	0.115 ± 0.019	0.117 ± 0.021		

Two slices of QSM maps were shown in Figure 3.8. Both Multitasking and reference maps clearly visualized the deep gray matter structure. The same structures as well as vessels could also be found in MinIPs of SWI and tSWI images. Multitasking qualitatively agreed with reference in all maps and images. Bland-Altman plot for susceptibility shown in Figure 3.7D indicated little bias between Multitasking and reference methods. As shown in Table 3.5, no significant difference was found between the two methods (P = 0.900) with two-way ANOVA. The susceptibility values and their distributions were summarized in Table 3.6. These measurements were consistent with

the reference ones (CoV < 5%, ICC > 0.95) and literature values (SN: 0.083-0.115 ppm, RN: 0.076-0.120 ppm, GP: 0.093-0.123 ppm) (69, 87, 109-111).

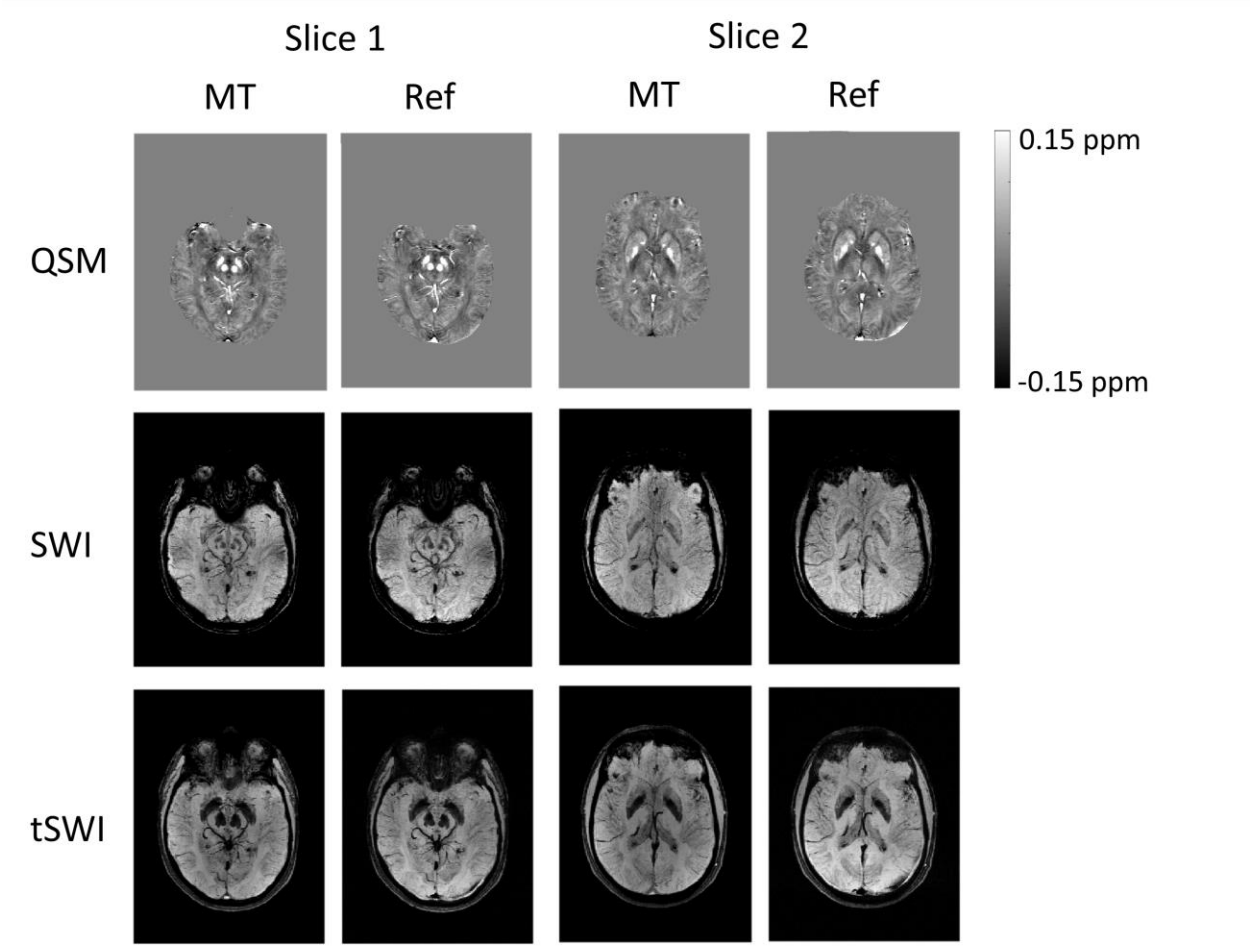

Figure 3.8: Representative in-vivo QSM at two slice locations using MR Multitasking (MT) and references (Ref) on the same healthy volunteer. Both QSM and SWI/ tSWI (MinIP) images agreed with the reference in terms of deep gray matter and vessel visualization.

Quantitative maps and six contrast-weighted images of a healthy volunteer were generated from Multitasking and were shown in Figure 3.9. As a byproduct from Equation (3.7), static field inhomogeneity ΔB_0 and equilibrium magnetization M_0 were also shown. T_1-weighted image synthesized based on the Bloch equations were compared with the one directly taken from reconstructed series in Figure 3.10, which showed very similar contrast. DIR images with WM

and CSF enhanced separately were shown in Figure 3.11. All images and maps showed appropriate image contrasts.

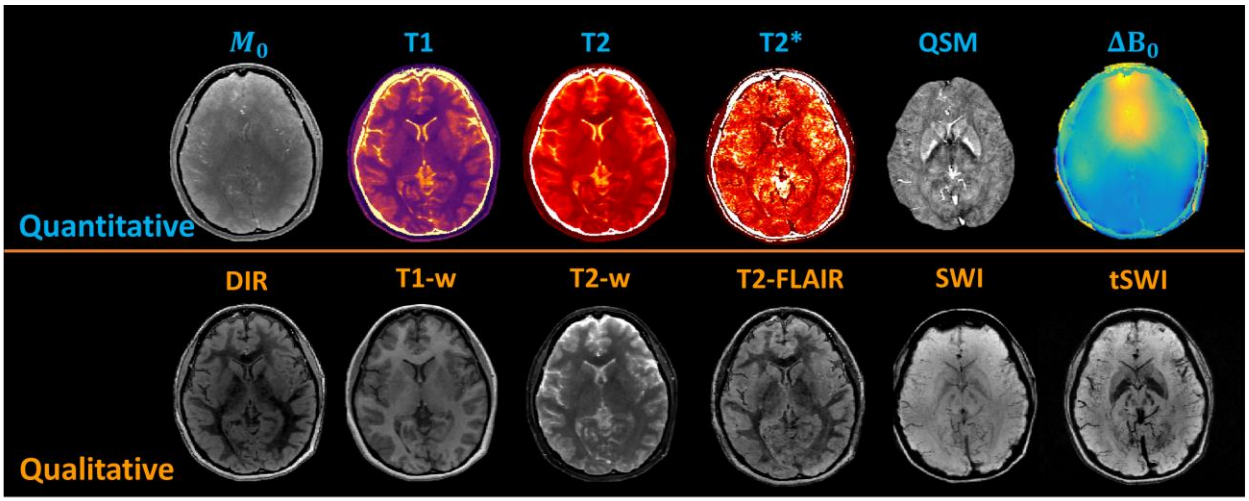

Figure 3.9: Results from a healthy volunteer including qualitative images and quantitative maps. The first row included quantitative maps and the second row showed all the weighted images. SWI and tSWI were MinIP results with an effective slab thickness of 16mm.

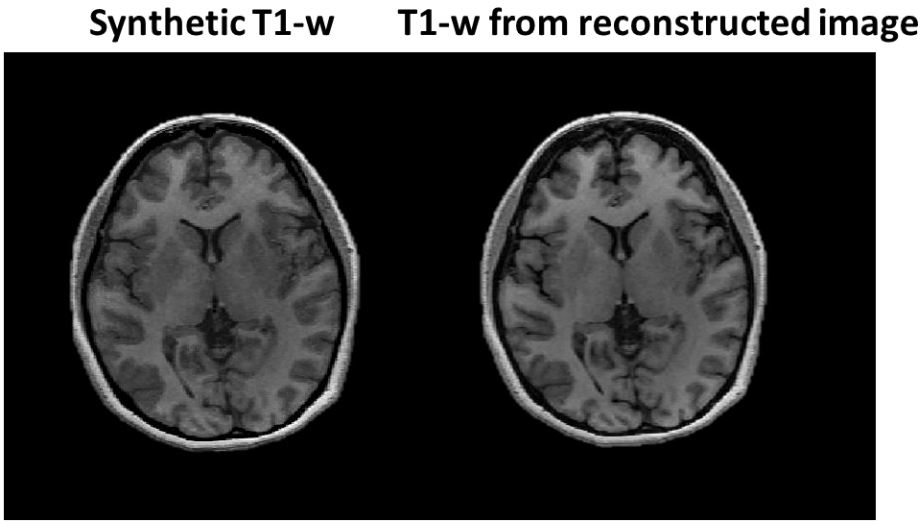

Figure 3.10: Synthetic T_1-w image and T_1-w image directly taken from reconstructed image series.

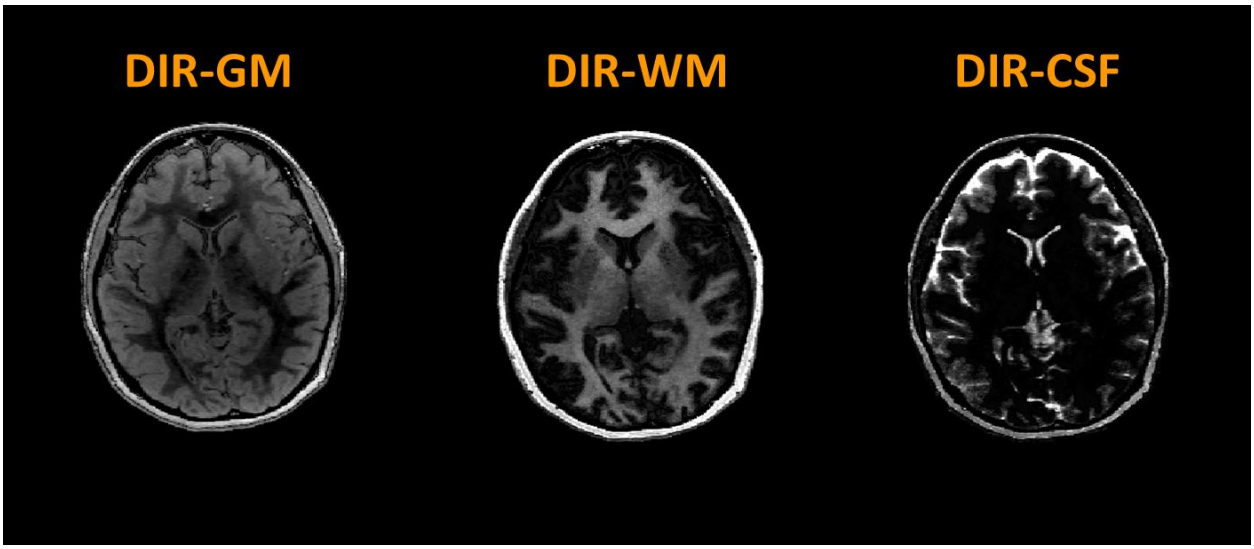

Figure 3.11: Synthesized DIR images with GM, WM, CSF enhanced, respectively.

3.4 Discussion

In this work, we developed a 3D fully flow-compensated Multitasking $T_1/T_2/T_2$*/QSM mapping technique. Validation was performed with numerical simulations, phantom, and volunteer studies. Quantitative in vivo measurements showed substantial agreement between Multitasking and the reference methods. Conventional multiparametric mapping techniques in the brain require separate scans, which is time consuming and can suffer from inter-scan misregistration and intra-scan motion. In comparison, our technique performs co-registered whole brain multiparametric mapping within a single 9.1-min scan and is two times as fast as the reference techniques (20 min) used in this study. The high-dimensional contrast encoding approach in Multitasking has further potential for resolving sub-voxel structure through relaxation correlation spectroscopy (112), which would otherwise become an ill-posed problem with 1D relaxation imaging methods (113-115).

To the best of our knowledge, this is the first technique for whole brain, simultaneous mapping of T_1, T_2, T_2*, and susceptibility. STAGE (15-17) achieves whole brain T_1/T_2*/QSM mapping at

the same resolution within 5 minutes, while multi-echo MP2RAGE technique performs T_1/T_2*/QSM mapping at a higher resolution (0.64 mm^3) within 16 minutes (20). In a more recent work, the scan time of multi-echo MP2RAGE is shortened to 8.5 minutes (19). However, the choice of very short last TE (~9ms) negatively impacts accuracy of T_2* estimation (20). Furthermore, none of the techniques performs T_2 quantification, and thus provide incomplete information for brain tissue characterization, as T_2-weighted and T_2-FLAIR images play a critical role in studying white matter disease and tumor imaging (116-118). And the multitasking approach presented herein offers a distinct advantage. Recent fingerprinting work has achieved joint T_1, T_2, and T_2* mapping, yet has limitations including 2D acquisition, long scan time (35s per slice), and no susceptibility information (78).

Multitasking T_1, T_2, T_2* and QSM maps show good consistency with the references. Nevertheless, small but significant biases were found in T_1/T_2/T_2* measurements between Multitasking and the references. Possible reasons include: (1) IR-TSE is known to underestimate T_1 compared to IR-SE due to slice interference (119). (2) T_2 differences could be caused by the sensitivity of the Multitasking preparation scheme (T_2-IR) to B_1 inhomogeneity (120) and the possible overestimation of ME-SE from stimulated echo contamination (121). (3) Remaining phase drifting during a long scan could cause phase cancellation effects, leading to T_2* underestimation. Further technical improvements may be able to compensate these effects. Despite the differences, CoVs and ICCs still indicate substantial quantitative agreement between the two methods and measurements from both methods were in the range of previous literature.

Six different contrast-weighted images were generated from Multitasking quantitative maps. Although all images show correct contrast, it should be noted that our synthetic FLAIR image still requires further improvement to match the clinical standards. The challenge of synthesizing T_2-

FLAIR has also been mentioned by others (122, 123) and can be related to partial volume, flow, and magnetization transfer effects. Better results may be obtained with the help of deep learning (122). Image synthesis has also been explored by previous MR fingerprinting work and by STAGE (15-17, 124). Compared to previous work, Multitasking provides an alternative for certain contrast weighted images. In this work we demonstrate that a decent T_1-weighted image can be directly obtained from the reconstructed image series without requiring synthesis. This may help to overcome the challenges related to Bloch synthesis (e.g., flow, magnetization transfer) and produce more 'natural' image contrast.

One future direction for this work is to increase spatial resolution to 1.0 mm isotropic resolution while retaining a reasonable scan time. The current resolution may still cause partial volume effects and missing of small lesions and bleeds. Scan time also limits the choice of TE and TR. The longest TE adopted in the current protocol matches with previous work (15, 18), but may still need lengthening to improve estimation for WM and GM T_2* values (20). Making this change would result in even longer scan time. Further technical improvement may be made by incorporating other prior knowledge including conjugate symmetry (125) and locally low rankness (126) for a shorter scan. For T_2* mapping particularly, B0 inhomogeneity correction along the gradient echo correction may help to improve the low-rank property and further cut down scan time. Deep learning-based methods like super-resolution are also potential avenues to improve spatial resolution (127, 128). In this study, we did not investigate the robustness of our sequence to motion, which can be important during a long scan or for pediatric/patient population (14, 129). However, we note that the Multitasking framework has been demonstrated to support several motion-handling techniques to produce motion-robust maps, such as automatically identifying and removing motion-corrupted data (25, 130) or by modelling motion as a separate dimension in the

tensor form (60, 131, 132). Finally, clinical validations would be performed in the future to investigate the usefulness of the technique for diagnostic purposes.

3.5 Conclusion

We have developed a three-dimensional, whole brain simultaneous $T_1/T_2/T_2$*/susceptibility mapping method in a single 9.1-min scan based on the MR Multitasking framework. The technique can retrospectively generate six different contrast-weighted images in addition to the four quantitative maps.

CHAPTER 4 Free-breathing, non-ECG, simultaneous myocardial T_1, T_2, T_2*, and fat-fraction mapping

4.1 Introduction

Quantitative parametric mapping has gained increasing interest and attention in the clinical practice of cardiovascular magnetic resonance imaging (MRI) because of its ability to provide insight into causes of non-ischemic and ischemic cardiomyopathies as well as its potential promise to elucidate disease processes involving the myocardial microvasculature. Quantification provides an objective assessment of disease progress (133, 134) and is sensitive to mild or diffuse tissue alterations (135, 136). Parametric mapping of T_1 and T_2 is capable of detecting fibrosis (1, 2), edema (3-5), whereas T_2* mapping quantifies cardiac iron concentration, which is essential for evaluating β-thalassemia major and sickle cell anemia (6, 137, 138). Myocardial fat content is associated with heart failure (139) and is of high prevalence in chronic myocardial infarction (140) and nonischemic cardiomyopathies (10) such as arrhythmogenic right ventricular dysplasia.

Several mapping techniques have previously been used for myocardial characterization, including T_1 mapping using Modified Look-Locker inversion recovery (MOLLI) (141) or saturation recovery single-shot acquisition (SASHA) (142), T_2 mapping with T_2-prepared balanced SSFP (143), and T_2* mapping with multi-echo gradient recalled echo (GRE) (6). However, these methods must be used with breath-holding and electrocardiogram (ECG) triggering to minimize respiratory and cardiac motion effects. Furthermore, separate acquisitions are needed for mapping separate parameters, resulting in potential misaligned maps and variable breath-holding quality.

Free-breathing techniques for cardiac parametric mapping have been developed using respiratory gating (22, 23, 144), bellows (145) or respiratory self-navigation signals (146, 147). However, respiratory gating is inefficient and can lead to long and unpredictable scan time, as data is only acquired in short windows dependent on individual subject motion. Bellows only provide a relative measure of respiratory motion rather than an absolute measure of diaphragmatic motion, which can lead to errors in respiratory motion identification (148). Respiratory self-navigation can address some of these issues but does not reach 100% acquisition efficiency unless it is also paired with cardiac self-navigation. The above mapping techniques all rely on less-efficient ECG gating, which is prone to errors at high field strengths (57) and for patients with arrhythmia (149).

Free-breathing, non-ECG cardiac T_1 and T_2 mapping has been achieved using the MR Multitasking framework (24, 150), which models the underlying image as a low-rank tensor and acquires training data to identify and resolve cardiac and respiratory motion. However, this framework has yet to include T_2* and fat fraction (FF) mapping in the heart. Multi-echo extensions of Multitasking for T_1, T_2, and T_2* mapping in the brain (151) and T_1, R_2*, and FF mapping in the liver (152) have been described. However, adding multiple echoes after every excitation pulse comes at the price of prolonged scan time and reduced temporal resolution, limiting the direct translation of these multi-echo extensions to cardiac imaging.

To address several limitations of prior techniques and to tailor the multitasking framework for multiparametric myocardial mapping, we developed a new technique based on MR Multitasking for the joint mapping of myocardial T_1, T_2, T_2*, and FF from a free-breathing, non-ECG triggered, 2D single slice acquisition. This technique includes (1) hybrid T_2prep/IR (T_2IR) preparations and multi-echo readouts to sample T_1, T_2, and T_2* relaxations; (2) a variable T_R (VTR) scheme alternating between single-echo and multi-echo readouts, for improved temporal resolution and

shorter scan time; (3) low-rank tensor (LRT) modeling to reconstruct the underlying images; and (4) a chemical-shift based method (153) for water and fat separation. The performance of the proposed technique was evaluated on phantom, healthy volunteers, symptomatic patients suffering from post-acute sequela of COVID (PASC), and ischemic heart disease (IHD) patients with ferumoxytol enhancement.

4.2 Methods

4.2.1 Imaging framework

4.2.1.1 Sequence diagram

The sequence diagram used in this work is shown in Figure 4.1A. The acquisition cycles through hybrid T_2IR modules with five different preparation durations (τ , with $\tau = 0$ corresponding to a standard IR pulse), with FLASH excitations for data readout filling the entire recovery period between preparation pulses. Two interleaved datasets are collected during the continuous acquisition: the training data ($\mathbf{d}_{\mathrm{tr}}$) are frequently collected at k-space center (0° radial spoke) to provide temporal information; the imaging data ($\mathbf{d}_{\mathrm{img}}$) are collected with golden-angle radial trajectory to provide spatial information. In previous MR Multitasking work for T2* mapping (151, 152), multi-echo readouts were used for both training and imaging data (Figure 4.1B), which limited the temporal resolution and imaging efficiency. To achieve a higher temporal resolution to characterize cardiac motion, instead of using constant T_R (CTR) for both datasets, a variable T_R (VTR) scheme was developed in this work, where the training data are collected using a single-echo, short T_R readout and imaging data are collected using a multi-echo, long T_R readout (Figure 4.1C).

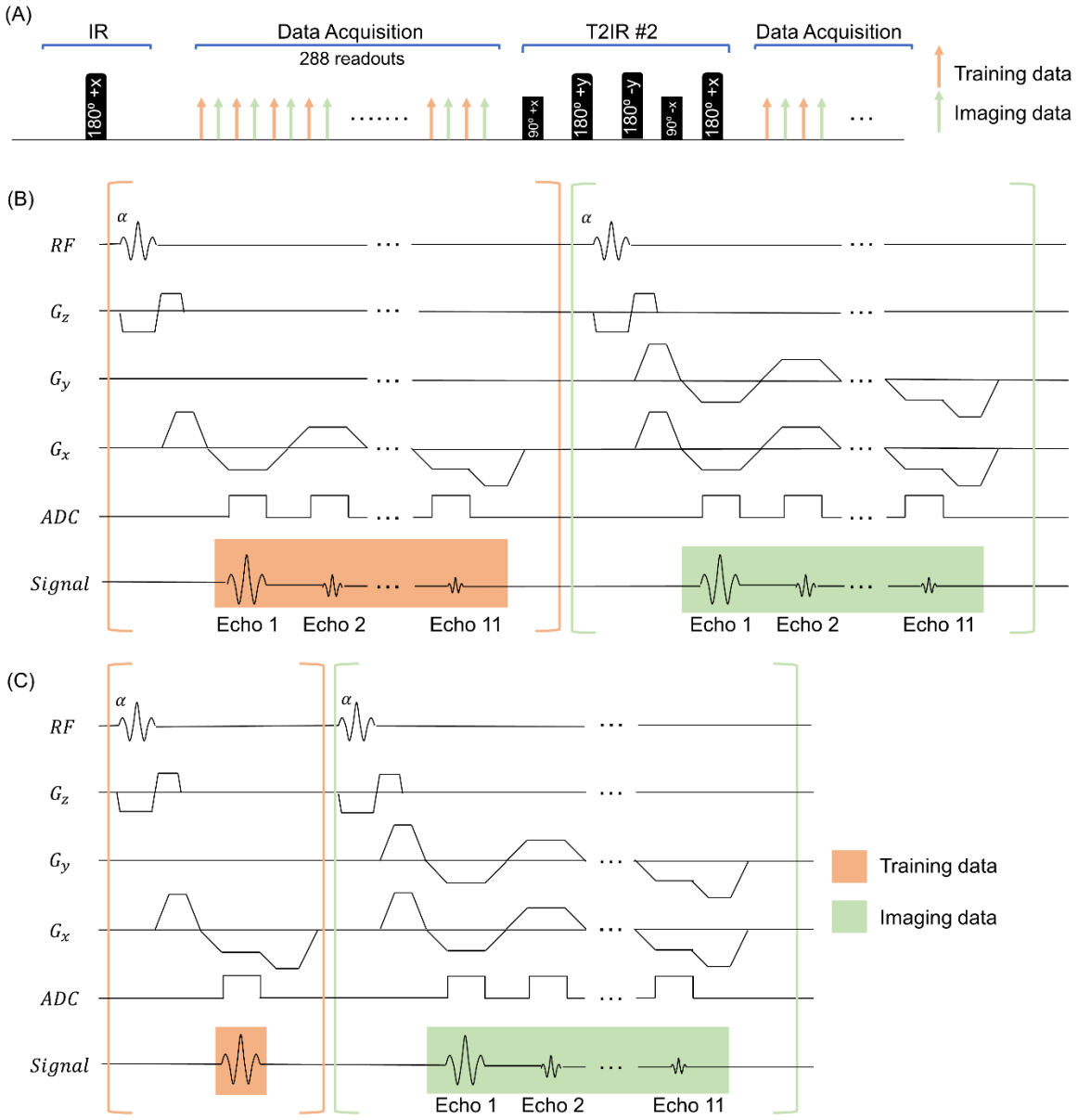

Figure 4.1: (A) Sequence diagram for the proposed multitasking $T_1/T_2/T_2^*$/FF mapping framework. Hybrid IR/T_2IR preparation modules were followed by 288 FLASH readouts, which enable collection of k-space lines with different $T_1/T_2/T_2^*$ contrasts. The training data was acquired every other readout. (B) Illustration of constant T_R (CTR) readout module, which used multi-echo readouts for both training and imaging data. (C) Illustration of variable T_R (VTR) readout module, which used a single-echo readout for training data and multi-echo readouts for imaging data.

Representative signal curves for CTR and VTR Multitasking for T_1 = 1.2s, T2 = 0.04s and five different T_2IR modules are exemplified and compared in Figure 4.2.

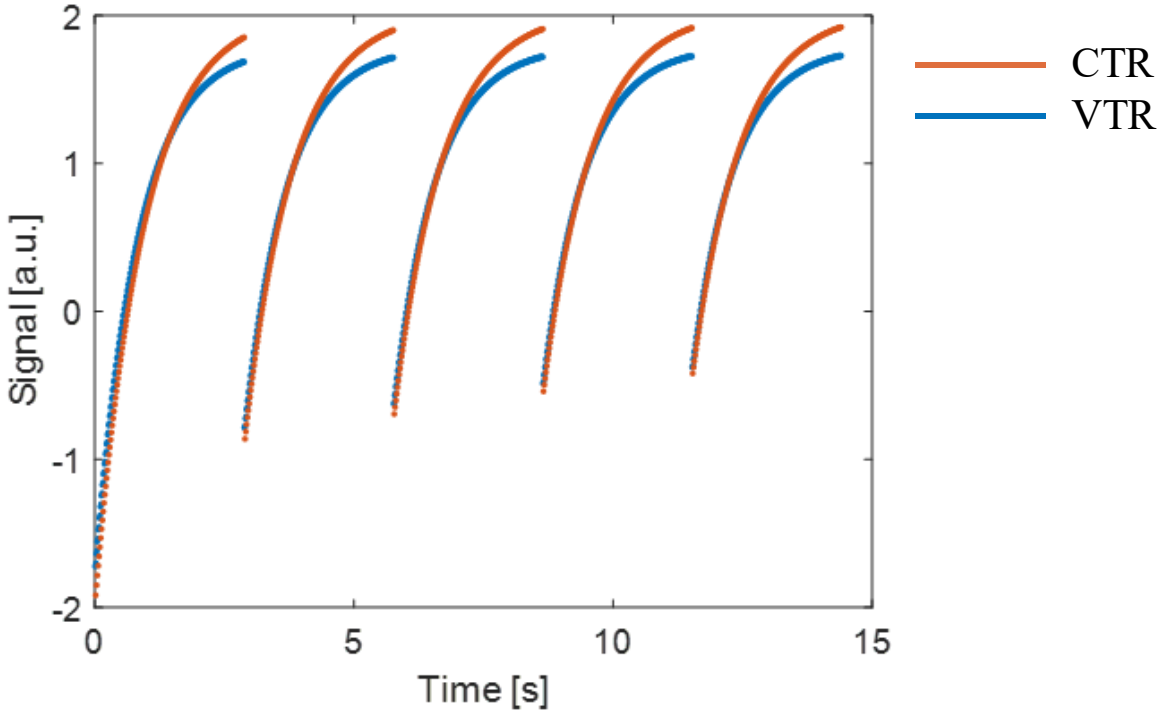

Figure 4.2: Representative signal curves of CTR and VTR Multitasking (only showing the first echo) for T_1 = 1.2s, T2 = 0.04s and five different T_2IR modules.

4.2.1.2 Low-rank tensor imaging model

The MR Multitasking framework models the underlying image as a 7D image $x(\mathbf{r}, T_c, T_r, \tau, T_I, T_E)$ with two spatial dimensions indexed by $\mathbf{r} = [x, y]$, and five temporal dimensions describing cardiac motion, respiratory motion, T_2 preparation, T_1 recovery, and gradient echo dynamics (T_2* decay and fat–water shift), indexed by T_c, T_r, τ, T_I, and T_E, respectively. By taking advantage of the spatial-temporal correlations (154), the image can be factorized as:

$$x(\mathbf{r}, T_c, T_r, \tau, T_I, T_E) = \sum_{\ell=1}^{L} u_\ell(\mathbf{r}) \phi_\ell(T_c, T_r, \tau, T_I, T_E), \quad (4.1)$$

$$\phi_\ell(T_{\mathrm{c}},T_{\mathrm{r}},\tau,T_{\mathrm{I}},T_{\mathrm{E}}) = \sum_{j=1}^{J}\sum_{k=1}^{K}\sum_{m=1}^{M}\sum_{n=1}^{N}\sum_{p=1}^{P} g_{\ell jkmnp}\, c_j(T_{\mathrm{c}}) r_k(T_{\mathrm{r}}) v_m(\tau) w_n(T_{\mathrm{I}}) q_p(T_{\mathrm{E}}), \qquad (4.2)$$

where $\{u_\ell(\mathbf{r})\}_{\ell=1}^{L}$ represent spatial coefficients and $\{(\phi_\ell(T_c,T_r,\tau,T_I,T_E)\}_{\ell=1}^{L}$ represent temporal functions which can be further decomposed into a core tensor $\mathcal{G}$ with elements $g_{\ell jkmnp}$ and individual bases for each temporal dimension: $\{c_j(T_c)\}_{j=1}^{J}$, $\{r_k(T_r)\}_{k=1}^{K}$, $\{v_m(\tau)\}_{m=1}^{M}$, $\{w_n(T_{\mathrm{I}})\}_{n=1}^{N}$, and $\{q_p(T_{\mathrm{E}})\}_{p=1}^{P}$ (155). The combination of Equations (4.1) and (4.2) suggests that a discretized image tensor $\mathcal{X}$ with elements $x_{ijkmnp} = x(\mathbf{r}_i, T_{\mathrm{c,j}}, T_{\mathrm{r},k}, \tau_m, T_{\mathrm{I},n}, T_{\mathrm{E},p})$ can be decomposed in Tucker form (62, 63) as follows:

$$\mathcal{X} = \mathcal{G} \times_1 \mathbf{U} \times_2 \mathbf{C} \times_3 \mathbf{R} \times_4 \mathbf{V} \times_5 \mathbf{W} \times_6 \mathbf{Q}, \qquad (4.3)$$

where the columns of **U**, **C**, **R**, **V**, **W**, and **Q** contain the basis functions for each corresponding dimension.

In MR Multitasking, the core tensor and temporal bases are often extracted from the training data, as will be described in the next section. However, because our VTR scheme collects only a single-echo readout for training data, multi-echo temporal information to determine **Q** and the 6th dimension of $\mathcal{G}$ will not be available. Therefore, we instead individually decompose each tensor $\mathcal{X}_p$, the subset of the image tensor $\mathcal{X}$ at the p^{th} echo:

$$\mathcal{X}_p = \tilde{\mathcal{G}} \times_1 \mathbf{U}_p \times_2 \mathbf{C} \times_3 \mathbf{R} \times_4 \mathbf{V} \times_5 \mathbf{W}, \qquad (4.4)$$

where $\tilde{\mathcal{G}}$ is an updated core tensor without a gradient-echo dimension, and $\mathbf{U}_p$ are the spatial coefficients for the pth echo. All echoes share the motion bases and T_1 and T_2 relaxation bases, as changes in motion and T_1/T_2 relaxation are negligible on the time scale between echoes.

4.2.1.3 Image reconstruction

This work adopts a similar strategy for MR Multitasking image reconstruction to previously published methods (24, 150, 156, 157). Briefly, this reconstruction workflow (1) predetermines the T_1 and T_2 temporal basis functions in **V** and **W** from a dictionary of signal curves, (2) reconstructs "real-time" images and perform motion binning, (3) recovers the missing elements in the training dataset, (4) estimates the cardiac basis functions in **C**, respiratory basis functions in **R**, and core tensor $\tilde{\mathcal{G}}$ from training data, and (5) solves spatial coefficients $\mathbf{U}_p$ for each echo from imaging data.

A dictionary of feasible T_2IR GRE signal curves is generated using the sequence parameters and a range of T_1/T_2 and B_1 inhomogeneity values based on the Bloch equations (24, 150, 157). The dictionary consists of 21 T_1 values logarithmically spaced from 100 ms to 3000 ms, 21 T_2 values logarithmically spaced from 10 ms to 3000 ms, 10 flip angles equally spaced between 0.5° to 5°, and 6 inversion efficiency factors equally spaced between -1 (perfect inversion) and -0.5. The T_1 basis functions in **W** and T_2 basis functions in **V** are obtained from the high-order SVD (HOSVD) (84) of the dictionary.

The second reconstruction step is to generate ungated images with an explicit low-rank matrix imaging strategy. The 'real-time' (ungated) temporal basis functions are estimated from singular value decomposition (SVD) of the training data. It has only one dimension representing the elapsed acquisition time and is similar to ϕ_ℓ in Equation (4.1). The spatial coefficients can therefore be estimated through a least-squares fitting to the imaging data.

A modified k-means clustering algorithm as previously described (24) is used to automatically place the corresponding images into 6 respiratory bins and 20 cardiac bins. To address the changing contrast weightings after the preparation pulses, the centroids solved in each iteration at different

contrast combinations are constrained by the pre-determined T_1/T_2 bases $\mathbf{V}$ and $\mathbf{W}$. Respiratory motion is identified first, and the respiratory bins assigned at each iteration are low-pass filtered with 50 Hz cutoff frequency. Then cardiac motion is binned with the same algorithm, expect that the cardiac bins are band-pass filtered with range of 50 – 130 Hz (a range for possible heart rates).

The training tensor $\mathcal{D}_{\mathrm{tr}}$, as expressed in $(\mathbf{k}, T_{\mathrm{c}}, T_{\mathrm{r}}, \tau, T_{\mathrm{I}})$-space, can still be undersampled as training data acquisition cannot typically cover every combination of cardiac phase, respiratory phase, T_2-IR prep duration, and inversion time. We apply a small-scale low-rank tensor completion algorithm by solving the optimization problem below:

$$\widehat{\mathcal{D}}_{\mathrm{tr}} = \arg \min_{\substack{\mathcal{D}_{\mathrm{tr}}, \text{ s.t.} \\ \mathbf{D}_{\mathrm{tr},(4)} \in \text{ range}(\mathbf{V}), \\ \mathbf{D}_{\mathrm{tr},(5)} \in \text{ range}(\mathbf{W})}} \|\mathbf{d}_{\mathrm{tr}} - \Omega_{\mathrm{tr}}(\mathcal{D}_{\mathrm{tr}})\|_2^2 + \lambda \sum_{i=1}^{3} \left\|\mathbf{D}_{\mathrm{tr},(i)}\right\|_* + R_{\mathrm{t}}(\mathcal{D}_{\mathrm{tr}}), \tag{4.5}$$

where $\mathbf{d}_{\mathrm{tr}}$ is the collected training data, $\Omega_{\mathrm{tr}}(\cdot)$ is the sampling operator for the training dataset, $\mathbf{D}_{\mathrm{tr},(i)}$ is the mode-i unfolding of the complete training tensor, $\|\cdot\|_*$ denotes the matrix nuclear norm, and $R_{\mathrm{t}}(\cdot)$ is a temporal regularizer, which in this work is chosen as temporal total variation (TV) along the respiratory and cardiac dimensions. Once the training tensor is completed, the cardiac basis functions in $\mathbf{C}$, respiratory basis functions in $\mathbf{R}$, and core tensor $\tilde{\mathcal{G}}$ can be extracted from the HOSVD of $\mathcal{D}_{\mathrm{tr}}$.

Finally, we solve the spatial coefficients $\mathbf{U}$ echo-by-echo:

$$\widehat{\mathbf{U}}_p = \arg\min_{\mathbf{U}_p} \left\|\mathbf{d}_{\mathrm{img},p} - \Omega\left(\widehat{\Phi} \times_1 \mathbf{FSU}_p\right)\right\|_2^2 + \lambda R_{\mathrm{s}}(\mathbf{U}_p), \tag{4.6}$$

for known temporal factor tensor $\widehat{\Phi} = \tilde{\mathcal{G}} \times_2 \mathbf{C} \times_3 \mathbf{R} \times_4 \mathbf{V} \times_5 \mathbf{W}$, where $\mathbf{d}_{\mathrm{img},p}$ is the imaging data at the p^{th} echo, and $R_{\mathrm{s}}(\cdot)$ is a wavelet sparsity regularizer. The reconstructed image tensor for the p^{th} echo is then given by the product $\widehat{\mathcal{X}}_p = \widehat{\Phi} \times_1 \widehat{\mathbf{U}}_p$.

A flow chart for image reconstruction can be found in Figure 4.3.

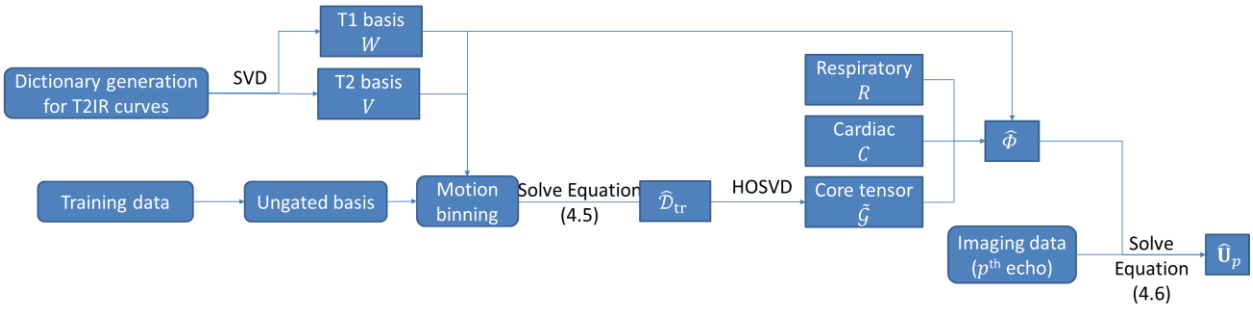

Figure 4.3: Flow chart for image reconstruction.

4.2.1.4 Parameter quantification

All quantification processes are performed at the end-expiration and end-diastolic phases of the reconstructed images.

The signal equation was derived based on the sequence structure and Bloch equations, as detailed in Supporting information of the publication (158). T_1 and T_2 values are fitted voxel-by-voxel from the signal equation, using the *lsqnonlin* solver in MATLAB R2016b.

T_2* mapping and water-fat separation are performed jointly using the reconstructed multi-echo images of the last inversion time with the longest T_2IR preparation duration, which are closest to the GRE steady state. Specifically, the following equation is solved for each multi-echo image $y(\mathbf{r}, T_{\mathrm{E}})$:

$$y(\mathbf{r}, T_{\mathrm{E}}) = \left(\mathcal{W}(\mathbf{r}) + \sum\nolimits_l C_l \mathcal{F}(\mathbf{r}) e^{i2\pi f_l T_{\mathrm{E}}}\right) e^{if_{B0} T_{\mathrm{E}} - T_{\mathrm{E}}/T_2^*}, \tag{4.7}$$

using a graph-cut algorithm (153), where $\mathcal{W}(\mathbf{r})$ and $\mathcal{F}(\mathbf{r})$ are the water and fat components, C_l and f_l are the weightings and the resonance frequency offsets of the lth fat peak, f_{B0} (in Hz) is the local frequency shift due to static field inhomogeneity. A multi-peak fat spectrum is employed here according to previous work (159). Finally, FF in each voxel is calculated as (160):

$$FF(\mathbf{r}) = \begin{cases} \dfrac{|\mathcal{F}(\mathbf{r})|}{|\mathcal{F}(\mathbf{r}) + \mathcal{W}(\mathbf{r})|}, & \text{if } \mathcal{F}(\mathbf{r}) > \mathcal{W}(\mathbf{r}) \\ 1 - \dfrac{|\mathcal{W}(\mathbf{r})|}{|\mathcal{F}(\mathbf{r}) + \mathcal{W}(\mathbf{r})|}, & \text{otherwise} \end{cases}. \quad (4.8)$$

4.2.2 Data acquisition

4.2.2.1 VTR Multitasking imaging parameters

VTR Multitasking acquisition cycled through hybrid T_2IR modules with preparation times τ = 0, 30, 40, 50, 60 ms. Eleven echo times at T_E = 1.6 – 14.6 ms were collected for imaging data and a single echo at T_E = 1.6 ms was collected for training data. The scan time for VTR Multitasking was 2.5 min/slice. Scan parameters were: field of view (FOV) = 270 × 270 mm^2, in-plane resolution = 1.7 x 1.7 mm^2, slice thickness = 8.0 mm. More details of the imaging protocol are available in Table 4.1.

Table 4.1: VTR Multitasking T_1/T_2/T_2*/FF mapping protocol. Recovery period refers to the spacing between preparation pulses. BW: bandwidth.

FOV (mm)	270	**Phase FOV**	100%
Scanning matrix	160 x 160	**Slice thickness (mm)**	8.0
Resolution (mm^2)	1.7 x 1.7	**Number of readout modules per shot**	288
Recovery period (ms)	2900	**Echo time (ms)**	1.6 – 14.6 (11 echoes)
Imaging data T_R (ms)	16.6	**Training data T_R (ms)**	3.6
T_2IR prep duration (ms)	0, 30, 40, 50, 60	**Pixel BW (Hz/pixel)**	1008
Flip angle (^{0})	5	**Scan time per slice (min:sec)**	2:31

Acquisition	2D single slice	**Sampling trajectory**	Golden Angle Radial
Reconstruction time (h)	3.5		

4.2.2.2 Phantom study

An ISMRM/NIST phantom (model 130, High Prevision Devices, Boulder, Colorado USA) was scanned for validation of T_1 and T_2. A Calimetrix phantom (Calimetrix, Madison, WI) was scanned for validating T_2*. To validate FF, a separate phantom was constructed with ten vials with target fat concentrations 0%, 1%, 3%, 5%, 7%, 9%, 10%, 15%, 20%, 30%, surrounded by de-ionized water.

Inversion-recovery spin echo (IR-SE) and T_2-weighted spin echo (T_2-SE) were acquired as references for T_1 and T_2, respectively. For the T_2* reference, single-echo GRE images were acquired for ten different echo times between 1 ms and 25 ms. A product q-DIXON sequence with 6 bipolar readouts was used as a reference for FF. Imaging parameters for all reference sequences are summarized in Table 4.2.

The above phantoms were put onto a linear motion stage (SHELLEY, Toronto, Ontario CANADA) to test the performance of the proposed VTR Multitasking technique to translational motion (period = 3.5 s, similar to respiratory motion). CTR Multitasking was also scanned for comparison. The phantom and the motion stage were placed as illustrated in Figure 4.4 to generate both in-plane and through-plane motion.

Table 4.2: List of sequence parameters for phantom study.

	VTR Multitasking	CTR Multitasking	IR-SE	T_2-SE	Multiple GRE	Q-dixon
Purpose	$T_1/T_2/T_2$*/FF		T_1	T_2	T_2*	FF
FOV (mm)	270 x 270					
Matrix size	160 x 160		192 x 192		160 x 160	128 x 128

In-plane resolution (mm)	1.7 x 1.7		1.4 x 1.4		1.7 x 1.7	2.1 x 2.1
Inversion time (ms)	3.6, 20.2, 23.8, 40.4, 44.0, …, 2892.2, 2908.8	16.6, 33.2, 49.8, 66.4, 83.0, …, 2905.0, 2921.6	50, 210, 350, 500, 1000, 1500, 2400, 3000	/	/	/
TE (ms)	1.6, 2.9, 4.2, 5.5, 6.8, 8.1, 9.5, 10.7, 12.0, 13.3, 14.6		8	15, 25, 45, 70, 100, 140, 180	1.6, 2.6, 3.6, 5.6, 7.6, 10.6, 13.6, 16.6, 20.6, 25.0	1.1, 2.5, 3.7, 4.9, 6.2, 7.4
TR (ms)	3.6 (Training data) 16.6 (Imaging data)	16.6	5000			9
Flip angle (°)	5		90	90	20	4
Scan time	2.5 min		1.88 h	1.88 h	2.24 h	13 s

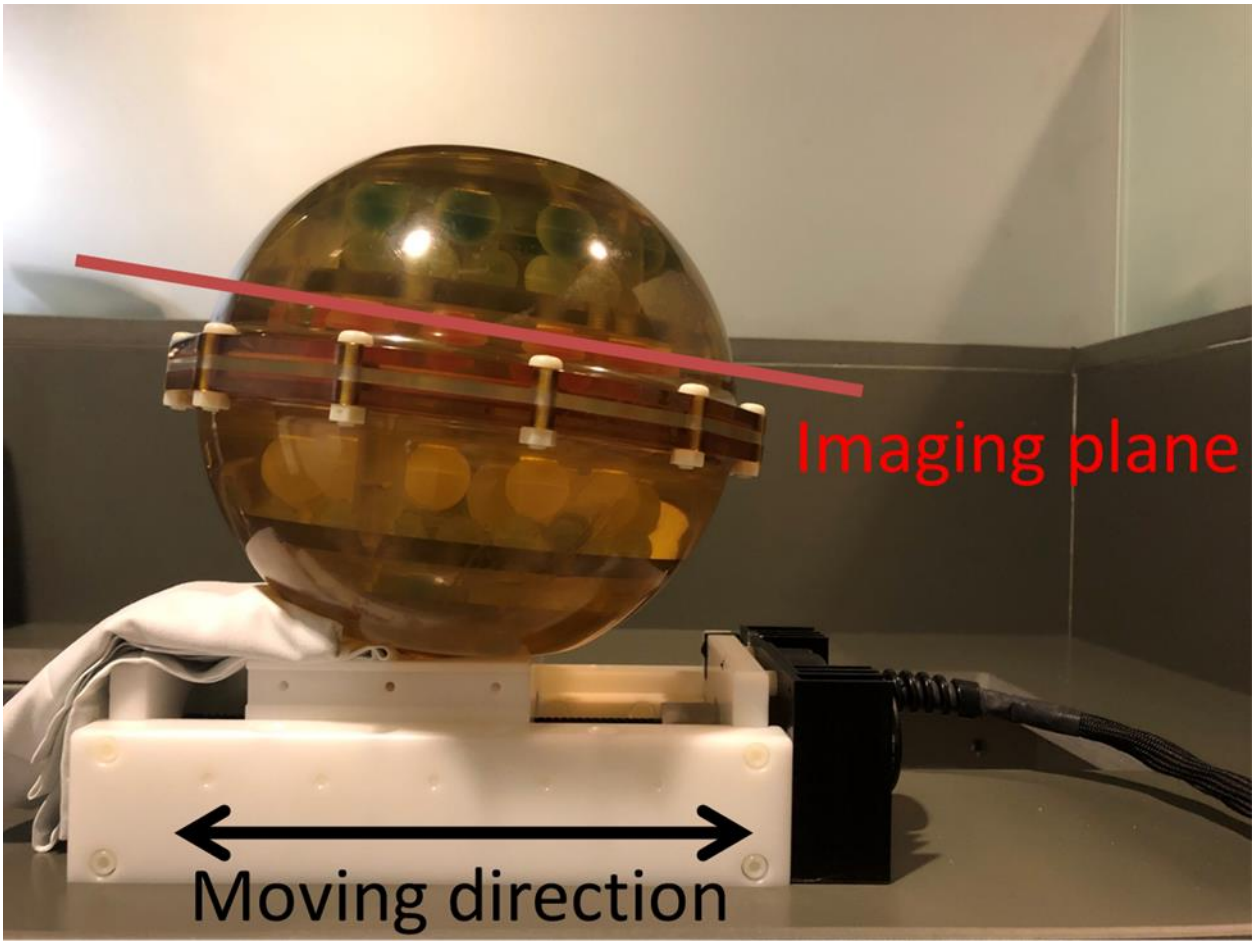

Figure 4.4: Illustration of motion stage and phantom setup. The phantom was titled towards the vertical line so that the moving direction of the stage would not be parallel to the imaging plane and spheres will experience both in-plane and through-plane motion.

4.2.2.3 In-vivo study

The in vivo study was approved by the institutional review board at Cedars-Sinai Medical Center and at VA Greater Los Angeles Healthcare System. Written informed consent from all subjects was obtained before the study. N = 12 healthy volunteers (age: 38.2 ± 13.1, 4 male) were recruited and scanned on a 3T scanner (MAGNETOM Vida, Siemens Healthineers, Erlangen, Germany) with a standard 18-channel body coil and an integrated spine matrix coil. VTR Multitasking acquisition was performed in short-axis views (basal, mid-ventricular, and apical slices). Reference protocols were scanned in the same imaging slices with an end-expiration

breath-hold, and triggered to the end-diastolic cardiac phase. Reference sequences included MOLLI for T_1 mapping and T_2-prep GRE for T_2 mapping. ME-GRE with 20° flip angle and 8 echo times ranging from 1.6 – 16.3 ms was used as the T_2* reference (144, 161). A prototype 6-point Dixon GRE sequence with 5° flip angle (21, 162-164) was used as the FF reference. Detailed parameters are listed in Table 4.3. Both VTR Multitasking and references were repeated once more at the mid-ventricular slice to test scan-rescan repeatability. Parametric maps were also acquired using CTR Multitasking (with identical scan time and parameters as VTR, except that T_E = 1.6 – 14.6 ms was used for both imaging and training data) at the mid-ventricular slice for comparison against VTR Multitasking.

To further validate the proposed technique on abnormal T_2* values, the VTR Multitasking and reference T_2* mapping sequences were incorporated as part of the clinical protocol with ferumoxytol (Feraheme, Covis Pharma, Cary, NC, USA) enhancement, which mimicked increased myocardial iron content. 3 patients (age: 70.7 ± 15.5, 2 male) with known ischemic heart diseases were scanned on a 3T scanner (MAGNETOM Skyra, Siemens Healthineers, Erlangen, Germany) with a standard 18-channel body coil and an integrated spine matrix coil. The images were acquired in the mid-ventricular slice at baseline, and following a 12-min intravenous infusion of ferumoxytol (4.0 mg/kg). MOLLI images were acquired as the conventional reference for T_1 mapping.

The proposed technique was also scanned within a protocol for PASC patients (N=13, age: 52.1 ± 14.5, 7 male) on a 3T scanner (MAGNETOM Vida, Siemens Healthineers, Erlangen, Germany) with a standard 18-channel body coil and an integrated spine matrix coil. The images were acquired in the mid-ventricular slice. MOLLI and T_2-prep GRE were used as T_1 and T_2 mapping references, respectively.

Table 4.3: List of sequence parameters for in-vivo study. Phase oversampling will be used for reference sequences to avoid wrapping when necessary. Nominal scan time of reference sequences is calculated for heart rate of 60 bpm. Here the temporal resolution for Multitasking is defined as the period between training data acquisitions.

	VTR Multitasking	CTR Multitasking	MOLLI 5(3)3	T_2 prep-FLASH	Multi-echo GRE	6-point Dixon GRE
Purpose	$T_1/T_2/T_2$*/FF		T_1	T_2	T_2*	FF
FOV (mm)	270 x 270					
Matrix size	160 x 160					
In-plane resolution (mm)	1.7 x 1.7					
Slice thickness (mm)	8					
Partial Fourier	/		6/8			
GRAPPA	/		R = 2			
Inversion time (ms)	3.6, 20.2, 23.8, 40.4, 44.0, …, 2892.2, 2908.8	16.6, 33.2, 49.8, 66.4, 83.0, …, 2905.0, 2921.6	100, 180, 947, 1045, 1807, 1892, 2695, 3615	/	/	/
TE (ms)	1.6, 2.9, 4.2, 5.5, 6.8, 8.1, 9.5, 10.7, 12.0, 13.3, 14.6		1.04	1.29	1.6, 3.7, 5.8, 7.9, 10.0, 12.1, 14.2, 16.3	1.6, 2.8, 4.1, 5.4, 6.6, 7.9
Readout mode	bipolar		/	/	monopolar	bipolar
TR (ms)	3.6 (Training data) 16.6 (Imaging data)	16.6	2.51	3.09	18.2	9.8
Temporal resolution (ms)	20.2	33.2	283.8	254.2	109.1	129.5
Flip angle (°)	5		35	12	20	5
Scan time	2.5 min		11 s	9 s	10 s	10 s

The reference T_1, T_2, and T_2* maps were automatically generated by the scanner. The reference FF maps were computed from complex images as described in Methods Section 4.2.1.4.

4.2.3 Analysis

All reconstructions were performed using MATLAB 2016b (MathWorks, Natick, Massachusetts) on a Linux workstation with a 3.08-GHz dual 16-core Intel Xeon processor and 256 GB RAM, which took about 3.5 hours for each slice. The rank for the T_1 dimension was chosen as 5 from the -40 dB threshold on the normalized singular value curves of the simulated dictionary. The ranks for T_2, respiratory motion, and cardiac motion dimensions were not truncated, as the nuclear norm term in Equation (5) for training tensor completion already performed a soft constraint on the tensor ranks of those dimensions. Finally, the rank for spatial dimension was empirically set to 48.

For phantom study, T_1/T_2/T_2*/FF measurements were calculated for each vial. Linear regression was performed for the relevant range (T_1: 0-2000 ms, T_2, T_2*: 0-100 ms, FF: 0 – 100%) and intraclass correlation coefficients (ICCs) were calculated from a two-way mixed model and 95% confidence using IBM SPSS Statistics (Armonk, New York) to evaluate the agreement between VTR Multitasking and the references.

A correlation analysis was performed between VTR Multitasking measurements of the motion phantom and the static reference values, between moving and static VTR Multitasking measurements, and between moving CTR and VTR Multitasking measurements. ICCs were calculated to assess agreement. SNR in each vial (defined as mean value over standard deviation) was calculated and compared between VTR and CTR measurements with Wilcoxon signed rank test.

The in vivo mid-ventricular maps of healthy subjects from different methods (references, VTR Multitasking, and CTR Multitasking) were blinded and pooled and assessed by an imaging cardiologist (A.C.K.). The T_1 and T_2 maps were scored based on a 4-point grading system (21): 1, uninterpretable; 2, poor (blurring and residual artifacts); 3, acceptable (mildly blurring and mild residual artifacts); 4 excellent (sharp myocardium wall and no artifact). The T_2* maps were scored based on a 5-point grading system (165): 0, unusable; 1, poor (heart just visible); 2, average (with severe septal artifact) 3, good (with moderate septal artifact); 4, very good (with mild septal artifact); 5, excellent (with negligible septal artifact). FF maps were not scored due to a lack of expertise (FF quantification is not clinically performed yet). The scores from the proposed VTR Multitasking were compared to those from reference and CTR Multitasking method using Wilcoxon signed-rank test.

The in vivo reference and VTR Multitasking maps were segmented in CVI 42 (Circle Cardiovascular imaging, Calgary, Alberta, Canada) using the AHA 16-segment model (166). Specifically, the epi- and endo-cardial contours were drawn on VTR Multitasking T_1 maps and were copied to other VTR Multitasking maps, which are co-registered. For reference T_1 and T_2 maps, the contours were drawn separately on the maps. For reference T_2* and FF maps, the ROIs were traced separately on the raw images (6) and were copied to the maps. Finally, automatic segmentation was performed by the software using the contours.

The T_1, T_2, T_2*, and FF values in different myocardial segments were used for comparison between VTR Multitasking and references. Myocardial homogeneity in healthy subjects was assessed using the root-mean square (RMS) inter-segment standard deviation (ISSD), which was calculated as the standard deviation of the 16 segmental values for each subject, aggregated across subjects using RMS. Repeatability in healthy subjects was assessed using the RMS within-segment

standard deviation (WSSD), which was calculated as the standard deviation of the 2 test–retest values for each segment and aggregated across segments and subjects using RMS, and coefficient of variation (CoV), which was calculated by normalizing the RMS-WSSD with the mean value of the 6 mid-ventricular segments. Three-way ANOVA tests (with methods, subject groups, pre- or post-contrast as independent variables) were performed on the mean T_1/T_2* measurements in each subject to test for statistically significant differences ($P<0.05$) between different methods. A two-way ANOVA test (with methods, subject groups as independent variables) was performed on the mean T_2 measurement in each subject to test for statistically significant differences ($P<0.05$) between different methods. A two-tailed student t-test was used for comparing mean FF measurements between different methods (with $P<0.05$ as significant), as these reference measurements were not available in patient groups. The agreement between different methods (in healthy subjects and in patients) and between repeated measurements (in healthy subjects) were assessed using Bland-Altman analysis.

4.3 Results

4.3.1 Phantom study

Phantom results shown in Figure 4.5A demonstrated good quality of VTR Multitasking maps both with and without motion. Substantial correlation ($R = 0.998$, 0.999, 0.979, and 0.995 for $T_1/T_2/T_2$*/FF, respectively) and agreement (ICC = 0.990, 0.959, 0.978, and 0.991 for $T_1/T_2/T_2$*/FF, respectively) were found between VTR Multitasking and reference measurements (Figure 4.5B). With motion, VTR Multitasking measurements still showed good correlation ($R =$ 0.999, 0.999, 0.986, and 0.995 for $T_1/T_2/T_2$*/FF, respectively) and agreed (ICC = 0.988, 0.934, 0.981, and 0.993 for $T_1/T_2/T_2$*/FF, respectively) with the reference measurements (Figure 4.5C). Figure 4.6 plots VTR Multitasking measurements with motion against those without motion. The

fitted slopes through regression analysis were 0.984, 0.980, 0.948, and 0.948 for $T_1/T_2/T_2^*$/FF, respectively. The correlation coefficients (R > 0.95) and ICCs (ICC > 0.96) indicated agreement.

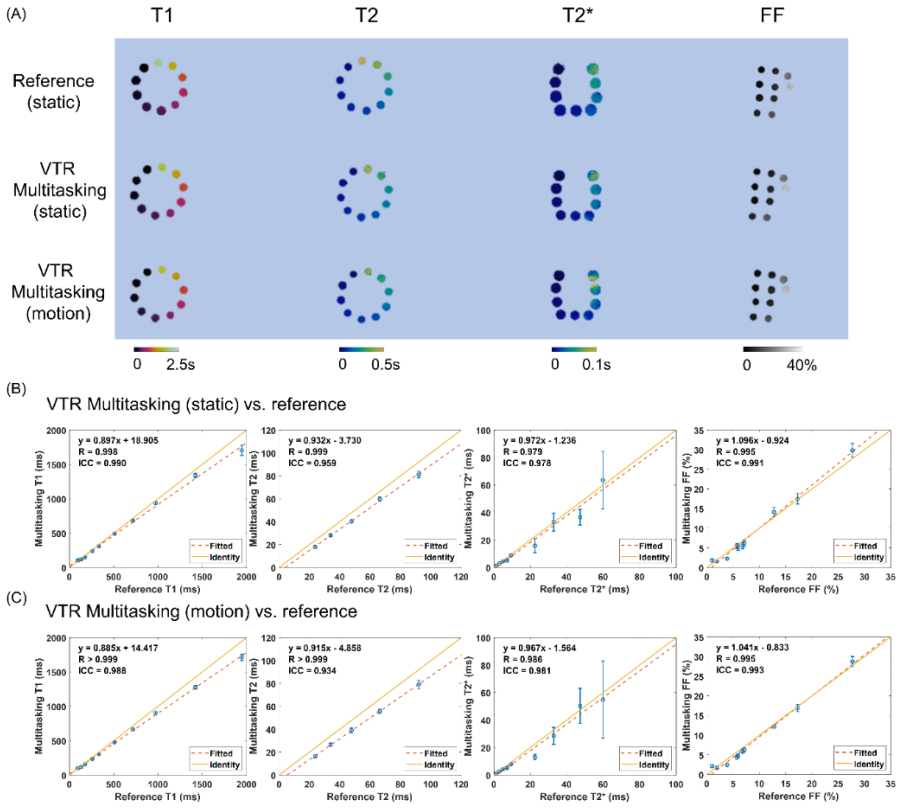

Figure 4.5: (A) Reference maps (1st row), VTR Multitasking maps collected without motion (2nd row), and VTR Multitasking maps collected with motion (3rd row) for NIST, Calimetrix, and FF phantoms. (B) The correlation plot between VTR Multitasking measurements (collected without motion) and reference measurements, with correlation coefficients and ICCs labeled (R > 0.97, ICC > 0.95). (C) The correlation plot between VTR Multitasking measurements (collected with motion) and reference measurements, with correlation coefficients and ICCs labeled (R > 0.98, ICC > 0.93).

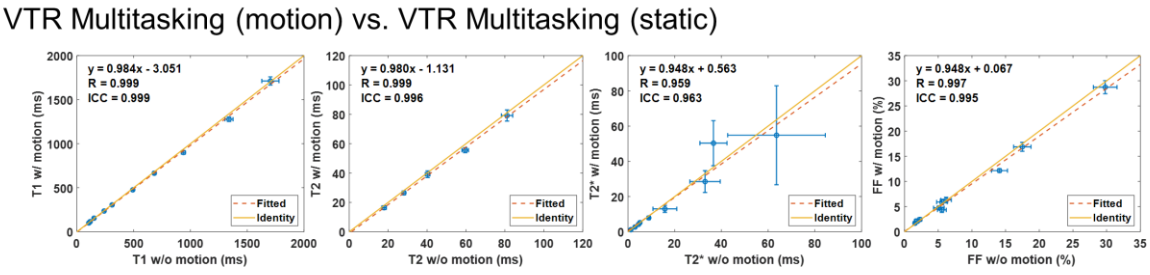

Figure 4.6: The correlation plot between Multitasking measurements with and without motion, with correlation coefficients and ICCs labeled (R > 0.95, ICC > 0.96).

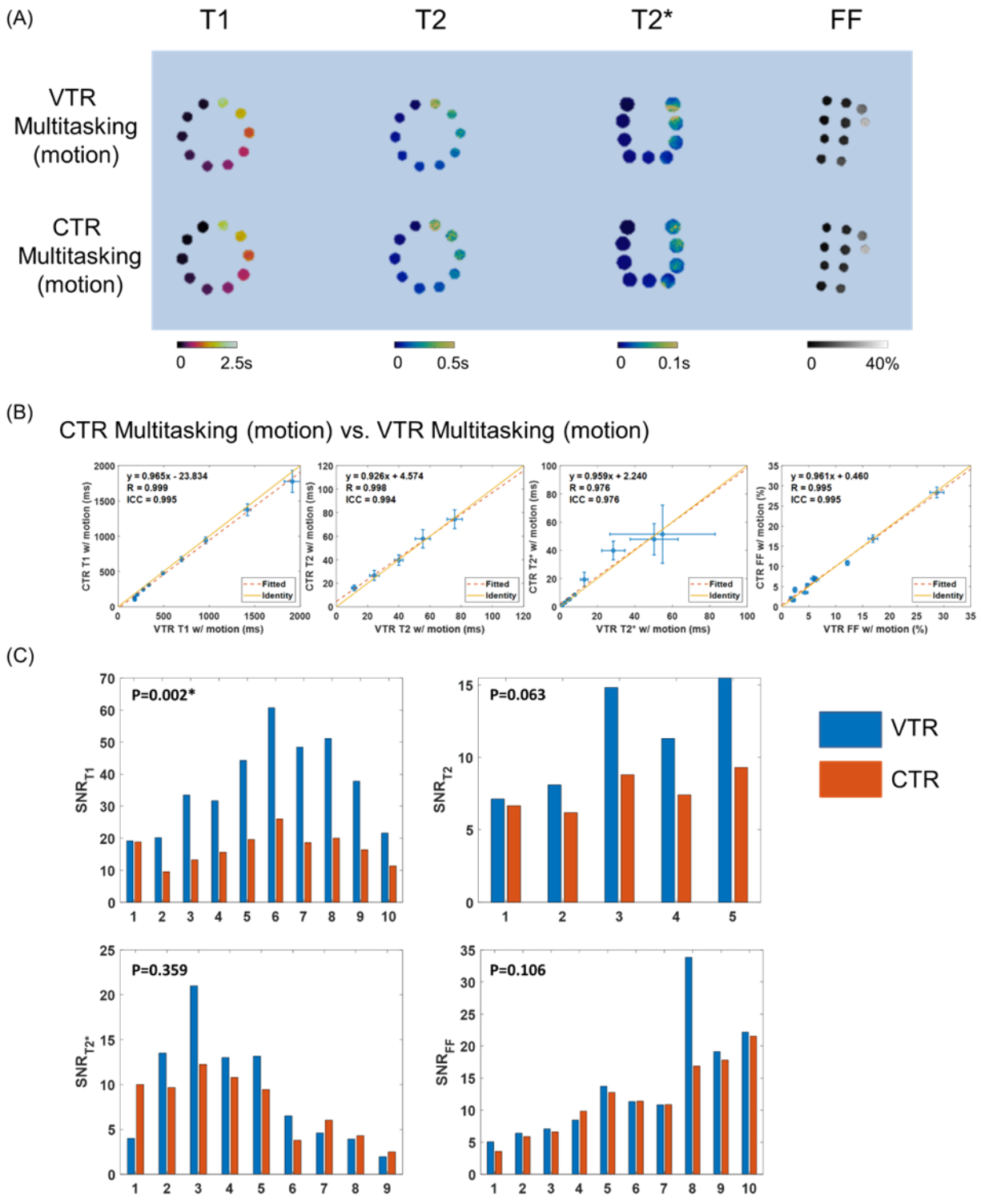

Figure 4.7: Comparison of VTR and CTR Multitasking measurements in motion phantoms. Differences with statistical significance (P<0.05) are identified by *.

The comparison between VTR and CTR Multitasking on motion phantoms is shown in Figure 4.7. The maps resembled each other, and the fitted slopes were 0.965, 0.926, 0.959, and 0.961 for T_1/T_2/T_2*/FF, respectively. Their measurements were consistent, as indicated by R and ICC (R > 0.97, ICC > 0.97). The SNR comparison in each vial demonstrated significantly better T_1 precision with the VTR approach (P =0.002). No significant difference was found for other parameters (P = 0.063, 0.359, and 0.106 for /T_2/T_2*/FF, respectively).

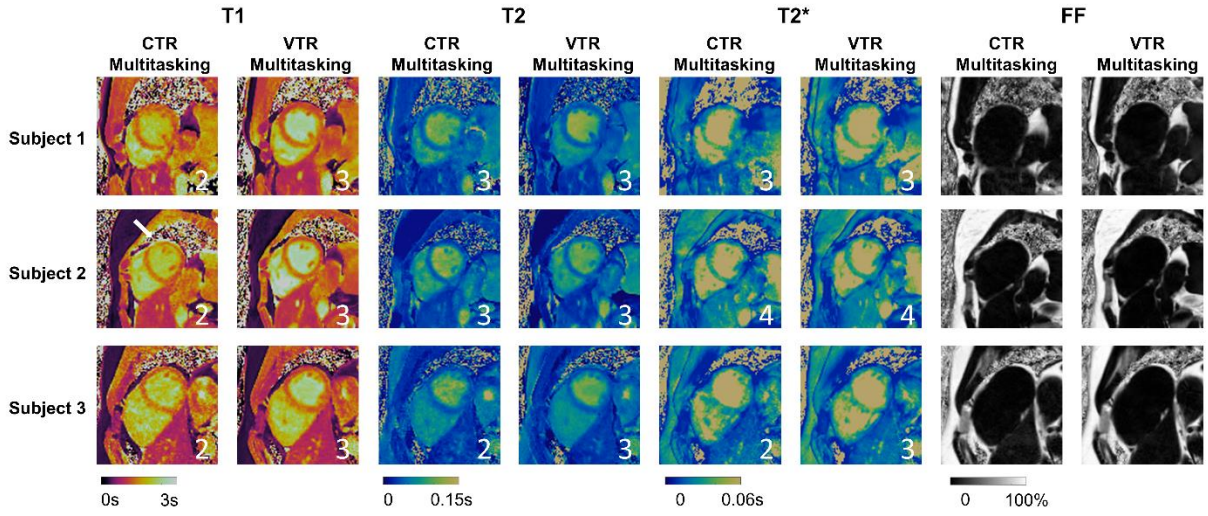

Figure 4.8: Comparison of T_1, T_2, T_2*, and FF maps between VTR Multitasking and CTR Multitasking method on three representative healthy subjects. The image quality scores from the cardiologist were labelled at the bottom-right corner of corresponding maps.

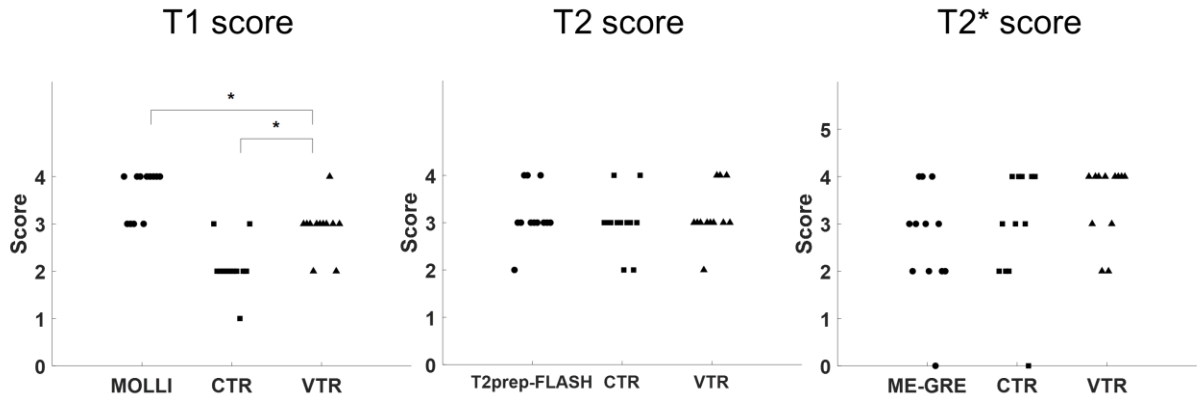

Figure 4.9: Evaluation of T_1, T_2, T_2* map quality from reference, CTR, and VTR Multitasking techniques. Differences with statistical significance (P<0.05) are identified by *.

4.3.2 In-vivo study

Figure 4.8 compares VTR and CTR Multitasking maps of 3 healthy subjects. Improved SNR and image quality are apparent on the VTR T_1 and T_2 maps. The white arrow on the CTR T_1 map indicates myocardial artifacts produced by CTR Multitasking. T_2* and FF maps from both methods appeared similar. The image quality scores for VTR and CTR Multitasking are shown in Figure 4.9, which indicated significantly higher scores for VTR T_1 maps (VTR median score: 3, CTR median score: 2, P =0.008). No significant differences were found in scores of T_2 (both with median score: 3, P = 0.766) and T_2* maps (VTR median score: 4, CTR median score: 3, P = 0.371).

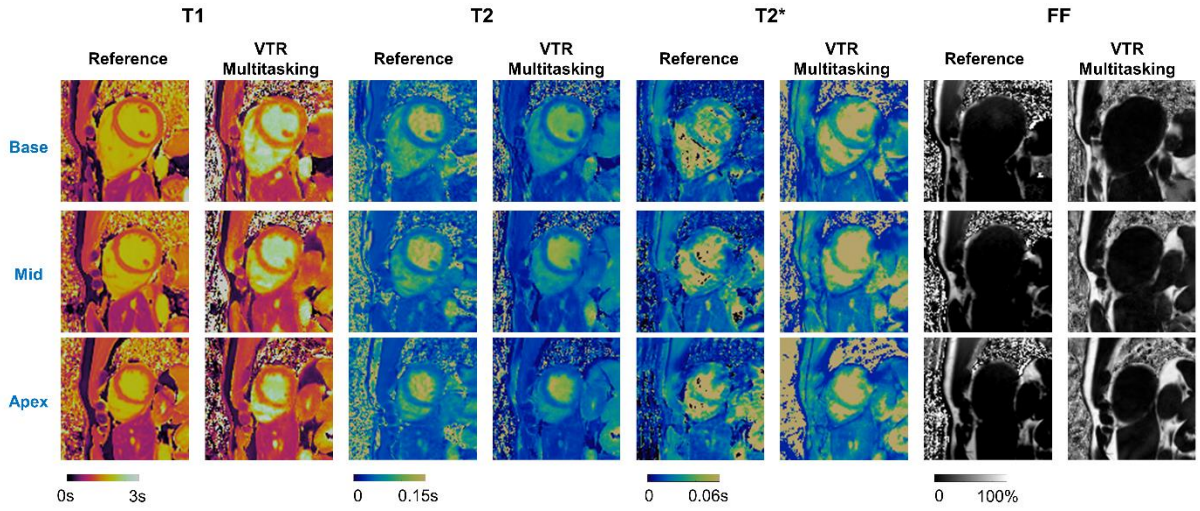

Figure 4.10: T_1, T_2, T_2*, and FF maps from VTR Multitasking and references on a representative healthy subject. The image quality scores for the mid-ventricular slice were: reference T_1 - 4 (excellent); reference T_2 - 3 (acceptable); reference T_2* - 3 (good); VTR Multitasking T_1 - 3 (acceptable); VTR Multitasking T_2 - 3 (acceptable); VTR Multitasking T_2* - 3 (good).

Mapping results from a representative healthy subject are shown in Figure 4.10 for VTR Multitasking and references. VTR Multitasking produced co-registered maps that resembled reference maps. The image quality scores in Figure 4.9 indicated significantly lower T_1 scores of VTR Multitasking compared to those of MOLLI (VTR median score: 3, MOLLI median score: 4,

P = 0.008). No significant differences were found for T_2 (both with median score: 3, P = 1.000) and T_2* maps (VTR median score: 4, reference median score: 3, P = 0.125). AHA 16-segment bullseye plots in Figure 4.11 show the mean quantitative measures across all 12 healthy subjects for T_1, T_2, T_2*, and FF. Both methods demonstrated little spatial variability in T_1 (RMS-ISSD < 80ms) and T_2 maps (RMS-ISSD < 4 ms). Higher spatial variability relative to the mean was found on T_2* maps of both methods, both of which measured lower T_2* values in the infero-lateral segment. VTR Multitasking FF maps showed better spatial homogeneity than reference maps (2.7% vs. 5.2%) and both methods indicated little-to-no myocardial fat in healthy subjects.

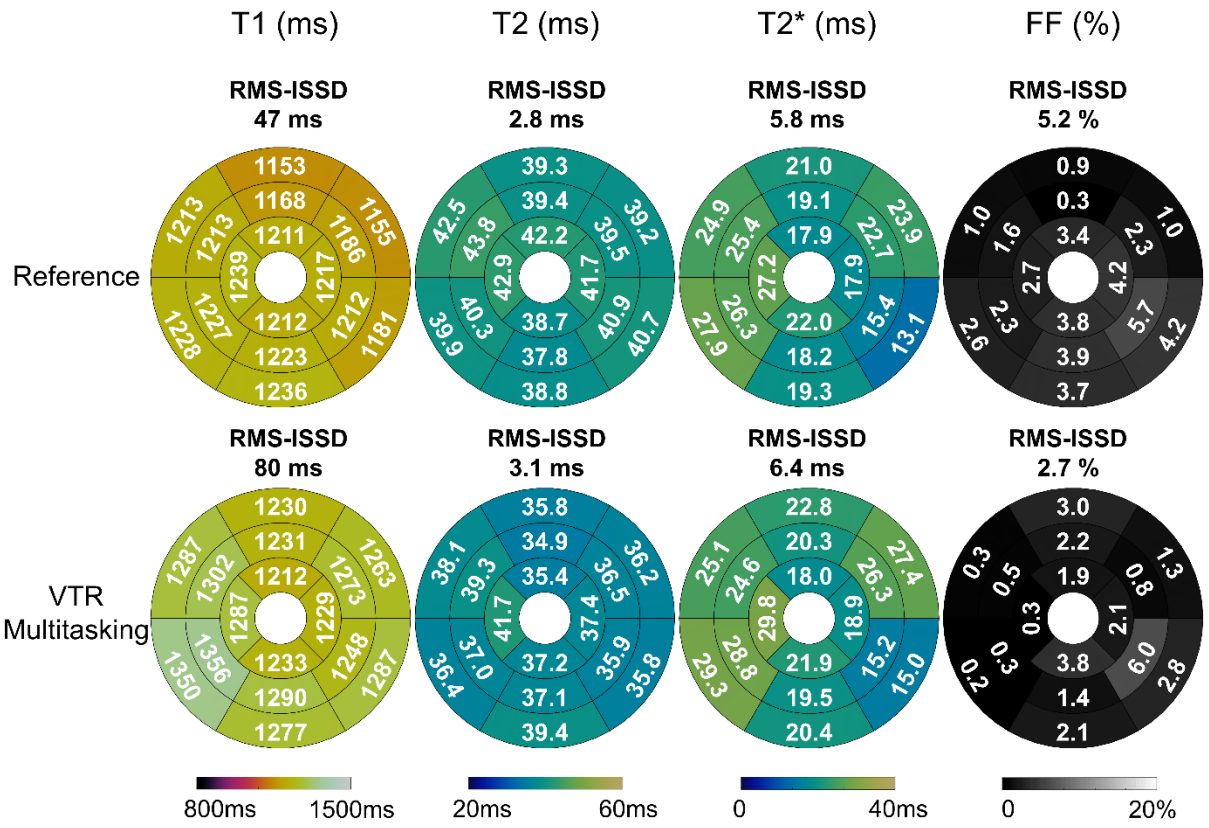

Figure 4.11: Bullseye plot of average T_1, T_2, T_2*, and FF measurements in healthy subjects (N=12) acquired with VTR Multitasking and references, with RMS-ISSD labelled to indicate the spatial variability.

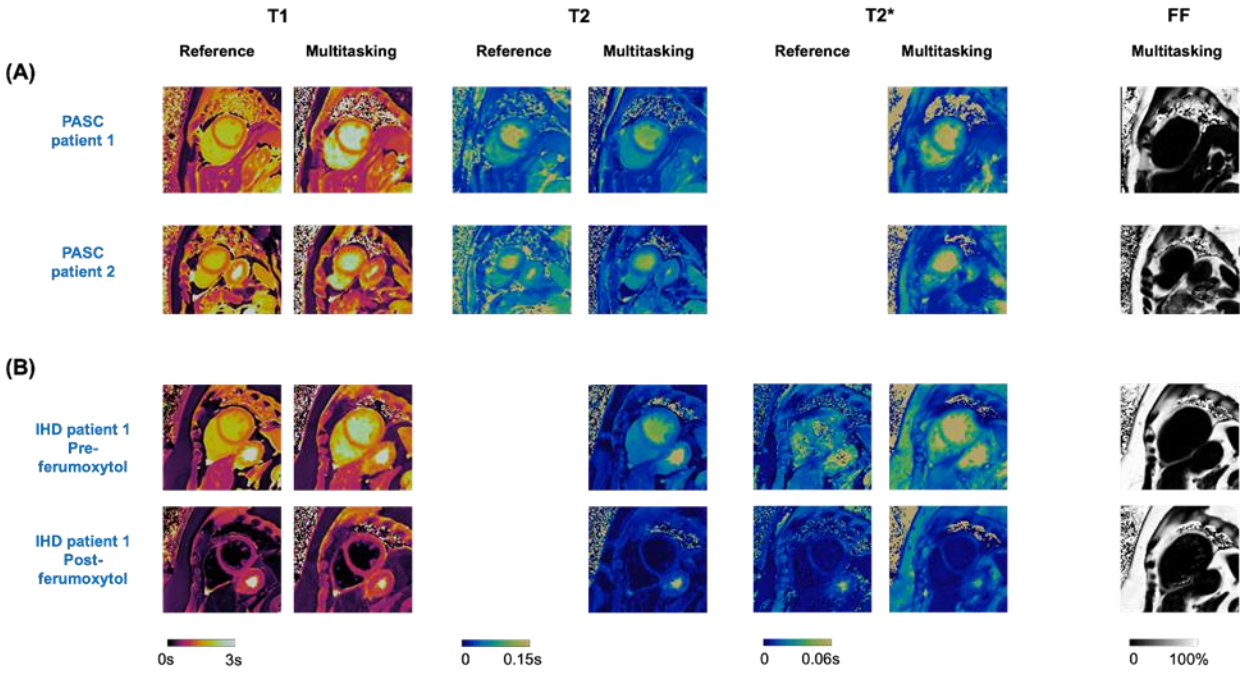

Figure 4.12: VTR Multitasking maps and available reference maps on two PASC patients (A) and an IHD patient pre- and post-ferumoxytol administration (B).

VTR Multitasking maps and available reference maps for two PASC patients are shown in Figure 4.12A. The quantitative maps pre- and post-ferumoxytol enhancement for an IHD patient are shown in Figure 4.12B. Both Multitasking and reference T_2* map showed reduced T_2* after ferumoxytol administration.

T_1, T_2, T_2*, and FF measurements from VTR Multitasking and available references are shown in Table 4.4 for all subjects. Statistical analysis indicated small but significant differences between VTR Multitasking and references for T_1 ($P < 0.001$, three-way ANOVA) and T_2 ($P<0.001$, two-way ANOVA). No significant differences were found between VTR Multitasking and references for T_2* ($P=0.820$, 3-way ANOVA) and FF measurements ($P=0.307$, t-test). Bland-Altman analyses in the global myocardium and in all segments are shown in Figure 4.13, with the following limits of agreement and CoV: global T_1: ±93 ms (4.0%); global T_2: ±10 ms (6.8%), global T_2*: ±4 ms

(6.7%), global FF: ±7% (>100%); segment-wise T_1: ±176 ms (6.2%), segment-wise T_2: ±9 ms (10.0%), segment-wise T_2*: ±11 ms (19.6%), segment-wise FF: ±12% (>100%).

Table 4.4: VTR Multitasking and reference measurements for all subjects.

		Reference	VTR Multitasking
Healthy volunteers (N=12)	T_1 (ms)	1207.8 ± 41.8	1266.8 ± 65.8
	T_2 (ms)	40.5 ± 1.4	37.4 ± 2.3
	T_2* (ms)	21.9 ± 2.9	23.2 ± 2.2
	FF (%)	2.7 ± 3.5	1.6 ± 1.0
PASC patients (N=13)	T_1 (ms)	1251.9 ± 26.9	1315.0 ± 71.0
	T_2 (ms)	41.0 ± 2.7	36.8 ± 3.5
IHD patients (pre-contrast, N=3)	T_1 (ms)	1266.6 ± 10.6	1316.1 ± 8.3
	T_2* (ms)	20.5 ± 4.7	22.1 ± 3.8
IHD patients (post-contrast, N=3)	T_1 (ms)	752.5 ± 71.2	866.0 ± 39.8
	T_2* (ms)	8.2 ± 1.1	6.8 ± 0.3

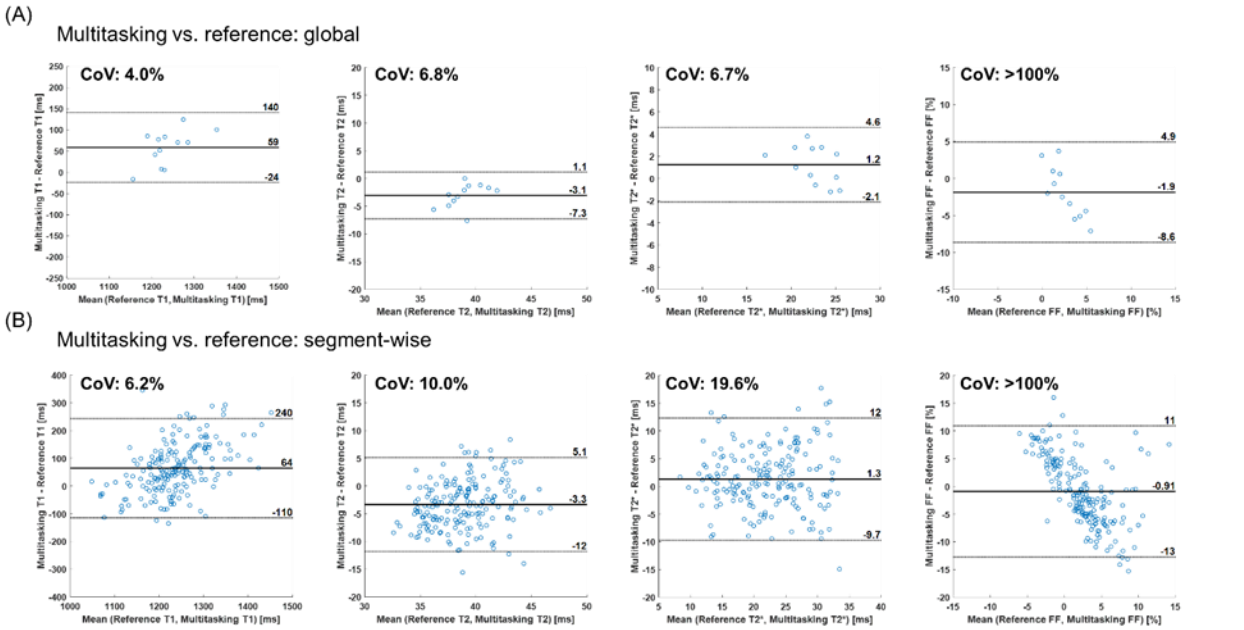

Figure 4.13: Bland-Altman plots comparing T_1, T_2, T_2*, and FF measurements from references and Multitasking techniques in global myocardium (A) and in all myocardial segments (B) of the healthy subjects. The dotted lines indicate the 95% limits of agreement, and the solid lines indicate mean bias. CoV: coefficient of variation.

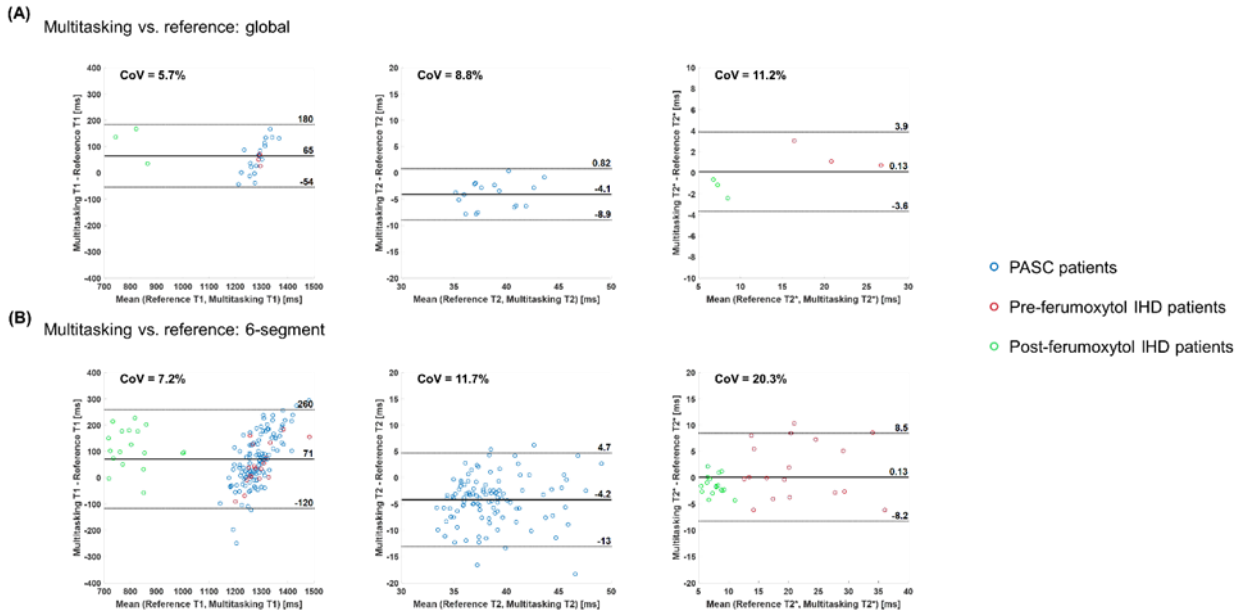

Figure 4.14: Bland-Altman plots comparing T_1, T_2, T_2* measurements from references and Multitasking techniques in global myocardium (A) and in mid-ventricular myocardial segments (B) of the patients. The dotted lines indicate the 95% limits of agreement, and the solid lines indicate mean bias. CoV: coefficient of variation.

The agreement between Multitasking and reference measurements were also analyzed for the patient cohort using Bland-Altman plots, as shown in Figure 4.14 for the global myocardium and all mid-ventricular segments. The following limits of agreement and coefficients of variation were found: global T_1: ±124 ms (6.1%); global T_2: ±5 ms (8.8%), and global T_2*: ±4 ms (11.2%); segmental T_1: ±198 ms (7.7%), segmental T_2: ±9 ms (11.4%), and segmental T_2*: ±8 ms (20.3%). Compared to the results on healthy volunteers, the limits of agreement in patients were larger.

Figure 4.15 shows repeatability measurements from VTR Multitasking and references in healthy subjects for the mid-ventricular slice. Figure 4.16 shows Bland-Altman plots of VTR Multitasking repeated measurements in the global region and in the 6 mid-ventricular segments of the healthy subjects. The limits of agreement between first and second VTR Multitasking scan were: global T_1: ±76 ms, global T_2: ±3 ms, global T_2*: ±7 ms, global FF: ±1%; segment-wise T_1: ±181 ms, segment-wise T_2: ±7 ms, segment-wise T_2*: ±9 ms, segment-wise FF: ±3%). Both VTR

Multitasking and references demonstrated good repeatability, as indicated by RMS-WSSD (T_1: < 65 ms, T_2: < 3 ms, T_2*: < 4 ms, FF: < 2 %) and CoV (T_1: < 6%, T_2: < 7%, T_2*: < 15%, FF: < 77%).

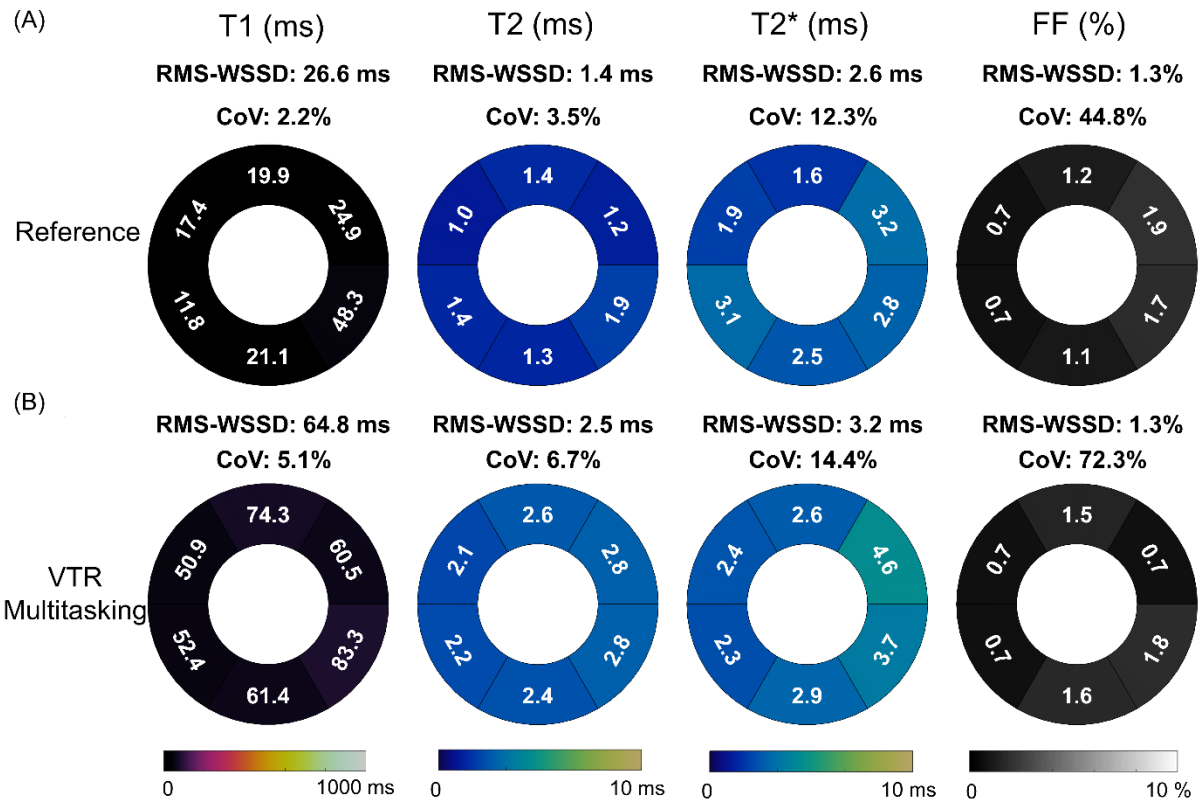

Figure 4.15: Reference (A) and Multitasking (B) measurement repeatability. Both methods demonstrated good repeatability, as indicated by RMS-WSSD and CoV.

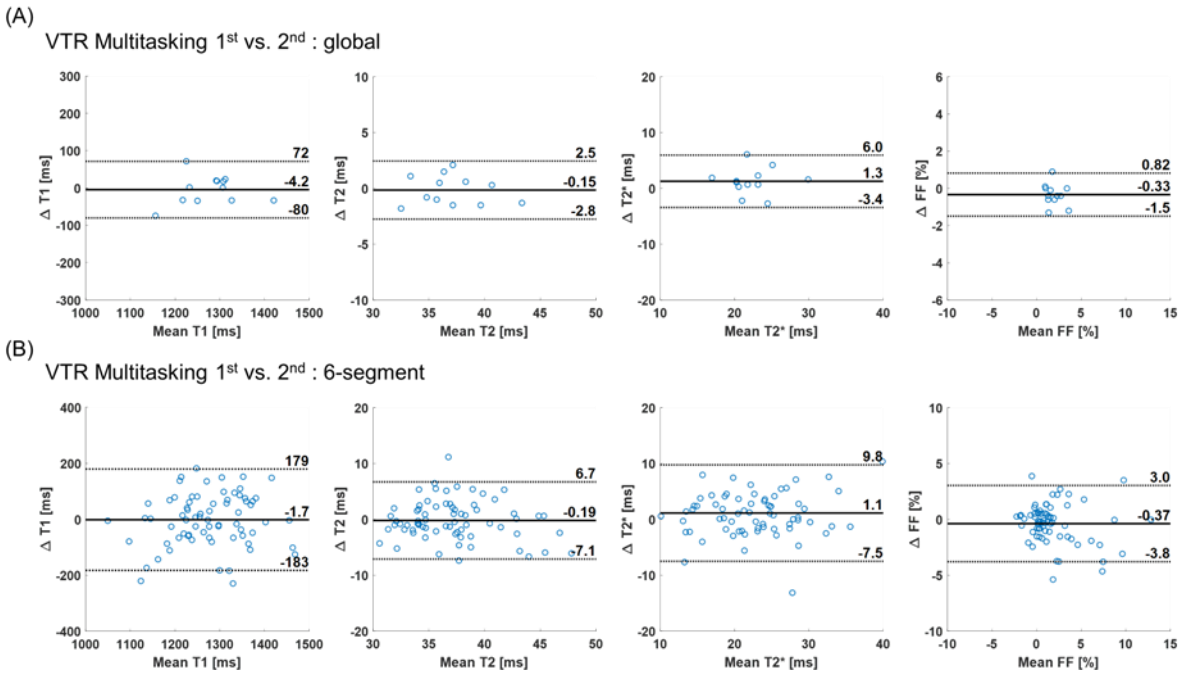

Figure 4.16: Bland-Altman plots comparing T_1, T_2, T_2*, and FF measurements from 1st and 2nd Multitasking scan in global myocardium (A) and in all 6 mid-ventricular segments (B) of N=12 healthy volunteers. The dotted lines indicate the 95% limits of agreement, and the solid lines indicate mean bias.

4.4 Discussion

Conventional single parametric cardiac mapping requires multiple breath-hold scans (141-143), leading to long scan times, potential image misregistration, and patient fatigue. Advanced techniques including 2D T_1/T_2/FF mapping (21) and T_1/T_2/T_2*/FF mapping (167) with a single breath-hold and free-breathing multi-parametric mapping techniques such as 3D T_1/T_2 mapping (146) and 2D T_1/T_2/T_2* mapping (144) have been developed. However, ECG signal is still required to deal with cardiac motion, which is prone to noise and errors particularly at high field strengths (57) and may fail in arrhythmia patients. In fact, a previous study (168) at 3T showed that ECG triggering failed for up to 35% of patients with regular sinus rhythm. In this work, a free-breathing, non-ECG technique was developed for simultaneous and co-registered myocardial T_1, T_2, T_2*, and FF quantification based on the MR Multitasking framework. The technique was validated on static

and motion phantoms, healthy volunteers, and patients, and the results indicated that the technique could provide repeatable measurements that agreed with the references.

CTR Multitasking using multi-echo readouts and a constant T_R for both training and imaging data has been recently presented for T_2* mapping in the brain (151) and T_2*/FF mapping in the liver (152). The VTR approach proposed in this work clearly outperformed the CTR approach in motion phantoms and in the heart, as shown in Figure 4.7 - Figure 4.9. Potential reasons include: (a) VTR collects more imaging data than CTR per unit scan time, resulting in improved imaging efficiency. (b) VTR has a higher temporal resolution (i.e., frequency of training data collection). With a T_R of 16 ms, the temporal resolution of the CTR approach will be at least 32 ms, thus making it more challenging to perform cardiac motion binning. In contrast, the temporal resolution of VTR in this work improved to 20 ms.

The VTR Multitasking measurements in phantoms were in good agreement with the SE and GRE references, yet T_1 and T_2 underestimation was observed. One possible cause of T_1 underestimation could be magnetization transfer effect (169). T_2 underestimation could potentially be caused by the sensitivity of the VTR Multitasking preparation scheme (T_2IR) to B_1 inhomogeneity (120). The VTR Multitasking measurements in moving phantoms showed similar results, which demonstrated the robustness of our technique to in-plane and through-plane motion. There were differences between the VTR Multitasking T_2* measurements with and without motion (especially the penultimate vial), which could be related to B_0 field changes during phantom movement.

The in vivo VTR Multitasking maps showed good spatial homogeneity, especially in T_1 and T_2. Both VTR Multitasking and reference methods revealed relatively low T_2* values in the infero-lateral segment, resulting in higher relative spatial variability in T_2* maps. Both techniques also

showed lower T_2* repeatability around the lateral wall than in other segments. This may be related to susceptibility artifacts around tissue boundaries, leading to less reliable T_2* measurement for both the Multitasking and reference techniques (170, 171). This has been a common issue for T_2* mapping especially at high fields, and our technique performed similarly to the conventional ones in this aspect.

In addition to the T_2 differences between VTR Multitasking and references as in the phantom study, the statistical test also showed a small but significant difference in T_1 measurements. One possible explanation would be T_1 underestimation from MOLLI due to magnetization transfer, T_2 confounding factors, and dependence on heart rate (169). The potential mismatch between cardiac phases and respiratory phases during analysis may partially contribute to these differences as well. In Multitasking, the cardiac phase with largest blood pool was selected as diastole and the respiratory phase with highest liver position was selected as end-expiration. In reference scans, however, the acquired phase may not always be diastole due to heart rate variations and breath-holding positions may vary based on given durations for exhalation. Despite the differences, VTR Multitasking measurements in healthy volunteers were still within or close to previous literature range at 3T (T_1: 1100-1314 ms, T_2: 38-46 ms, T_2*: 20.5 – 24 ms, FF: 1-1.5 %) (21, 161, 165, 172-175). The repeatability of Multitasking T_1 measurements (RMS-WSSD: 65 ms) were lower than that of MOLLI (RMS-WSSD: 27 ms), yet the variance in T_1 was still lower than the changes originating from various cardiovascular diseases (acute myocardial infarction: >128 ms, chronic myocardial infarction: 166 ms, hypertrophic cardiomyopathy: >125 ms, dilated cardiomyopathy: 169 ms, acute viral myocarditis: 154 ms, amyloidosis: >126 ms) (136, 176-182), indicating that the proposed technique has the potential for disease detection. The relatively large CoVs in FF

measurement of both reference and VTR Multitasking were caused by low FF values (close to 0) in this cohort.

T_1 image quality scores of VTR Multitasking were lower than those of MOLLI but the median score was still "acceptable". The lower image quality could potentially be explained by the balanced SSFP readouts used in MOLLI, which had higher SNR compared to the GRE readouts used in this work. The proposed VTR Multitasking technique still has unique advantages in resolving motion compared to MOLLI and may therefore benefit patients who cannot breath-hold or for whom ECG triggering fails. We also note that the proposed VTR scheme raised the median T_1 image quality from "poor" (for the previous CTR scheme) up to "acceptable", a critical improvement for clinical application.

Preliminary evaluation of T_2* mapping was performed on IHD patients after ferumoxytol administration, which mimicked increased myocardial iron content and resulted in short myocardial T_2* values. The results indicated the proposed technique has the potential to detect diffuse T_2* changes, e.g., in Thalassemia Major patients. Although T_1 and/or T_2 mapping were performed for PASC and IHD patients, the range of T_1/T_2/FF values in the in-vivo study is limited and the patient group has a relatively small size. In the future, more comprehensive patient study with a larger cohort and relevant disease models should be performed to evaluate the clinical significance of the proposed technique.

At present, standardization of multiparametric myocardial mapping is challenging due to vendor differences in acquisition protocols and post-processing workflow for quantitative cardiovascular MRI. The setup for ECG triggering (acquisition window, trigger delay, etc.) and instructions for breath holding can also vary among MR technologists. In comparison, our proposed method can potentially reduce the vendor-dependence and operator-dependence by

introducing a unified protocol and reconstruction scheme, and by removing the need for ECG and breath holding. Future multi-center and multi-vendor studies will be needed for validation. In this work, the technique was implemented and tested on a 3T scanner. In principle, it can also be extended to lower fields (1.5 T or even lower). The main technical challenge would be SNR reduction, as for any other techniques. Balanced SSFP readouts may be incorporated into Multitasking in SNR-demanding scenarios with further technical development.

Another potential area for future improvement is the scan time. Assuming a breath-hold scan plus the recovery period is approximately 1 min, the 2.5 mins needed for our technique is shorter than the 4 mins required for 4 single-parameter scans with reference methods. Nevertheless, it may still be time-consuming if a short-axis stack is desired in a clinical setting. Potential approaches for further acceleration include simultaneous multi-slice acquisition (183) and deep learning based methods such as super-resolution (184). In this study, we only analyzed parametric maps and measurements in the diastolic phase. However, the same parametric maps in systolic phase as well as cine imaging are also readily available with our technique (24). With dynamic information, one can potentially measure the changes of biomarkers throughout the cardiac cycle to reveal physiological information which is currently understudied using conventional techniques. Additionally, with the aid of deep learning reconstruction, inline reconstruction can be implemented (185). Finally, the adoption of advanced shim-RF coils may potentially reduce B_0 inhomogeneity and susceptibility artifacts in the myocardium especially at high fields (3T and above) (186).

4.5 Conclusion

A free-breathing, non-ECG technique was developed for simultaneous myocardial T_1, T_2, T_2*, and FF quantification in a single 2.5-min scan based on the MR Multitasking framework. The technique yielded repeatable measurements that agreed with references.

CHAPTER 5 Alternating Low-Rank Tensor Reconstruction for Cardiovascular MR Multitasking

5.1 Introduction

High-dimensional MRI, involving multiple temporal dimensions (≥ 2) associated with various types of motion and/or contrast changes, is an increasingly active field of research (60, 115, 187-191). This approach holds promise for comprehensively characterizing dynamic physiological phenomena and tissue properties. However, high-dimensional MRI often requires significantly prolonged acquisition time, which increases exponentially with the number of dimensions. Advanced reconstruction techniques that achieve high acceleration factors are therefore sought to maintain a clinically feasible scan time.

Several multidimensional reconstruction approaches are available to reduce scan time. Compressed sensing enhances acquisition efficiency by exploiting the sparse representations of underlying data in a transform domain (192). In the context of high-dimensional MRI, examples are the XD-GRASP (187) and XD flow techniques (188), which use temporal finite differences as sparsifying transforms for cardiac motion, respiratory motion, and/or contrast enhancement. Additionally, low-rank tensor structure can be used to model high-dimensional datasets (82, 155). These approaches leverage the correlations along and across spatial and temporal dimensions, using data-adaptive sparse domains/subspaces. In addition to using these compressed representations for image modeling, low-rank tensor image reconstruction additionally permits in-subspace storage and computation, making high-dimensional imaging computationally practical (60).

At present, several low-rank tensor reconstructions estimate temporal subspaces from a subject-specific auxiliary dataset. This subspace estimation is then followed by subspace-constrained reconstruction of spatial coefficients (60, 155, 193). This strategy is exemplified by the MR Multitasking framework for multi-dimensional imaging (60), which acquires two interleaved datasets: "training" data (also referred to as "navigator" data) are frequently collected at the k-space center (a projection line at $k_y = 0$) for temporal subspace estimation, and "imaging" data are collected with an incoherent sampling pattern, such as golden-angle radial trajectory, for recovering spatial coefficients with a fixed subspace.

However, neither the subspace estimation nor the subspace-constrained reconstruction is performed using the entire acquired dataset, potentially introducing subspace bias and compromising reconstruction performance, especially at high undersampling ratios. This is because the training data is only acquired at a subset of k-space locations, and the assumption that dominant temporal subspace in training data will be the same as that in the underlying images may be violated in the presence of noise and modeling error (194) and worsened by trajectory shape dependencies (195).

With the goal of further improving reconstruction and reducing scan time, here we describe a novel approach for low-rank tensor image reconstruction. Instead of estimating and using a fixed subspace for reconstruction, the proposed method jointly estimates the separate temporal basis functions, core tensor, and spatial coefficients from the entire acquired dataset. This method was evaluated for 2D myocardial T_1/T_2 mapping with MR Multitasking, using both numerical simulations and an in-vivo study.

5.2 Background

5.2.1 Problem formulation

Inspired by previous work on low-rank matrix imaging (194) and low-rank tensor completion (196), the underlying reconstruction problem with a Tucker low-rank model can be formulated as:

$$\widehat{\mathcal{X}} = \arg \min_{\substack{\mathcal{X} \\ rank(\mathcal{X}_{(i)}) \leq L_i, \forall i}} \|\mathbf{d} - \mathcal{A}(\mathcal{X})\|_2^2, \tag{5.1}$$

where $\mathbf{d}$ is the acquired k-space data, $\mathcal{A}(\cdot)$ is an MRI encoding operator which includes sensitivity maps, Fourier transform, and sampling masks, and $\mathcal{X}_{(i)}$ is the mode-i unfolding of $\mathcal{X}$. However, the optimization problem in (5.1) is NP-hard (197). The nuclear norm heuristic (198) has been used to address this challenge, which turns Equation (5.1) into:

$$\widehat{\mathcal{X}} = \arg\min_{\mathcal{X}} \|\mathbf{d} - \mathcal{A}(\mathcal{X})\|_2^2 + \lambda \sum_i \left\|\mathcal{X}_{(i)}\right\|_*. \tag{5.2}$$

Unlike Equation (5.1), (5.2) is a convex optimization problem with a guaranteed global minimum and can be solved using algorithms such as alternating direction method of multipliers (ADMM) (199). However, if $\mathcal{X}$ has multiple dimensions (as in high-dimensional MRI applications), the memory consumption will increase dramatically and prohibit the storage and operations of $\mathcal{X}$. For instance, a complex tensor with 160×160 voxels, 20 cardiac phases, 6 respiratory phases, 700 inversion times (T_I), and 5 T_2 preparation durations (τ) needs >100 GB for storage, before considering multichannel images and auxiliary variables. Therefore, Equation (5.2) is not feasible for many applications.

A computationally efficient alternative is to decompose the underlying tensor, e.g. into Tucker form (62, 63) as:

$$\mathcal{X} = \mathcal{G} \times_1 \mathbf{U}^{(1)} \times_2 \mathbf{U}^{(2)} \times_3 \ldots \times_n \mathbf{U}^{(n)}, \tag{5.3}$$

where $\mathcal{G} \in \mathbb{C}^{L_1 \times L_2 \times \ldots \times L_d}$ is the core tensor, $\mathbf{U}^{(i)} \in \mathbb{C}^{N_i \times L_i}$ is the factor matrix for the corresponding dimension, $\times_i$ is the mode-i tensor product and $N_i \geq L_i$. Storing and recovering the parameterized $\mathcal{X}$ as in Equation (5.3) ensures that $rank(\mathcal{X}_{(i)}) \leq L_i, \forall i$ and improves memory consumption, as it requires $L_1 L_2 \ldots L_d + N_1 L_1 + N_2 L_2 + \cdots + N_d L_d$ elements rather than $N_1 N_2 \ldots N_d$ elements. The MR Multitasking framework (60) follows this parameterized approach, using sequential reconstruction: temporal factor matrices and the core tensor are estimated from one subset of data, and the spatial factor matrix is reconstructed from another subset of data.

5.2.2 MR Multitasking sequence and reconstruction

Previous section 2.3 already gave a general description about MR Multitasking framework. Here we briefly describe the workflow and define the notations with the practical example of 2D T_1/T_2 mapping.

The sequence cycles through inversion recovery (IR) and T_2-preparation/IR (T_2IR) modules, followed by interleaved acquisition of training data and imaging data. The underlying images are modeled as a 6D image $x(\mathbf{r}, T_c, T_r, T_I, \tau)$ with two spatial dimensions indexed by $\mathbf{r} = [x, y]$, and four temporal dimensions encoding cardiac motion, respiratory motion, T_1 relaxation, and T_2 relaxation, indexed by T_c, T_r, T_I, and τ, respectively. By taking advantage of spatial-temporal correlations (82), the underlying images can be further modeled as a low-rank tensor and can be decomposed in Tucker form:

$$\mathcal{X} = \mathcal{G} \times_1 \mathbf{U}_x \times_2 \mathbf{U}_c \times_3 \mathbf{U}_r \times_4 \mathbf{U}_{T_1} \times_5 \mathbf{U}_{T_2}, \tag{5.4}$$

where $\mathcal{G} \in \mathbb{C}^{L_1 \times L_2 \times L_3 \times L_4 \times L_5}$ is the core tensor, $\mathbf{U}_x \in \mathbb{C}^{N_1 \times L_1}$ is the spatial factor matrix, $\mathbf{U}_c \in \mathbb{C}^{N_2 \times L_2}$, $\mathbf{U}_r \in \mathbb{C}^{N_3 \times L_3}$, $\boldsymbol{U}_{T_1} \in \mathbb{C}^{N_4 \times L_4}$, and $\mathbf{U}_{T_2} \in \mathbb{C}^{N_5 \times L_5}$ contain the basis functions for each corresponding temporal dimension. Equation (5.4) can be seen as a special case of equation (5.3).

The reconstruction is performed with the following steps: (1) simulate a dictionary of T_1/T_2 relaxation signal curves and use SVDs to obtain $\widehat{\mathbf{U}}_{T_1}$ and $\widehat{\mathbf{U}}_{T_2}$; (2) complete the training dataset d_{tr} and perform a high-order SVD (HOSVD) to obtain $\hat{\mathcal{G}}$, $\widehat{\mathbf{U}}_{\text{c}}$, and $\widehat{\mathbf{U}}_{\text{r}}$, defining a temporal factor tensor $\widehat{\Psi} \coloneqq \left(\hat{\mathcal{G}} \times_2 \widehat{\mathbf{U}}_{\text{c}} \times_3 \widehat{\mathbf{U}}_{\text{r}} \times_4 \widehat{\mathbf{U}}_{T_1} \times_5 \widehat{\mathbf{U}}_{T_2}\right) \in \mathbb{C}^{L_1 \times N_2 \times N_3 \times N_4 \times N_5}$; 3) recover spatial coefficients $\mathbf{U}_{\text{x}}$ from imaging data. The last step is done by fixing all the temporal components and solving the following convex optimization problem:

$$\widehat{\mathbf{U}}_{\text{x}} = \arg\min_{\mathbf{U}_{\text{x}}} \left\| \mathbf{d}_{\text{img}} - \Omega_{\text{img}} \left(\mathbf{F}\mathbf{S}\mathbf{U}_{\text{x}} \mathcal{M}\left(\widehat{\Psi}\right) \right) \right\|_2^2 + \lambda_1 R_{\text{s}}(\mathbf{U}_{\text{x}}), \tag{5.5}$$

where $\mathbf{d}_{\text{img}}$ is the imaging data, Ω_{img} is the $(\mathbf{k}, t)$-space sampling mask of the imaging data, $\mathbf{F}$ is the Fourier transform, $\mathbf{S}$ are the sensitivity maps**,** and $R_{\text{s}}(\cdot)$ is a wavelet sparsity regularizer. $\mathcal{M}(\cdot)$ is a temporal re-ordering operator that maps the $(T_{\text{c}}, T_{\text{r}}, T_{\text{I}}, \tau)$-space multidimensional temporal factor tensor in $\mathbb{C}^{L_1 \times N_2 \times N_3 \times N_4 \times N_5}$ to a "real-time" (ungated) temporal factor matrix in $\mathbb{C}^{L_1 \times T}$, where $t = 1,2,\dots,T$ is the real-time stamp indexing the actual readout acquisition order of each timepoint. The reconstructed tensor is then given by the product $\widehat{\mathcal{X}} = \widehat{\Psi} \times_1 \widehat{\mathbf{U}}_{\text{x}}$. Note Equation (5.5) is different from Equations (3.5) and (4.6) with the explicit definition of temporal factor tensor Ψ and reordering operator $\mathcal{M}$.

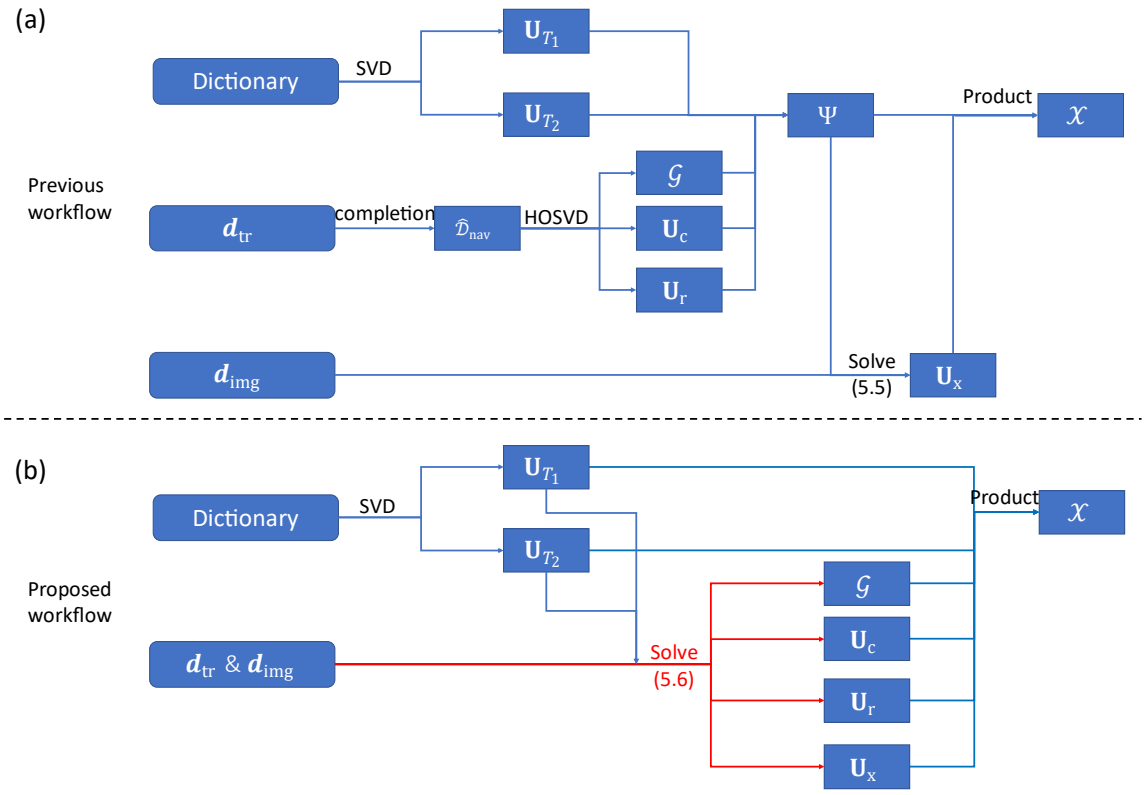

Figure 5.1: Schematic workflow of previous reconstruction approach (a) and the proposed approach (b). The key differences are highlighted in red.

5.3 Proposed Method

Instead of estimating subspace and core tensor from training data and performing subspace-constrained reconstruction with imaging data according to Equation (5.5), we have developed a method for joint estimation of spatial coefficients, core tensor, and motion temporal factor matrices from the entire acquired k-space data in this work. The image reconstruction is formulated as:

$$\hat{\mathcal{G}}, \hat{\mathbf{U}}_{\mathrm{x}}, \hat{\mathbf{U}}_{\mathrm{c}}, \hat{\mathbf{U}}_{r} = \arg\min_{\mathcal{G}, \mathbf{U}_{\mathrm{x}}, \mathbf{U}_{\mathrm{c}}, \mathbf{U}_{r}} \left\| \mathbf{d}_{\mathrm{all}} - \Omega\left(\mathbf{F}\mathbf{S}\mathbf{U}_{\mathrm{x}}\mathcal{M}(\mathcal{G} \times_2 \mathbf{U}_{\mathrm{c}} \times_3 \mathbf{U}_{\mathrm{r}} \times_4 \hat{\mathbf{U}}_{\mathrm{T}_1} \times_5 \hat{\mathbf{U}}_{\mathrm{T}_2})\right) \right\|_2^2 + R(\mathcal{G}, \mathbf{U}_{\mathrm{x}}), s.t. \mathbf{U}_{\mathrm{c}}^{\mathrm{H}}\mathbf{U}_{\mathrm{c}} = \mathbf{I} \text{ and } \mathbf{U}_{r}^{\mathrm{H}}\mathbf{U}_{r} = \mathbf{I}, \tag{5.6}$$

where $\mathbf{d}_{\mathrm{all}}$ is the entire dataset acquired, Ω is the $(\mathbf{k}, t)$-space sampling mask of the entire dataset, $(\cdot)^{\mathrm{H}}$ denotes the conjugate transpose, and $R(\cdot)$ is a regularizer for the core tensor and spatial

coefficients. Note that although it is possible to formulate (5.6) to also update the basis functions for T_1 and T_2 relaxation, our implementation keeps these fixed as $\widehat{\mathbf{U}}_{\mathrm{T}_1}$ and $\widehat{\mathbf{U}}_{\mathrm{T}_2}$ because they are already derived from the simulated signal dictionary and are not subject-dependent. A schematic reconstruction workflow proposed in this work is shown in Figure 5.1 and is compared with the previous approach.

5.3.1 Choice of regularization

To ensure the well-posedness of (5.6), constraints and/or regularization that avoid scaling ambiguity should be employed (200). In this work, we constrained $\mathbf{U}_{\mathrm{c}}$ and $\mathbf{U}_{\mathrm{r}}$ to have orthonormal columns, which serves as a simple way to constrain the column norm and Frobenius norm of these two factor matrices. We adopted the same regularization term for $\mathbf{U}_{\mathrm{x}}$ as in our previous work, i.e., the l_1 norm of the wavelet transform of $\mathbf{U}_{\mathrm{x}}$. Finally, we chose core tensor sparsity as based on previous work on multiway tensor reconstruction (155, 201). In summary, the regularizer can be written as:

$$R(\mathcal{G}, \mathbf{U}_x) = \lambda_1 \|\mathrm{vec}(\mathbf{W}\mathbf{U}_{\mathrm{x}})\|_1 + \lambda_2 \|\mathrm{vec}(\mathcal{G})\|_1, \tag{5.7}$$

where $\mathbf{W}$ is the matrix operator for a wavelet transform, $\mathrm{vec}(\cdot)$ is the vectorization operation, and λ_1 and λ_2 are regularization parameters. The problem in (5.6) becomes:

$$\hat{\mathcal{G}}, \widehat{\mathbf{U}}_{\mathrm{x}}, \widehat{\mathbf{U}}_{\mathrm{c}}, \widehat{\mathbf{U}}_{\mathrm{r}} = \arg \min_{\mathcal{G}, \mathbf{U}_{\mathrm{x}}, \mathbf{U}_{\mathrm{c}}, \mathbf{U}_r} \left\| \mathbf{d}_{\mathrm{all}} - \right.$$

$$\left. \Omega\left(\mathbf{F}\mathbf{S}\mathbf{U}_{\mathrm{x}}\mathcal{M}(\mathcal{G} \times_2 \mathbf{U}_{\mathrm{c}} \times_3 \mathbf{U}_{\mathrm{r}} \times_4 \widehat{\mathbf{U}}_{\mathrm{T}_1} \times_5 \widehat{\mathbf{U}}_{\mathrm{T}_2})\right)\right\|_2^2 + \lambda_1 \|\mathrm{vec}(\mathbf{W}\mathbf{U}_{\mathrm{x}})\|_1 + \tag{5.8}$$

$$\lambda_2 \|\mathrm{vec}(\mathcal{G})\|_1, s.t. \mathbf{U}_{\mathrm{c}}^{\mathrm{H}}\mathbf{U}_{\mathrm{c}} = \mathbf{I} \text{ and } \mathbf{U}_{\mathrm{r}}^{\mathrm{H}}\mathbf{U}_{\mathrm{r}} = \mathbf{I}.$$

Throughout this work, we set $\mathbf{U}_{\mathrm{c}}$ and $\mathbf{U}_{\mathrm{r}}$ to be full rank, as in previous work (60). Despite being complete bases, $\mathbf{U}_{\mathrm{c}}$ and $\mathbf{U}_{\mathrm{r}}$ are still learned by our algorithm, as they affect the sparsity of $\mathcal{G}$. More specifically, the unknown factors of the temporal factor tensor $\widehat{\Psi}$ constitute a subtensor $\Phi :=$

$\mathcal{G} \times_2 \mathbf{U}_c \times_3 \mathbf{U}_r$, in which case $\mathcal{G} = \Phi \times_2 \mathbf{U}_c^H \times_3 \mathbf{U}_r^H$ for unitary $\mathbf{U}_c$ and $\mathbf{U}_r$. A sparsity penalty on $\mathcal{G}$ thus relies on $\mathbf{U}_c^H$ and $\mathbf{U}_r^H$ as data-driven sparsifying transforms on Φ. This re-frames the optimization problem as:

$$\begin{aligned}\hat{\Phi}, \hat{\mathbf{U}}_x, \hat{\mathbf{U}}_c, \hat{\mathbf{U}}_r = \arg\min_{\Phi, \mathbf{U}_x, \mathbf{U}_c, \mathbf{U}_r} \left\| \mathbf{d}_{all} - \Omega\left(\mathbf{F}\mathbf{S}\mathbf{U}_x \mathcal{M}(\Phi \times_4 \hat{\mathbf{U}}_{T_1} \times_5 \hat{\mathbf{U}}_{T_2})\right)\right\|_2^2 + \\ \lambda_1 \|\mathrm{vec}(\mathbf{W}\mathbf{U}_x)\|_1 + \lambda_2 \|\mathrm{vec}(\Phi \times_2 \mathbf{U}_c^H \times_3 \mathbf{U}_r^H)\|_1, s.t. \mathbf{U}_c^H \mathbf{U}_c = \mathbf{I} \text{ and } \mathbf{U}_r^H \mathbf{U}_r = \mathbf{I}.\end{aligned} \tag{5.9}$$

5.3.2 Optimization algorithm

Through variable splitting, Equation (5.9) is equivalent to:

$$\begin{aligned}\hat{\Phi}, \hat{\mathbf{U}}_x, \hat{\mathbf{U}}_c, \hat{\mathbf{U}}_r, \hat{\mathbf{Z}}, \hat{\mathcal{C}} = \arg\min_{\mathcal{G}, \mathbf{U}_x, \mathbf{U}_c, \mathbf{U}_r, \mathbf{Z}, \mathcal{C}} \left\| \mathbf{d}_{all} - \right. \\ \left. \Omega\left(\mathbf{F}\mathbf{S}\mathbf{U}_x \mathcal{M}(\Phi \times_4 \hat{\mathbf{U}}_{T_1} \times_5 \hat{\mathbf{U}}_{T_2})\right)\right\|_2^2 + \lambda_1 \|\mathrm{vec}(\mathbf{Z})\|_1 + \lambda_2 \|\mathrm{vec}(\mathcal{C})\|_1, s.t. \mathbf{U}_c^H \mathbf{U}_c = \\ \mathbf{I}, \mathbf{U}_r^H \mathbf{U}_r = \mathbf{I}, \mathbf{Z} = \mathbf{W}\mathbf{U}_x, \text{and } \mathcal{C} = \Phi \times_2 \mathbf{U}_c^H \times_3 \mathbf{U}_r^H.\end{aligned} \tag{5.10}$$

The (augmented) Lagrangian form can then be written as:

$$\begin{aligned}\mathcal{L}(\Phi, \mathbf{U}_x, \mathbf{U}_c, \mathbf{U}_r, \mathbf{Z}, \mathcal{C}, \mathbf{Y}_1, \mathcal{Y}_2, \mathbf{L}_c, \mathbf{L}_r) = \left\| \mathbf{d}_{all} - \right. \\ \left. \Omega\left(\mathbf{F}\mathbf{S}\mathbf{U}_x \mathcal{M}(\Phi \times_4 \hat{\mathbf{U}}_{T_1} \times_5 \hat{\mathbf{U}}_{T_2})\right)\right\|_2^2 + \lambda_1 \|\mathrm{vec}(\mathbf{Z})\|_1 + \lambda_2 \|\mathrm{vec}(\mathcal{C})\|_1 + \\ \langle \mathbf{Y}_1, \mathbf{W}\mathbf{U}_x - \mathbf{Z} \rangle + \frac{\rho_1}{2} \|\mathbf{W}\mathbf{U}_x - \mathbf{Z}\|_F^2 + \langle \mathrm{mat}(\mathcal{Y}_2), \mathrm{mat}(\Phi \times_2 \mathbf{U}_c^H \times_3 \mathbf{U}_r^H - \mathcal{C}) \rangle + \\ \frac{\rho_2}{2} \|\mathrm{mat}(\Phi \times_2 \mathbf{U}_c^H \times_3 \mathbf{U}_r^H - \mathcal{C})\|_F^2 + \mathrm{tr}\left(\mathbf{L}_c^H (\mathbf{U}_c^H \mathbf{U}_c - \mathbf{I})\right) + \mathrm{tr}\left(\mathbf{L}_r^H (\mathbf{U}_r^H \mathbf{U}_r - \mathbf{I})\right),\end{aligned} \tag{5.11}$$

where $\mathbf{Y}_1$, $\mathcal{Y}_2$, $\mathbf{L}_c$, and $\mathbf{L}_r$ are the Lagrange multipliers, ρ_1 and ρ_2 are the penalty parameters, $\mathrm{tr}(\cdot)$ is the matrix trace norm, $\|\cdot\|_F$ is the Frobenius norm, and $\mathrm{mat}(\cdot)$ is an operation that matricizes the tensor with mode-1 unfolding. The unconstrained optimization problem can be solved by ADMM in the following steps:

$$\mathbf{Z}^{k+1} = \arg\min_{\mathbf{Z}} \frac{\rho_1}{2} \|\mathbf{W}\mathbf{U}_x^k - \mathbf{Z}\|_F^2 + \lambda_1 \|\mathrm{vec}(\mathbf{Z})\|_1; \tag{5.12}$$

$$\mathbf{U}_{\mathrm{x}}^{k+1} = \arg\min_{\mathbf{U}_{\mathrm{x}}} \left\| \mathbf{d}_{\mathrm{all}} - \Omega\left(\mathbf{F}\mathbf{S}\mathbf{U}_{\mathrm{x}}\mathcal{M}(\Phi^{k} \times_4 \widehat{\mathbf{U}}_{\mathrm{T}_1} \times_5 \widehat{\mathbf{U}}_{\mathrm{T}_2})\right)\right\|_2^2 + \frac{\rho_1}{2}\left\|\mathbf{W}\mathbf{U}_{\mathrm{x}} + \mathbf{Y}_1^{k}/\rho_1 - \mathbf{Z}^{k+1}\right\|_{\mathrm{F}}^2; \tag{5.13}$$

$$\mathbf{U}_{\mathrm{c}}^{k+1}, \boldsymbol{L}_{\mathrm{c}}^{k+1} = \arg\min_{\mathbf{U}_{\mathrm{c}}, \boldsymbol{L}_{\mathrm{c}}} \frac{\rho_2}{2}\left\|\mathrm{mat}\left(\left(\mathcal{Y}_2^{k}/\rho_2 - \mathcal{C}^{k}\right) \times_2 \mathbf{U}_{\mathrm{c}} \times_3 \mathbf{U}_{\mathrm{r}}^{\mathrm{k}} + \Phi^{k}\right)\right\|_{\mathrm{F}}^2 + \mathrm{tr}\left(\mathbf{L}_c^{\mathrm{H}}(\mathbf{U}_{\mathrm{c}}^{\mathrm{H}}\mathbf{U}_{\mathrm{c}} - \mathbf{I})\right); \tag{5.14}$$

$$\mathbf{U}_{\mathrm{r}}^{k+1}, \mathbf{L}_{\mathrm{r}}^{k+1} = \arg\min_{\mathbf{U}_{\mathrm{r}}, \mathbf{L}_{\mathrm{r}}} \frac{\rho_2}{2}\left\|\mathrm{mat}\left(\left(\mathcal{Y}_2^{k}/\rho_2 - \mathcal{C}^{k}\right) \times_2 \mathbf{U}_{\mathrm{c}}^{k} \times_3 \mathbf{U}_{r} + \Phi^{k}\right)\right\|_{\mathrm{F}}^2 + \mathrm{tr}\left(\mathbf{L}_{\mathrm{r}}^{\mathrm{H}}(\mathbf{U}_{\mathrm{r}}^{\mathrm{H}}\mathbf{U}_{\mathrm{r}} - \mathbf{I})\right); \tag{5.15}$$

$$\Phi^{k+1} = \arg\min_{\Phi} \left\| \mathbf{d}_{\mathrm{all}} - \Omega\left(\mathbf{F}\mathbf{S}\mathbf{U}_{\mathrm{x}}^{k+1}\mathcal{M}(\Phi \times_4 \widehat{\mathbf{U}}_{\mathrm{T}_1} \times_5 \widehat{\mathbf{U}}_{\mathrm{T}_2})\right)\right\|_2^2 + \frac{\rho_2}{2}\left\|\mathrm{mat}\left(\left(\mathcal{Y}_2^{k}/\rho_2 - \mathcal{C}^{k}\right) \times_2 \mathbf{U}_{\mathrm{c}}^{k+1} \times_3 \mathbf{U}_{\mathrm{r}}^{k+1} + \Phi\right)\right\|_{\mathrm{F}}^2; \tag{5.16}$$

$$\mathcal{C}^{k+1} = \arg\min_{\mathcal{C}} \frac{\rho_2}{2}\left\|\mathrm{mat}\left(\mathcal{C} - \mathcal{Y}_2^{k}/\rho_2 - \Phi^{k+1} \times_2 (\mathbf{U}_{\mathrm{c}}^{k+1})^{\mathrm{H}} \times_3 (\mathbf{U}_{\mathrm{r}}^{k+1})^{\mathrm{H}}\right)\right\|_{\mathrm{F}}^2 + \lambda_2\|\mathrm{vec}(\mathcal{C})\|_1; \tag{5.17}$$

$$\mathbf{Y}_1^{k+1} = \mathbf{Y}_1^{k} + \rho_1(\mathbf{W}\mathbf{U}_{\mathrm{x}}^{k+1} - \mathbf{Z}^{k+1}); \tag{5.18}$$

$$\mathcal{Y}_2^{k+1} = \mathcal{Y}_2^{k} + \rho_2(\Phi^{k+1} \times_2 (\mathbf{U}_{\mathrm{c}}^{k+1})^{\mathrm{H}} \times_3 (\mathbf{U}_{\mathrm{r}}^{k+1})^{\mathrm{H}} - \mathcal{C}^{k+1}). \tag{5.19}$$

The steps in Equations (5.18) and (5.19) are the multiplier updates with gradient ascent, and the subproblems in Equations (5.13) and (5.16) are least-squares problems which can be solved using the preconditioned conjugate gradient (PCG) algorithm.

The subproblem in Equation (5.12) is an l_1 regularized linear regression problem, which has an analytical solution (202):

$$\mathbf{Z}^{k+1} = \max\left(\left|\mathbf{W}\mathbf{U}_{\mathrm{x}}^{k} + \mathbf{Y}_1^{k}/\rho_1\right| - \lambda_1/\rho_1, 0\right) \cdot \mathrm{sign}\left(\mathbf{W}\mathbf{U}_{\mathrm{x}}^{k} + \mathbf{Y}_1^{k}/\rho_1\right). \tag{5.20}$$

Similarly, the solution to Equation (5.17) is:

$$\mathcal{C}^{k+1} = \max\left(\left|\mathcal{Y}_2^k/\rho_2 + \Phi^{k+1} \times_2 (\mathbf{U}_\mathrm{c}^{k+1})^\mathrm{H} \times_3 (\mathbf{U}_\mathrm{r}^{k+1})^\mathrm{H}\right| - \lambda_2/\rho_2\right) \cdot \operatorname{sign}\left(\mathcal{Y}_2^k/\rho_2 + \Phi^{k+1} \times_2 (\mathbf{U}_\mathrm{c}^{k+1})^\mathrm{H} \times_3 (\mathbf{U}_\mathrm{r}^{k+1})^\mathrm{H}\right). \quad (5.21)$$

The subproblems in Equations (5.14) and (5.15) could potentially be solved using previous findings on the orthogonal Procrustes problem (203). However, in this work we instead obtained $\mathbf{U}_\mathrm{c}^{k+1}$ and $\mathbf{U}_\mathrm{r}^{k+1}$ from the HOSVD of the current image series $\Phi^k \times_1 \mathbf{U}_\mathrm{x}^{k+1} \times_4 \widehat{\mathbf{U}}_{\mathrm{T}_1} \times_5 \widehat{\mathbf{U}}_{\mathrm{T}_2}$ using alternating least squares (see Property 1 in (204)) with fixed T_1 and T_2 relaxation basis. to alleviate memory constraints, this HOSVD was calculated on $\Phi^k \times_1 [(\mathbf{U}_\mathrm{x}^{k+1})^\mathrm{H}\mathbf{U}_\mathrm{x}^{k+1}]^{-1/2} \times_4 \widehat{\mathbf{U}}_{\mathrm{T}_1} \times_5 \widehat{\mathbf{U}}_{\mathrm{T}_2}$.

For initialization, we get $\mathcal{G}^1$, $\mathbf{U}_\mathrm{c}^1$, and $\mathbf{U}_\mathrm{r}^1$ from the HOSVD of completed $\widehat{\mathcal{D}}_\mathrm{nav}$. Φ^1 is initialized from $\mathcal{G}^1 \times_2 \mathbf{U}_\mathrm{c}^1 \times_3 \mathbf{U}_\mathrm{r}^1$. Then $\mathbf{U}_\mathrm{x}^1$ can be efficiently initialized by setting $\lambda = 0$ in Equation (5.5) and solving the resulting quadratic unregularized least-squares problem. Because Equation (5.8) is non-convex, global convergence is not guaranteed and results will be dependent on this initialization. However, empirical evidence on the matrix case from previous work indicated acceptable convergence behavior in practice (205, 206).

5.3.3 Practical considerations

In practice, system imperfections such as gradient delay will introduce a trajectory dependent oscillation in radial imaging (207). Those fluctuations can be misinterpreted as a signal feature and be overfitted by data-adaptive reconstruction approaches. Previous works (e.g., (208)) have used an orthogonal projection method to remove these effects from estimated subspace and we extended this concept to our approach.

We model the trajectory effects based on the known frequency. Let ϕ^t be the projection angle at time stamp $t(t = 1,2, \dots, T)$. We define the following vector which contains the oscillations for the h_1,h_2,...,h_{n_h}-th order of harmonics:

$$h^t \equiv \begin{pmatrix} e^{ih_1\phi^t} \\ e^{-ih_1\phi^t} \\ \vdots \\ e^{ih_{n_h}\phi^t} \\ e^{-ih_{n_h}\phi^t} \end{pmatrix}, \tag{5.22}$$

and stacking h^t column-wise forms the harmonic matrix $\mathbf{H} \in \mathbb{C}^{(2n_h)\times T}$.

Instead of removing the oscillation basis in $\mathbf{H}$ from $\mathbf{\Psi}_{\mathrm{rt}} \coloneqq \mathcal{M}(\Psi)$ using orthogonal projection, we seek to recover the spatial components corresponding to the oscillations and discard them later. Specifically, we construct:

$$\mathbf{\Psi}_{\mathrm{rt,cor}}^{k} = \begin{pmatrix} \mathcal{M}(\Psi^k) - \mathcal{M}(\Psi^k)\mathbf{H}^{+}\mathbf{H} \\ \mathbf{H} \end{pmatrix}, \tag{5.23}$$

a corrected real-time temporal factor matrix that explicitly models the oscillations. We solve:

$$\mathbf{U}_{\mathrm{x}}^{k+1} = \arg\min_{\mathbf{U}_{\mathrm{x}}} \left\| \mathbf{d}_{\mathrm{all}} - \Omega\left(\mathbf{F}\mathbf{S}\mathbf{U}_{\mathrm{x}}\mathbf{\Psi}_{\mathrm{rt,cor}}^{k}\right) \right\|_2^2 + \frac{\rho_1}{2} \left\| \mathbf{W}\mathbf{U}_{\mathrm{x}} + \mathbf{Y}_1^k/\rho_1 - \mathbf{Z}^{k+1} \right\|_{\mathrm{F}}^2, \tag{5.24}$$

instead of (5.13), after which we only keep the first L_1 components of $\mathbf{U}_{\mathrm{x}}$.

The implementation details of the overall algorithm are summarized in pseudo-code **Algorithm 1**.

Algorithm 1 Proposed reconstruction

Input:

Acquired k-space data $\mathbf{d}$, sampling mask Ω, sensitivity map $\mathbf{S}$

T_1 and T_2 basis $\widehat{\mathbf{U}}_{\mathrm{T}_1}$ and $\widehat{\mathbf{U}}_{\mathrm{T}_2}$

Harmonic matrix $\mathbf{H}$, reordering operator $\mathcal{M}$

Rank choices L_1, L_2 (full rank), and L_3 (full rank)

Regularization parameters λ_1, λ_2, ρ_1, ρ_2

Output:

Reconstructed images $\hat{\mathcal{G}} \times_1 \widehat{\mathbf{U}}_{\mathrm{x}} \times_2 \widehat{\mathbf{U}}_{\mathrm{c}} \times_3 \widehat{\mathbf{U}}_{\mathrm{r}} \times_4 \widehat{\mathbf{U}}_{\mathrm{T}_1} \times_5 \widehat{\mathbf{U}}_{\mathrm{T}_2}$

Initialization

Complete $\widehat{\mathcal{D}}_{\text{nav}}$ and get $\mathcal{G}^1$, $\mathbf{U}_{\text{c}}^1$, and $\mathbf{U}_r^1$ with HOSVD.

Compute $\Psi^1 = \mathcal{G}^1 \times_2 \mathbf{U}_{\text{c}}^1 \times_3 \mathbf{U}_r^1 \times_4 \widehat{\mathbf{U}}_{\text{T}_1} \times_5 \widehat{\mathbf{U}}_{\text{T}_2}$ and $\boldsymbol{\Psi}_{\text{rt,cor}}^1$ from (5.23).

Solve $\mathbf{U}_{\text{x}}^1$ from $\arg\min_{\mathbf{U}_{\text{x}}} \left\| \mathbf{d}_{all} - \Omega\left(\mathbf{FSU}_{\text{x}} \boldsymbol{\Psi}_{\text{rt,cor}}^1\right) \right\|_2^2$.

Set $\mathbf{Y}_1^1$ and $\mathcal{Y}_2^1$ to 0, Compute $\Phi = \mathcal{G}^1 \times_2 \mathbf{U}_{\text{c}}^1 \times_3 \mathbf{U}_{\text{r}}^1$.

For k=1 to 14 **do**

Compute $\mathbf{Z}^{k+1}$ from (5.12) and $\mathbf{U}_{\text{x}}^{k+1}$ from (5.24).

Keep the first L_1 components of $\mathbf{U}_{\text{x}}^{k+1}$ and compute $\mathcal{T} = \Phi^k \times_1 [(\mathbf{U}_{\text{x}}^{k+1})^{\text{H}} \mathbf{U}_{\text{x}}^{k+1}]^{-1/2} \times_4 \widehat{\mathbf{U}}_{\text{T}_1} \times_5 \widehat{\mathbf{U}}_{\text{T}_2}$.

Compute $\mathbf{U}_{\text{c}}^{k+1}$ and $\mathbf{U}_{\text{r}}^{k+1}$ from HOSVD of $\mathcal{T}$.

Compute Φ^{k+1} from (5.16) and $\mathcal{C}^{k+1}$ from (5.17).

Compute $\mathbf{Y}_1^{k+1}$ from (5.18) and $\mathcal{Y}_2^{k+1}$ from (5.19).

Update $\Psi^k = \Phi^k \times_4 \widehat{\mathbf{U}}_{\text{T}_1} \times_5 \widehat{\mathbf{U}}_{\text{T}_2}$ and compute $\boldsymbol{\Psi}_{\text{rt,cor}}^k$ from (5.23)

Set $\rho_1 = 1.1\rho_1$ and $\rho_2 = 1.1\rho_2$

End for

Return $\widehat{\mathbf{U}}_{\text{x}} = \mathbf{U}_{\text{x}}^{15}$, $\widehat{\mathbf{U}}_{\text{c}} = \mathbf{U}_{\text{c}}^{15}$, $\widehat{\mathbf{U}}_{\text{r}} = \mathbf{U}_r^{15}$, $\hat{\mathcal{G}} = \Phi^{15} \times_2 \widehat{\mathbf{U}}_{\text{c}}^{\text{H}} \times_3 \widehat{\mathbf{U}}_{\text{r}}^{\text{H}}$

5.4 Experiments

5.4.1 Numerical simulations

A numerical phantom was created from the XCAT phantom (209) with 20 cardiac phases ($N_2 = 20$) and 6 respiratory phases ($N_3 = 6$). The average heart rate and respiration rate were set to be 75 bpm and 15 bpm, respectively, with 10% standard deviation. Typical T_1/T_2 values at 3T were assigned to different tissue types. The sequence diagram and acquisition scheme developed

in previous work (60) was used to simulate k-space data. The sequence parameters shown in Table 5.1 were used for simulation. Five T_2IR modules with preparation durations = 0, 30, 40, 50, 60 ms (with 0 corresponding to a standard IR, $N_5 = 5$), and 720 readouts were collected in each shot ($N_4 = 720$). The matrix size = [320,320] with 2-fold oversampling ($N_1 = 320^2$). MRI acquisition was simulated based on the preparation pulses and Bloch equations with the programmed cardiac and respiratory motion states, and k-space data were generated using 12 simulated coils and the radial trajectory for training data (0° radial spoke) and imaging data (golden angle). Partial-volume effects were simulated by averaging the signal from 16 adjacent 0.5-mm thick slices for a typical slice thickness prescribed in in-vivo studies.

Table 5.1: Sequence parameters used for numerical simulation and in-vivo studies of this work. The FOV and matrix size includes 2-fold oversampling. BW: bandwidth.

FOV (mm^2)	540 × 540	**Slice thickness (mm)**	8
Matrix size	320 × 320	**Resolution (mm)**	1.7 × 1.7
TE (ms)	1.6	**TR (ms)**	3.6
Number of readouts per shot	720	**Recovery period (s)**	2.6
T_2IR prep durations (ms)	0, 30, 40, 50, 60	**Pixel BW (Hz/pixel)**	1008
Flip angle (°)	5	**Acquisition time (s)**	90

Image reconstruction was performed with the previous fixed basis approach (60) and with the proposed joint update approach. The rank choices were kept the same as before (60), i.e., $L_1 = 48$, $L_2 = 20$, $L_3 = 6$, $L_4 = 5$, $L_5 = 5$, and were used for both reconstruction approaches. The reconstructed images at the end-expiration and end-diastolic phase were then fitted to get the T_1

and T_2 maps. Root mean squared error (RMSE), bias (μ), and precision (σ) between the ground truth and the reconstructed maps were used as the evaluation metric. They are defined as:

$$\mu = \frac{\sum_{i,j}\left(\theta_{i,j} - \hat{\theta}_{i,j}\right)}{N}, \tag{5.25}$$

$$\sigma = \sqrt{\sum_{i,j}\left(\theta_{i,j} - \hat{\theta}_{i,j} - \mu\right)^2 / N}, \tag{5.26}$$

$$\mathrm{RMSE} = \sqrt{\sum_{i,j}\left(\theta_{i,j} - \hat{\theta}_{i,j}\right)^2 / N}, \tag{5.27}$$

where $\theta_{i,j}$ and $\hat{\theta}_{i,j}$ are the ground truth and the reconstructed parameter maps at voxel location (i,j), and N is total number of voxels in the region of interest. Also note that $\mathrm{RMSE} = \sqrt{\mu^2 + \sigma^2}$, so the explicit computation of bias and precision will help explain the results of RMSE.

To evaluate the reconstruction performance at different scan time, reconstruction was performed at different scan lengths ([39,52,65,78,91]s).

To evaluate if the temporal basis estimation was improved by the proposed approach, we analyzed the projection error of the underlying gold standard images $\mathcal{X}$ onto the temporal basis estimated with different reconstruction approaches. As the gold standard images are impractically large (>100 GB) to be created and stored, we compressed it with $\widetilde{\mathcal{X}} = \mathcal{X} \times_4 \widehat{\mathbf{U}}_{T_1}^{H}$, which made the tensor more than 100 times smaller while preserving Frobenius norm distance. Letting $\widehat{\Psi}$ to be the multi-dimensional temporal basis estimated during reconstruction and $\widetilde{\Psi} = \widehat{\Psi} \times_4 \widehat{\mathbf{U}}_{T_1}^{H}$ to be its compressed form, the projection error is calculated as:

$$\epsilon = \frac{\left\| \widetilde{\mathcal{X}}_{(1)} - \widetilde{\mathcal{X}}_{(1)}\left(\widetilde{\Psi}_{(1)}\right)^{+}\widetilde{\Psi}_{(1)} \right\|_F^2}{\left\| \widetilde{\mathcal{X}}_{(1)} \right\|_F^2} \times 100\%, \tag{5.28}$$

where $(\cdot)^+$ is the pseudo-inverse, and $\|\cdot\|_F$ is the Frobenius norm. We also computed $\widetilde{\Psi}$ from the HOSVD of $\widetilde{\mathcal{X}}$ with the same rank choices $[L_1, L_2, L_3, L_4, L_5]$ as in the reconstruction and calculated the projection error using Equation (5.28), which established the baseline for best possible resultssame rank. As this was done directly on multidimensional gold standard images, the projection error for the HOSVD is invariant to scan time.

For parameter choices, the regularization parameter λ_1 in the fixed basis approach was optimized for best RMSE, and we optimized λ_2 in the joint update approach with the same λ_1 for best RMSE. That led to $\lambda_1 = 1.5 \times 10^{-5}$ and $\lambda_2 = 6 \times 10^{-3}$. We initialized $\rho_1 = \lambda_1$ and ρ_2 to be the 70th percentile of $|\mathrm{vec}(\mathcal{G}^1)|$.

5.4.2 In-vivo study

The study involving human participants was approved by the institutional review board at Cedars-Sinai Medical Center. Prior to their participation, written informed consent was obtained from all subjects. A group of 10 healthy volunteers (3 males) with an average age of 36.4 ± 12.5 years were scanned forthe study. Imaging was performed using a 3T scanner (MAGNETOM Vida, Siemens Healthineers, Erlangen, Germany) equipped with a standard 18-channel body coil and an integrated spine matrix coil. Multitasking acquisition was performed using the same sequence in the mid-ventricular slice with short-axis view. The sequence parameters were still set as in Table 5.1**Error! Reference source not found.**. The acquisition was performed twice to assess repeatability.

The reconstruction was performed with 90-second length and 50-second length (by retrospective truncation) of data. The scan time of 50 s was chosen based on the results from simulations, which will be shown in the following section. The rank choices were kept the same as in numerical simulations, i.e., $L_1 = 48$, $L_2 = 20$, $L_3 = 6$, $L_4 = 5$, and $L_5 = 5$. The

regularization parameter λ_1 was obtained for each subject by estimating the Laplace distribution parameter of the wavelet coefficients using k-means clustering of the least-squares solution, a Bayesian re-interpretation of (210). This was kept the same for the fixed basis approach and the proposed joint update approach. The parameter λ_2 was tuned towards the best visual quality on one subject and were kept the same for all subjects ($\lambda_2 = 5 \times 10^{-5}$) and different scan length. We initialized $\rho_1 = \lambda_1$ and ρ_2 to be the 70th percentile of $|\mathrm{vec}(\mathcal{G}^1)|$. The reconstruction was first performed without using harmonic matrix **H**. When examining the spectrum of $\mathcal{M}(\Psi^k)$, we found frequency components corresponding to the 3rd and 13th harmonic. Therefore, **H** was set accordingly in our dataset.

The myocardial T_1 and T_2 maps generated from different approaches were analyzed using the AHA 6-segment model. The epicardial and endocardial contours were drawn on the black-blood image (inversion time near 1080 ms) reconstructed by the previously used fixed basis approach at 90s acquisition time and were kept the same for analysis of different approaches and different scan times. The maps were evaluated using two quantitative metrics: precision and repeatability. Precision was defined as the standard deviation within a myocardium segment in healthy subjects. Repeatability was defined as the standard deviation of the repeated measurements for the same segment. The Wilcoxon signed-rank test was used (with *signrank*() function in MATLAB R022b) to compare measurement precision and repeatability from different reconstruction approaches, with $P<0.05$ considered as significant.

All reconstructions were performed using MATLAB 2016b on a Linux workstation with a 3.08-GHz dual 16-core Intel Xeon processor and 256 GB RAM. The fixed basis approach took about 40 min for one slice, and the proposed joint update approach took about 75 min for one slice.

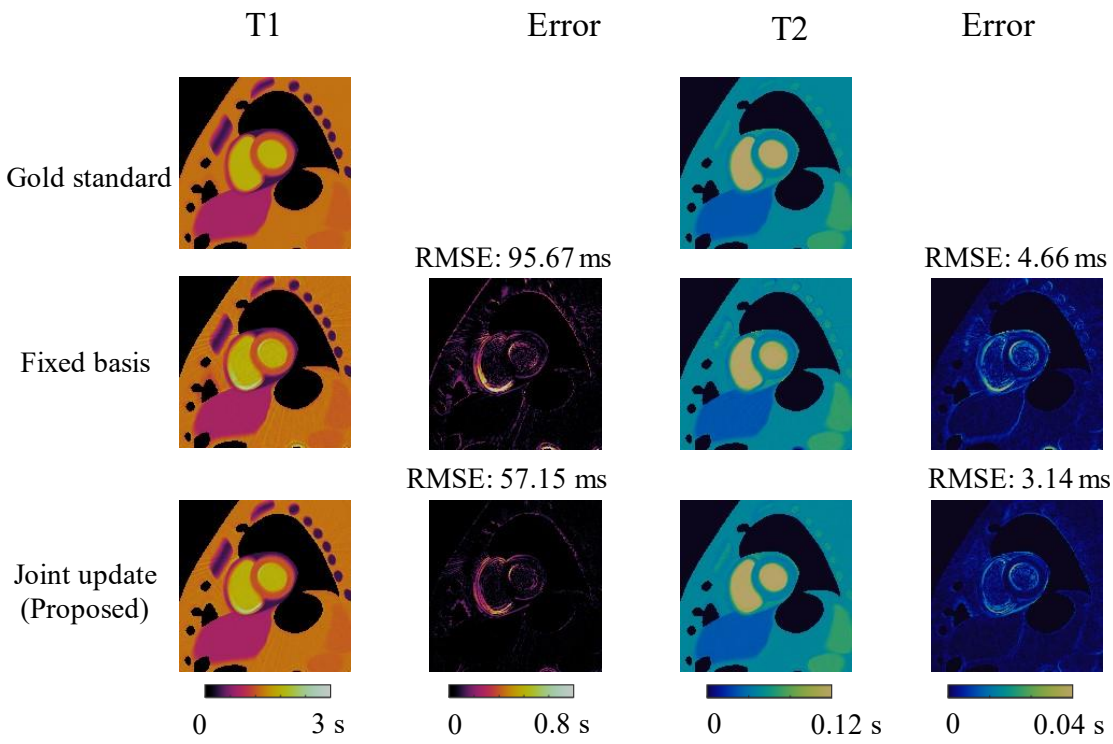

Figure 5.2: Reconstructed parametric maps of T_1, T_2, and corresponding error maps against the gold standard in the case of scan length = 90 s. The comparison showed superior reconstruction performance using the proposed approach.

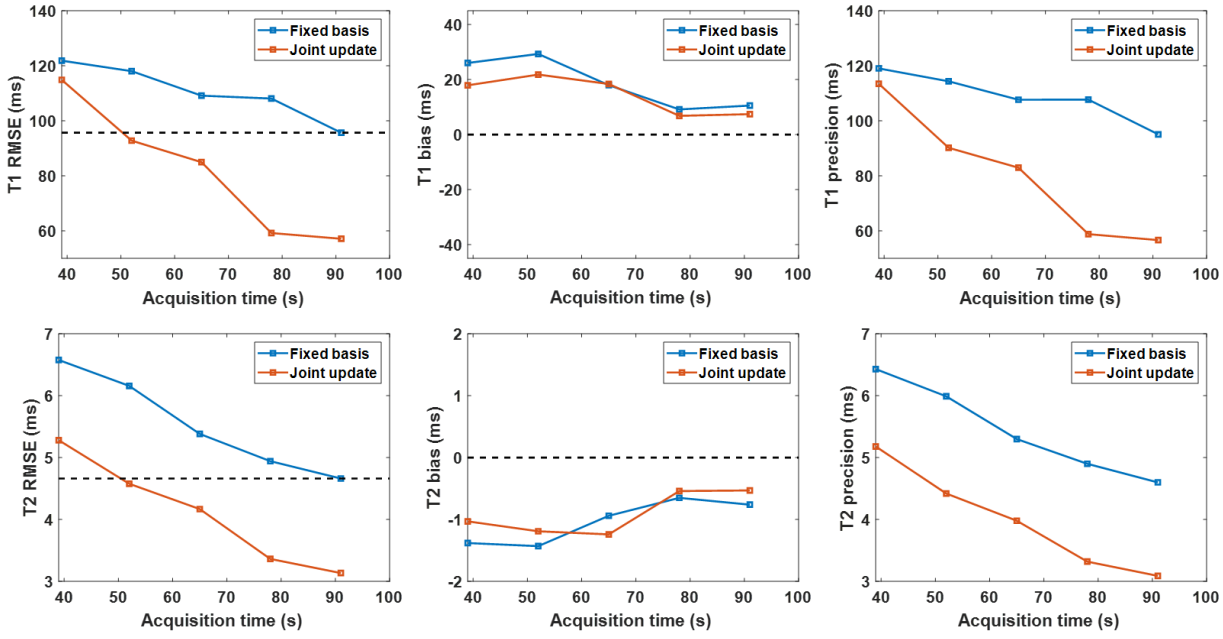

Figure 5.3: The RMSE, bias, and precision of T_1 and T_2 mapping from different reconstruction approaches at various acquisition lengths.

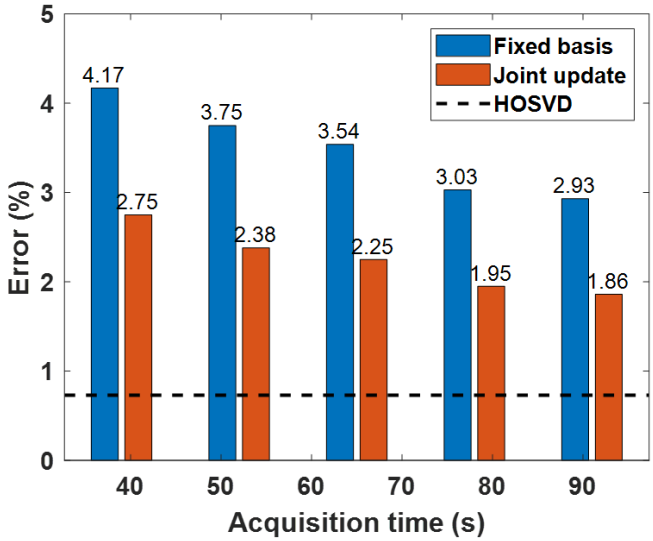

Figure 5.4: Projection error of the gold standard images onto the estimated temporal subspace from different approaches and at different acquisition times. The result from HOSVD (0.73%) can be seen as the best possible result by low-rank tensor modelling. HOSVD: high-order singular value decomposition.

5.5 Results

5.5.1 Numerical simulations

The reconstructed T_1 and T_2 maps obtained from the previous and proposed approach at the scan time of 90 s are compared in Figure 5.2. The proposed approach exhibited lower residual error, as evidenced by the RMSE values and the error maps. Figure 5.3 illustrates the impact of scan time on different approaches, with the proposed approach consistently outperforming the fixed subspace approach in terms of T_1 and T_2 RMSE across all examined scan times. Even when the scan time was truncated to 50 s, the proposed approach still yielded slightly superior reconstructions compared to the previous approach at a 90-s scan time. Further analysis decomposing RMSE into bias and precision showed that the improvement of proposed reconstruction mainly came from improved precision. The comparison of projection error shown in Figure 5.4 demonstrated that the proposed joint update approach achieved better temporal

subspace estimation than the fixed basis approach at all scan times studied. Using the projection error from HOSVD as a baseline (0.73%), the proposed approach nearly achieved a two-fold improvement at the scan time of 90 s.

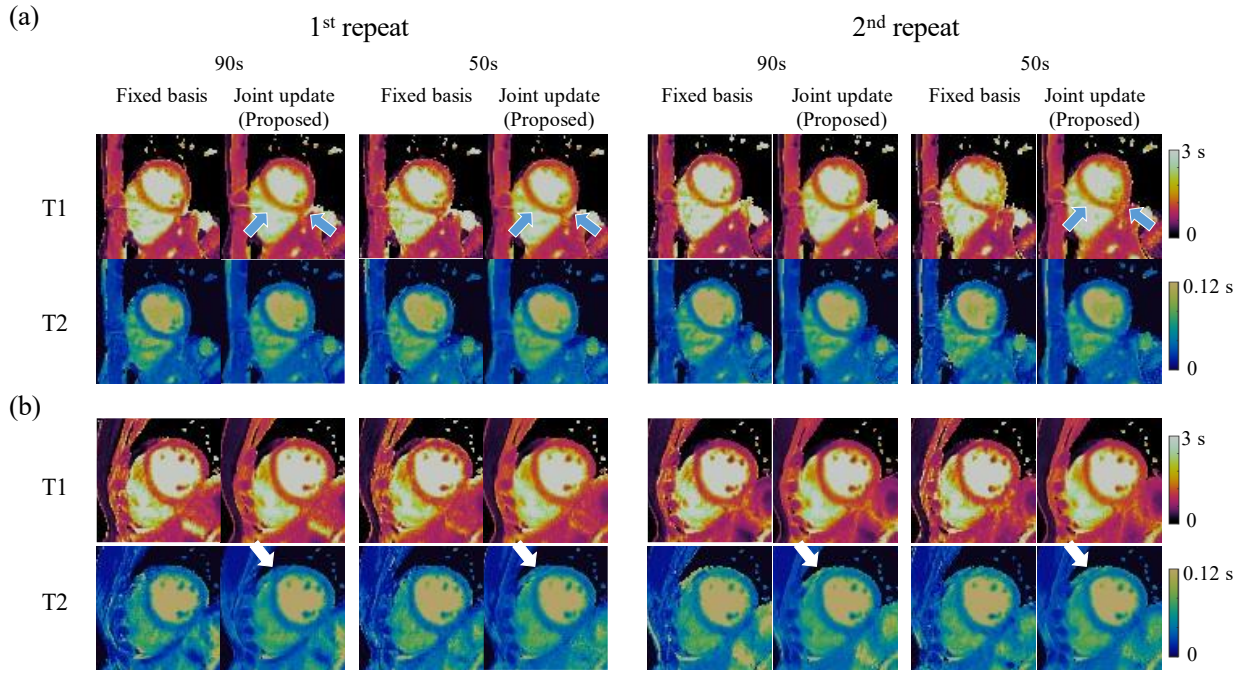

Figure 5.5: The T_1 and T_2 maps of two healthy subjects (a) and (b) with different reconstruction approaches with 1st and 2nd (repeated) scan. The proposed approach better preserved myocardium boundary around the inferior segment (blue arrow) and improved homogeneity of the septum (blue arrow) as depicted in (a). It also improved SNR around the anterior segment (white arrow) as shown in (b).

5.5.2 In-vivo studies

Figure 5.5 compares T_1 and T_2 maps reconstructed with different approaches for two representative healthy subjects, each with two acquisition repeats. Compared to the fixed basis approach with the same acquisition time, the proposed approach better preserved myocardium boundary around the inferior segment (blue arrow) and improved homogeneity of the septum (blue arrow) as depicted in Figure 5.5(a). Furthermore, it improved SNR around the anterior segment (white arrow) as shown in Figure 5.5 (b). Remarkably, the visual quality of the proposed

reconstruction with a 50-s scan time was comparable to that of the fixed basis approach with 90-s scan time.

Table 5.2: Quantitative evaluation on precision and repeatability for in-vivo study.

Median precision (ms) and quartile range

Scan time	90s		50s	
	T_1	T_2	T_1	T_2
Fixed basis	125.18 [101.65,179.83]	4.53 [3.60,7.17]	129.57 [101.40,156.54]	4.98 [4.17,7.51]
Joint update	**99.94 [73.49,129.99]**	**3.99 [2.94,4.66]**	**107.27 [89.58,130.05]**	**4.51 [3.75,5.90]**

Median repeatability (ms) and quartile range

Scan time	90s		50s	
	T_1	T_2	T_1	T_2
Fixed basis	76.42 [28.06,132.75]	2.89 [1.55,5.43]	72.36 [31.96,131.20]	3.09 [1.06,5.71]
Joint update	**51.01 [27.95,88.68]**	**2.10 [1.04,4.13]**	51.08 [19.35,98.74]	**2.15 [0.79,4.19]**

Table 5.2 summarizes the median precision and repeatability, along with the quartile range, of T_1 and T_2 mapping from different reconstruction approaches. The proposed approach demonstrated improved precision and repeatability at both scan times. The distribution and statistical comparison in Figure 5.6 reveal significant precision improvement ($P<0.001$ for T_1 at both scan times, $P<0.001$ for T_2 at 90 s, $P=0.002$ for T_2 at 50s). The repeatability improvement was also significant for T_1 at 90 s ($P=0.011$) and for T_2 at both scan times ($P<0.001$). No significant difference in T_1 repeatability at 50 s was found between different methods. When comparing across different scan times, the proposed approach yielded significantly better T_1 precision ($P<0.001$) and T_2 repeatability ($P=0.012$) with 50-s data compared to the fixed basis approach with 90-s data. No significant difference was found for T_2 precision ($P=0.791$) and T_1 repeatability ($P=0.248$).

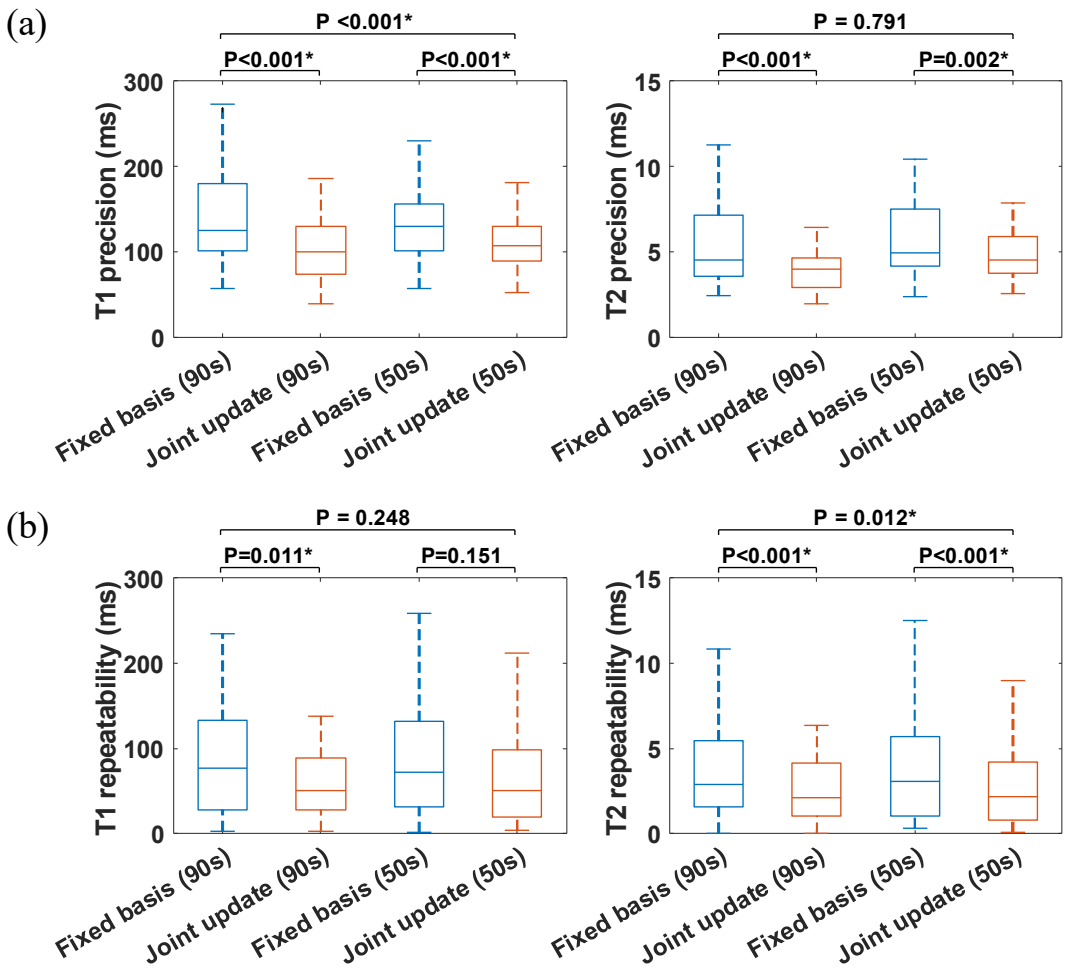

Figure 5.6: Distribution and comparison of T_1 and T_2 precision and repeatability from different reconstruction approaches. Statistical significance is indicated with *. Whisker length is set to 1.5 times quartile range.

5.6 Discussion

Compressed sensing and tensor/array modeling are promising for multi-dimensional imaging within a clinically feasible scan time. At present, most low-rank tensor imaging approaches rely on obtaining a temporal subspace from an auxiliary dataset and then performing subspace-constrained reconstruction, which could compromise reconstruction performance. In this work, we developed a novel approach that alternately estimated the factor matrices and core tensor for a low-rank tensor from the entire acquired data. The framework was inspired by (155), which

adopted a sparse core-tensor prior and estimated the core tensor and spatial coefficients from the imaging data. Here our work took a step further by incorporating the temporal basis update. This update scheme can also be interpreted from the perspective of transform sparsity, aiming to further sparsity the core tensor with appropriate factor matrices. Our work also has a connection with previous blind compressed sensing (BCS) work (205, 206), representing a preliminary extension of BCS from matrices to tensors. Experimental results demonstrated improved precision and repeatability for quantitative mapping using our proposed approach compared to fixed basis reconstruction methods. Although our evaluation primarily focused on T_1 and T_2 mapping with MR Multitasking, the developed framework should be applicable to other biomarkers (such as $T_1\rho$, ADC) and will improve other subspace constrained low-rank tensor reconstructions such as (155, 193).

The trajectory-dependent signal oscillations in a radial acquisition pose known challenges, and these patterns could be overfitted as a signal contribution with a data-adaptive reconstruction scheme. In this study, we partially addressed the oscillations by modeling them as a group of harmonics and extended the orthogonal projection approach used in previous work (207, 208). Instead of removing the components from the estimated real-time basis $\mathbf{\Psi}_{\mathrm{rt}}$, we intentionally added the relevant harmonics to $\mathbf{\Psi}_{\mathrm{rt}}$. This approach could be seen as a "spectral trap" that helps capture the spatial components associated with the oscillations, which can be subsequently discarded. Our preliminary experiments (not shown) found that this approach yielded slightly superior results than performing orthogonal projection to remove the harmonics from $\mathbf{\Psi}_{\mathrm{rt}}$.

The rank choice in this work, with $L_1 = 48$, $L_2 = 20$, $L_3 = 6$, $L_4 = 5$, $L_5 = 5$, was kept the same as previous work (60) to ensure a fair comparison. The rank of the T_1 dimension was chosen based on the -40 dB threshold on the normalized singular value curves of the simulated dictionary.

The rank of spatial dimension was empirically chosen as 48. The ranks of cardiac and respiratory dimension were not truncated. The update of factor matrices for those two dimensions were for learning a sparsifying transform for Φ. This is similar to the idea in dictionary learning (211) and BCS. In the meantime, it should be noted that the framework established here can be extended to scenarios where all dimensions are truncated by slightly tweaking the optimization algorithm. An additional regularization parameter λ_2 was introduced in the proposed approach and it was chosen as 5×10^{-5} based on visual assessment of one dataset. Our preliminary study suggested that it generalized well to other datasets, therefore tuning of λ_2 in practical usage should not pose a significant challenge.

In numerical simulations, our proposed approach consistently outperformed the previous approach in terms of T_1 and T_2 RMSE across all scan times. Further analysis showed that the observed benefit was primarily a result of improved precision. The evaluation of temporal basis estimation from different approaches indicated that our proposed approach achieved superior estimation of the temporal subspace by leveraging the complete acquired dataset. This finding potentially explains the subsequent improvement in the quality of T_1 and T_2 maps. Since no ground truth was available for the in-vivo study, we mainly evaluated precision and repeatability, both of which are critical metrics in quantitative imaging. The improvements of our proposed approach in precision had the potential for facilitating diagnosis, longitudinal tracking, and treatment monitoring.

With the proposed approach, T_1 and T_2 RMSE at a 50-s scan time were slightly better than the fixed basis approach at a 90-s scan time in the simulation. This observation motivated us to study these two scan times using in-vivo data. The results from in-vivo data demonstrated that our proposed approach at 50 s yielded comparable results in terms of T_1 repeatability and T_2 precision,

and significantly better results in terms of T_1 precision and T_2 repeatability, when compared to the fixed basis approach with 90-s scan time. These findings indicate the potential for scan time reduction. However, there are two potential factors that could influence the result in a prospective study: 1) In this work, we used the sensitivity map estimated with 90-s data to avoid introducing additional confounders. However, this estimation could be compromised with a shorter acquisition time. This issue may be mitigated by utilizing a separate short scan for sensitivity estimation or implementing better sensitivity estimation approaches, such as ESPIRiT (212) that may help alleviate this issue. 2) We used binning results from the 90-s data to avoid motion mismatch when comparing results with different scan lengths. However, the performance of motion binning may be impacted by a shorter scan. Further investigation is warranted to assess and characterize the impact of these factors.

One interesting future direction would be to extend the framework for a "navigator-less" acquisition, which solely collects imaging data. This approach has the potential to alleviate trajectory-dependent effects associated with the interleaved acquisition of training data and imaging data. By eliminating the need for training data, imaging efficiency could be enhanced, enabling higher temporal and spatial resolutions. This extension holds promise for further enhancing multi-dimensional imaging using low-rank tensor constraints.

5.7 Conclusion

We developed a novel low-rank tensor reconstruction approach which alternated between solving the factor matrices and the core tensor from the entire acquired dataset. The proposed approach improved precision and repeatability for quantitative imaging and has the potential for further reducing scan time.

CHAPTER 6 Conclusions and Future Directions

6.1 Summary

Quantitative MRI directly measures underlying tissue properties and holds great promise for comprehensive tissue characterization and objective disease diagnosis. In contrast to qualitative images, quantitative imaging offers the potential for treatment monitoring and early diagnosis. Combining different biomarkers through multiparametric mapping further enhances diagnostic accuracy, including sensitivity and specificity. However, certain technical challenges hinder the clinical adoption of multiparametric mapping, including prolonged scan time for acquiring different biomarkers, physiological motion within a scan, and misaligned multiparametric maps from separate scans.

Recent technical developments, such as the advances in MRF technique, have enabled simultaneous multiparametric mapping within a clinically feasible scan time. Nevertheless, challenges remain in handling intra-scan physiological motion or random movements, and the application of MR fingerprinting into the heart often requires breath-holding and ECG gating to freeze motion or external motion monitors for tracking respiratory and/or cardiac motion. Multiple breath holds could lead to patient fatigue, and the ECG signal may be prone to errors at high field strengths.

The MR Multitasking framework is promising for motion-resolved, multi-parametric mapping. This dissertation focuses on advancing MR Multitasking framework for more comprehensive tissue characterization, with a particular emphasis on the extraction of T_2*, susceptibility, and fat information from multi-echo acquisitions. Moreover, a novel reconstruction approach is developed, which could improve precision and repeatability of quantitative measurements from

MR Multitasking and potentially reduce scan time. It is expected the dissertation will contribute to enhancing the comprehensiveness and robustness of MR Multitasking framework for disease diagnosis and monitoring. By addressing technical challenges and improving quantitative performance, this ultimate purpose is to enable widespread clinical use of multiparametric mapping, facilitating more accurate and efficient disease assessments.

CHAPTER 3 introduced a technique for three-dimensional simultaneous brain mapping of T_1, T_2, T_2*, and magnetic susceptibility. Full flow compensation was implemented along all gradient directions and for all echoes to reduce confounding flow effects onto susceptibility. The technique achieved whole brain coverage with an anisotropic resolution of $0.7 \times 1.4 \times 2$ mm^3 in a 9.1-min scan. It was evaluated on phantoms and healthy volunteers, yielding measurements that were comparable to those from conventional references. We also demonstrated the feasibility of contrast-weighted image synthesis using multi-parametric maps from the technique.

CHAPTER 4 further developed the technique for free-breathing, non-ECG, simultaneous myocardial T_1, T_2, T_2*, and fat-fraction mapping and addressed the technical challenges related to temporal resolution and scan time. Instead of acquiring multi-echo FLASH readouts for both training and imaging data, we proposed a novel approach which utilized a single-echo, short T_R readout for training data to enhance temporal resolution and imaging efficiency of the sequence. The technique was evaluated on static and motion phantoms and healthy volunteers, which produced repeatable quantitative measurements that agreed with those from conventional breath-held, ECG-triggered references in a 2.5-min acquisition. The image quality assessment from an imaging cardiologist also indicated a statistically significant improvement in T_1 map quality of the proposed approach. The technique was further incorporated into the clinical protocol for patients with post-acute sequela of COVID and patients with ischemic heart diseases (IHD). The IHD

patients underwent ferumoxytol enhancement to mimic increased iron content in the myocardium, and the T_2* values outside the normal native range were correctly measured using the proposed technique.

CHAPTER 5 presented a novel reconstruction approach based on low-rank tensor constraints. In previous MR Multitasking implementations, we utilized training data for temporal subspace estimation, which was followed by recovering the spatial coefficients using the fixed temporal subspace. This could potentially lead to subspace bias and compromise reconstruction performance. Therefore, we proposed a new reconstruction approach which utilized the entire k-t dataset acquired for estimating temporal and spatial components. Compared to the previous approach, the proposed technique showed better precision and repeatability in numerical simulations and in in-vivo studies and showed comparable or better performance with a shortened scan time.

6.2 Future Clinical Directions

6.2.1 Potential applications of fat imaging

6.2.1.1 Preliminary clinical results

$N = 4$ consented patients that were identified with pre-HFpEF (heart failure with preserved ejection fraction) were recruited and scanned on a 3T scanner (MAGNETOM Vida, Siemens Healthineers, Erlangen, Germany) with a standard 18-channel body coil and an integrated spine matrix coil. The VTR Multitasking technique developed in CHAPTER 4 was scanned in the mid-ventricular slice with short-axis view. A free-breathing 1[H]-MRS was also scanned in the septum region of myocardium for triglyceride content.

The fat-water ratio from different techniques were analyzed using Bland-Altman plot and are shown in Figure 6.1(A). The limits of agreement between our technique (based on Dixon) and

MRS is 1.5%, which is very close to the findings (2%) of a previous study (213). Paired t-tests indicate no significant difference between the measurements from different approaches.

The preliminary evaluations of fat imaging showed initial agreement of our proposed approach with the gold standard. Moreover, it also established the limits, which indicated any fat differences smaller than 1.5% cannot be detected with our technique. In this specific patient cohort, the alterations in fat water ratio were smaller than 0.5%, which was beyond the sensitivity and precision of our technique.

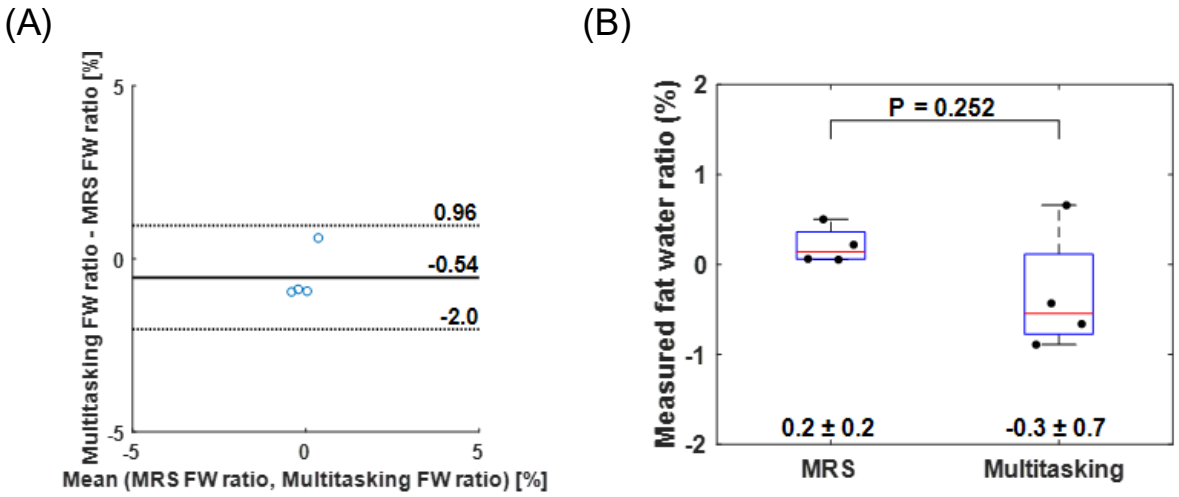

Figure 6.1: (A) Bland-Altman plot of measured fat-water ratio from MRS and developed MR Multitasking technique. (B) The distribution of measured fat-water ratio. FW: fat-water.

6.2.1.2 Potential applications

Although Dixon type of techniques may have limited precision for identifying pre-HFpEF patients, there have been emerging studies associating epicardial adipose tissues (EAT) and pericardial adipose tissues (PAT) with adverse cardiovascular phenotypes. Chahine et. al (214) found a significant correlation between EAT volume and fibrosis in the left atrium (assessed using late-gadolinium enhancement). Ng et. al (213) found EAT volume was independently associated with interstitial myocardial fibrosis and global strain of left ventricle. Another study (215)

involving 42598 UK biobank participants found an independent association between higher PAT and poorer left ventricular function, mass, and great wall thickness. Those studies typically utilized a Dixon sequence for water-fat separation and segments and measures the adipose tissue volume, where the information needed are also available with the developed VTR Multitasking technique. The EAT and PAT could be potential targets of the developed technique, and further development should be focused on increasing the spatial coverage and scanning efficiency.

6.2.2 Patients with arrhythmia

6.2.2.1 Preliminary results

Although MR Multitasking may provide a solution to patients with arrhythmia, so far there have been limited evaluations on this cohort. An 86-year-old consented patient (male) with recurring premature ventricular contractions (PVC) and type-2 diabetes was imaged on a 3T scanner (MAGNETOM Skyra, Siemens Healthineers, Erlangen, Germany) with a standard 18-channel body coil and an integrated spine matrix coil following gadolinium enhancement. High burden was found on this patient with ECG monitoring (36.8%). MOLLI images with ECG gating were collected for T_1 mapping with short-axis view, and the proposed VTR Multitasking technique was collected with long axis view.

The parametric maps from MOLLI and from VTR Multitasking are shown in Figure 6.2. The MOLLI technique seemed to have failed to provide a T_1 map, which may be related to mismatched cardiac phases across the contrast weighted images. In contrast, Multitasking seemed to give reasonable results which had less motion artifacts. The adipose tissues seen on the FF map appeared to match with the patient information (type-2 diabetes). Previous literatures (216, 217) have pointed out the potential associations between cardiac adiposity and cardiovascular events and arrhythmia. This seemed to be aligned with the adipose tissue around epicardial regions and

atrial regions in the FF map as well. Despite the promising results, there is still a lack of direct and convincing evidence regarding the utility of the developed technique on this patient cohort. At this stage, further clinical evaluations are required.

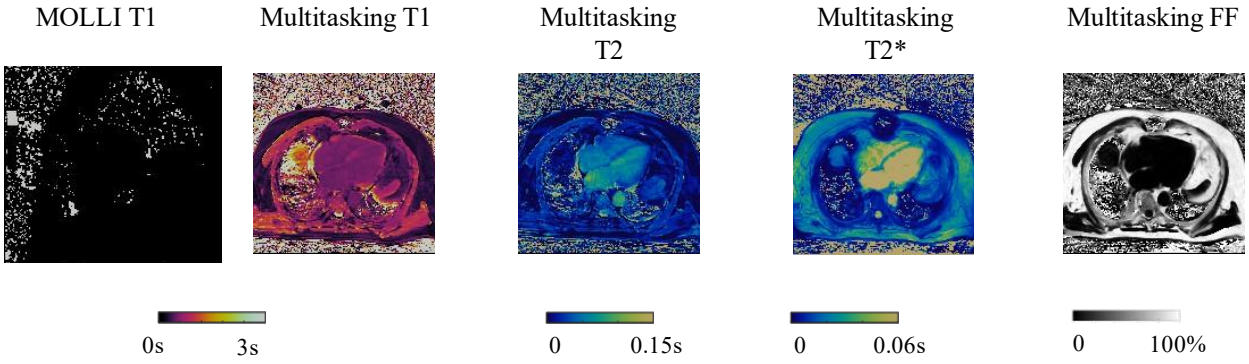

Figure 6.2: The MOLLI and Multitasking results on a PVC patient.

6.2.2.2 Potential ways of validation

ECG-gated techniques, such as MOLLI, may fail in an arrhythmia patient. Therefore, it is challenging to employ these conventional techniques as references and other baselines should be considered. One potential option would be a motion phantom similar to the linear motion stage used in CHAPTER 4. However, it must go beyond the translational motion to be able to generate cardiac motion patterns. Then the phantom can be filled with certain solutions and be programmed to mimic arrythmia. Finally, image acquisition can be performed without motion as the reference and with motion for testing.

Another option is to create an animal model of arrythmia, as described in (218). The Multitasking and conventional ECG-gated references can be acquired for those animals, after which the animals will be terminated for ex-vivo imaging. Finally, Multitasking measurements will be compared with ex-vivo measurements.

6.3 Future Technical Developments

6.3.1 Towards mid-field and/or low-field quantitative imaging

6.3.1.1 Background

To date, the practice of MR Multitasking has been limited to 3T. However, scanner availability of a particular field strength could be limited in real-life scenarios. In the meantime, while cardiovascular MR is increasing being conducted on 3T scanners, 1.5T scanners remain the mainstream for clinical studies. It is therefore important to consider how MR Multitasking can be applied to lower field strengths.

The collected MRI signal is proportional to the external magnetic field. Therefore, one of the primary challenges for low-field MRI is the reduced SNR. For example, with the same sequence, image SNR at 1.5T will be half of that at 3T. On the other side, low field scanners are also advantageous (219) in cost, specific absorption rate (SAR) limits and B0 and B1 field homogeneities.

One potential approach to take advantage of the benefits at low field while alleviating the SNR issues is to use bSSFP readouts. Compared to GRE readouts, bSSFP utilizes balanced gradients and doesn't spoil the transverse magnetization, which is later refocused and therefore produces higher signal. It must be noted that bSSFP has high demand for B0 field homogeneity, and usually leads to high SAR because of short T_R and large flip angles. However, those won't be fundamental challenges at low field, as mentioned above.

6.3.1.2 Methods

Figure 6.3 shows the prototyping sequence diagram for an bSSFP Multitasking sequence. Catalyzation pulses are used before data acquisition to minimize signal oscillations. There are many options available for catalyzation pulses (220). Through preliminary testing, we found

Kaiser-Bessel ramp worked well with 15 ramp-up pulses and $\beta = 3$ for radial trajectories. Therefore, this setup was adopted throughout the following experiments.

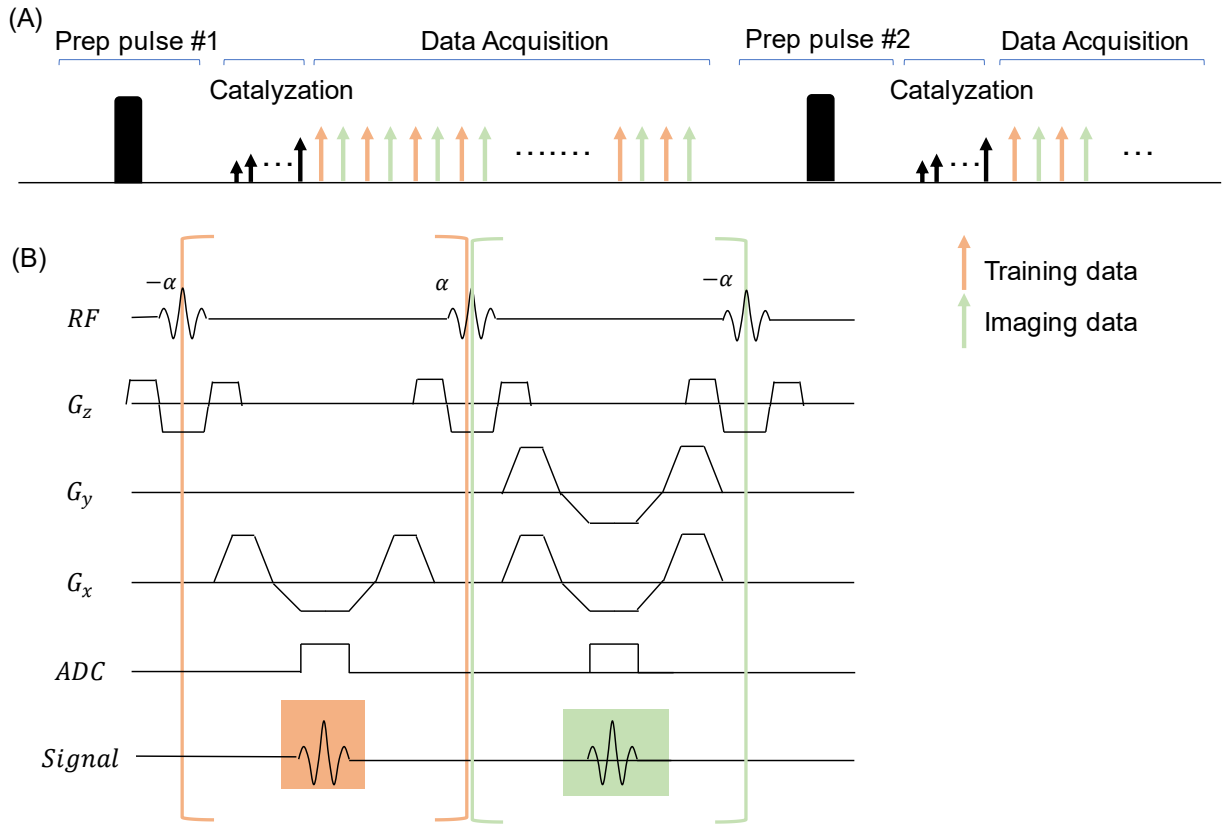

Figure 6.3: (A) A prototyping MR Multitasking sequence integrating bSSFP readouts. Every time before the acquisition starts, catalyzation pulses are played to minimize signal oscillations (B) Both training and imaging data are now acquired with bSSFP readouts and imaging data is collected using golden angle radial trajectory.

A Cramer-Rau bound analysis was performed with typical tissue and system parameters at 1.5T (T_1 = 1000 ms, T_2 = 50 ms, inversion efficiency = 0.9, $\Delta B_0 = 20$Hz) to assess theoretical performance of GRE Multitasking and bSSFP Multitasking. The simulated sequence cycled through hybrid T_2IR modules with preparation times = 0, 30, 40, 50, 60 ms and the analysis was performed for flip angles ranging from 2° to 50°. The repetition time $T_R = 3.6$ ms and recovery period was around 2765 ms. The T_1 and T_2 precision were calculated from the inverse of resulting Fisher information matrix, and NRMSE was calculated based on the following definition:

$$NRMSE = \sqrt{\frac{\frac{\sigma_{T1}^2}{T1^2} + \frac{\sigma_{T2}^2}{T2^2}}{2}}, \tag{6.1}$$

where σ_{T1} and σ_{T2} correspond to T_1 and T_2 precision.

The bSSFP Multitasking T_1/T_2 mapping sequence was implemented based on Figure 6.3 with repetition time $T_R = 3.6$ ms, flip angle $= 12°$, recovery period ≈ 2765 ms, and T_2 preparation time = 0, 30, 40, 50, 60 ms. Two consented volunteers were scanned on a 1.5T scanner (MAGNETOM Avanto, Siemens Healthineers, Erlangen, Germany) with a standard body coil and an integrated spine matrix coil. The scan time was 1.5 min.

A new signal dictionary was generated for bSSFP readouts using Bloch equations for different T_1/T_2 combinations. The other parts of reconstruction were kept the same as in GRE Multitasking (60). Since it is hard to derive an analytical equation for the underlying signal, a dictionary fitting strategy (221) was used for parametric mapping. The fitting dictionary was generated for different T_1/T_2/inversion efficiency combinations and were designed based on typical physiological and system limits of cardiac imaging: T_1 values were taken as between 50 ms to 3000 ms (with an increment of 10 ms below 100 ms, an increment of 20 ms from 100 ms to 1200 ms, an increment of 40 ms from 1200 ms to 1800 ms, and an increment of 100 ms above 1800 ms); T_2 values ranged from 5 ms to 600 ms (with an increment of 2 ms below 60 ms, an increment of 5 ms from 60 ms to 100 ms, an increment of 10 ms from 100 ms to 300 ms, and an increment of 50 ms above 300 ms); inversion efficiency ranged from 0.5 to 1 (with an increment of 0.05 below 0.75, an increment of 0.02 above 0.75). Inversion efficiency of 1 means perfect inversion. To further reduce computational cost and memory constraints, the generated dictionary was compressed using principal component analysis (21) and dictionary matching was performed in the compressed domain. To be specific, let $\mathbf{D} \in \mathbb{C}^{N \times T}$ denote the simulated dictionary with N entries and T time

points. An SVD was performed on $\mathbf{D}$ to find the best temporal basis $\mathbf{V} \in \mathbb{C}^{T\times L}$ ($L \ll T$ and L was set to be 100 in this work). Then the best matched dictionary entry i for voxel r was found by:

$$i = arg\max_i \langle I(r)\mathbf{V}, \mathbf{D}_i\mathbf{V}\rangle, \tag{6.2}$$

where $I(r)$ are the reconstructed signal at voxel r and $\langle\cdot\rangle$ denotes vector inner product.

6.3.1.3 Results

Figure 6.4 shows the results for Cramer Rau bound analysis. The comparison shows the theoretical superiority of bSSFP Multitasking over GRE Multitasking, leading to about 40% difference in 1/NRMSE. The plot also indicates bSSFP Multitasking may need much larger flip angles than the GRE version, which is around 28 degrees for optimal performance.

Figure 6.5 shows myocardial T_1 and T_2 maps for two healthy volunteers with bSSFP Multitasking sequences. The average myocardial T_1 values were 965.8 ms for subject 1 and 975.3 ms for subject 2. The average myocardial T_2 values were 46.6 ms for subject 1 and 42.6 ms for subject 2.

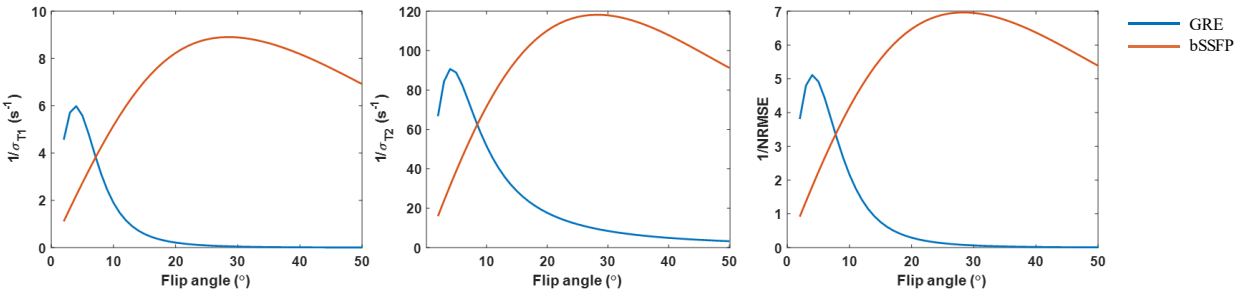

Figure 6.4: Cramer Rau bound analysis for GRE Multitasking and bSSFP Multitasking for a range of flip angles.

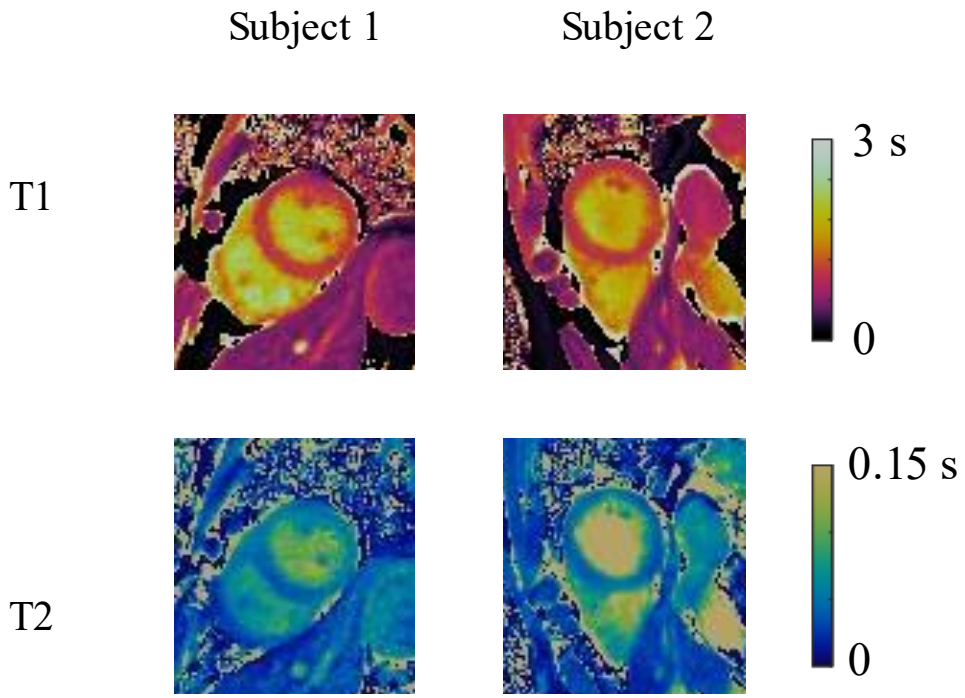

Figure 6.5: T_1 and T_2 maps from bSSFP Multitasking on two healthy volunteers.

6.3.1.4 Discussions

The translation of MR Multitasking to lower field strengths would enhance the accessibility and portability of the technique. One of the key technical challenges at low field would be SNR penalty, and we proposed to address this challenge using a bSSFP readout. The numerical simulations indicate the benefit of bSSFP Multitasking over the GRE version at 1.5T in terms of precision. The simulation was performed without considering the B1 confounding effects. As mentioned before, B1 field inhomogeneity would be less of an issue at 1.5T, so the assumption should be overall valid. Moving forward, it would be interesting to consider the unknown B1 effects and perform comparison again in the context of using two flip angles for B1+ mapping.

The in-vivo study on two healthy volunteers showed reasonable image quality and quantitative measurements which close to previous literature values at 1.5T (222, 223). This demonstrated initial feasibility, even with a sub-optimal flip angle of 12°. Based on the numerical simulation,

the precision of T_1 and T_2 can be potentially enhanced by a factor of 2 from flip angle of 12° to 28° (the optimal flip angle in theory). Further validations utilizing better flip angle choices will be needed against the conventional references and in-vivo comparison should be performed with GRE Multitasking on T_1/T_2 precision.

6.3.2 Towards navigator-free MR Multitasking

6.3.2.1 Background

MR Multitasking collects training data (navigator data) and imaging data in an interleaved way. The training data can be seen as a fully-sampled, low-resolution surrogate, which allows fast extraction of temporal basis functions and recovery of spatial coefficients with that fixed temporal subspace. There are certain limitations associated with the acquisition and utilization of training data: 1) A significant portion of the scan is spent on training data acquisition, which gives little spatial information and compromises imaging efficiency; 2) The temporal subspace estimated from training data can be sub-optimal, as demonstrated and improved in CHAPTER 5; 3) A dedicated sequence implementation is needed to alternate between the datasets, which may add complexity to deployment of MR Multitasking and compromise its portability.

To overcome the limitations associated with training data, we took some preliminary steps in developing a "navigator-free" version of MR Multitasking for T_1 and T_2 mapping. The primary technical challenges include: 1) to reconstruct the "realtime" (ungated) images without prior knowledge of realtime temporal subspace 2) to recover the underlying tensor without knowledge of temporal matrices and the core tensor. The approaches we used to tackle these challenges will be described in the next section.

6.3.2.2 Methods

Figure 6.6: (A) A prototyping MR Multitasking sequence dedicated to imaging data collection (B) The imaging data are collected using tiny golden angle radial trajectory. Figure 6.6 shows the sequence diagram used in this work, which removes all the training data collection. The imaging data are collected using tiny golden angle trajectories (7^{th} order). The imaging protocol can be found in Table 6.1.

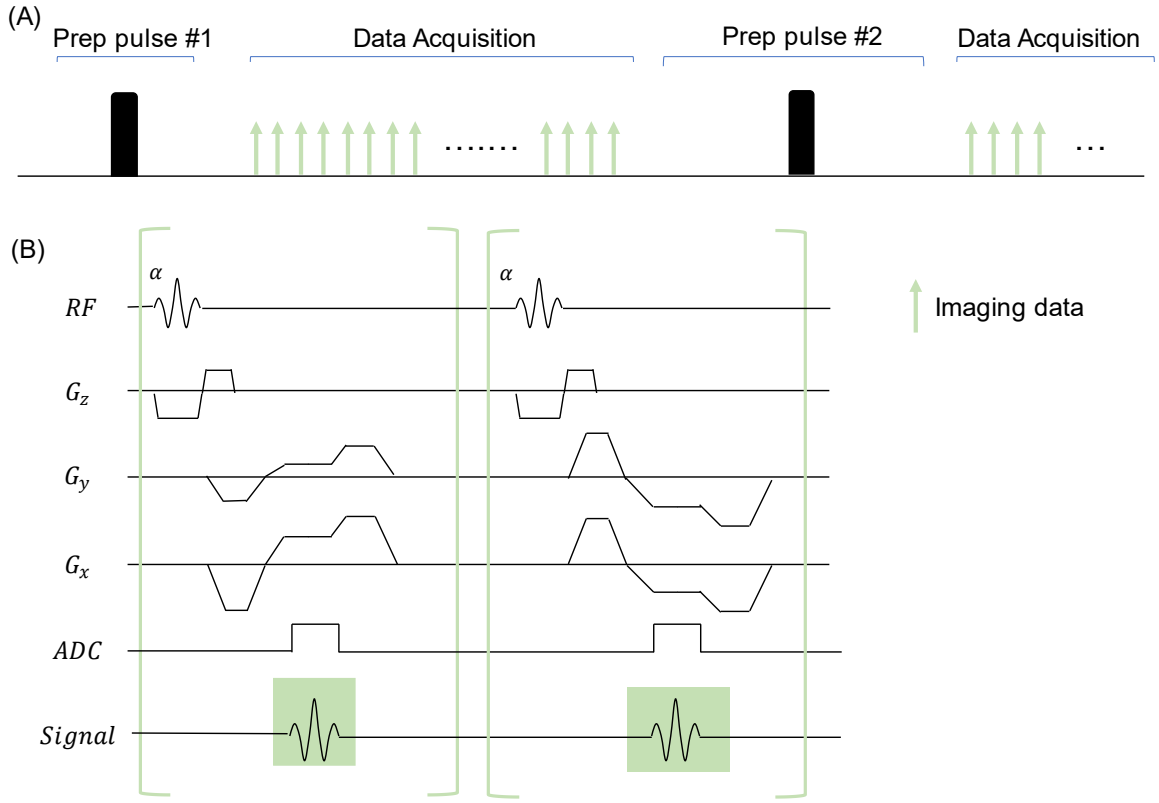

Figure 6.6: (A) A prototyping MR Multitasking sequence dedicated to imaging data collection (B) The imaging data are collected using tiny golden angle radial trajectory.

Table 6.1: Sequence parameters used. The FOV and matrix size includes 2-fold oversampling. BW: bandwidth.

FOV (mm^2)	540 × 540	**Slice thickness (mm)**	8
Matrix size	320 × 320	**Resolution (mm)**	1.7 × 1.7

TE (ms)	1.6	**TR (ms)**	3.6
Number of readouts per shot	720	**Recovery period (s)**	2.6
T_2IR prep durations (ms)	0, 30, 40, 50, 60	**Pixel BW (Hz/pixel)**	1008
Flip angle (°)	5	**Acquisition time (s)**	90
Trajectory	Tiny golden angle (7th order)		

In the first step of reconstruction, we aimed to recover realtime (ungated) images for binning. This was done by solving the following low-rank matrix reconstruction problem:

$$\widehat{\mathbf{X}} = \arg\min_{\substack{\mathbf{X} \\ \mathbf{X}=\mathbf{U}\boldsymbol{\Phi}}} \|\mathbf{d} - \Omega\mathbf{F}\mathbf{S}\mathbf{X}\|_2^2, \tag{6.3}$$

where $\mathbf{X} \in \mathbb{C}^{N\times T}$ are the ungated image series, $\mathbf{F}$ denotes Fourier transform, $\mathbf{S}$ denotes sensitivity maps, Ω is the undersampling mask, N is the number of voxels, and T is total number of realtime points. The optimization problem in Equation (6.3) is non-convex and is equivalent to:

$$\widehat{\mathbf{U}}, \widehat{\boldsymbol{\Phi}} = \arg\min_{\mathbf{U},\boldsymbol{\Phi}} \|\mathbf{d} - \Omega\mathbf{F}\mathbf{S}\mathbf{U}\boldsymbol{\Phi}\|_2^2, \tag{6.4}$$

where $\boldsymbol{\Phi} \in \mathbb{C}^{L_{rt}\times T}$ are the realtime temporal basis functions and $\mathbf{U} \in \mathbb{C}^{N\times L_{rt}}$ are the spatial coefficients. In this work, we set $L_{rt} = 24$ and solved Equation (6.4) combining incremented rank power factorization (IRPF) (224) and sliding window reconstruction (with a temporal resolution of 50 ms). The IRPF algorithm initializes $\mathbf{U}$ and $\boldsymbol{\Phi}$ with random rank-1 matrices (vectors) and alternatively solves for $\mathbf{U}$ and $\boldsymbol{\Phi}$ by fixing the other variable in Equation (6.4). It then increments the rank for $\mathbf{U}$ and $\boldsymbol{\Phi}$ and repeats the process. The incrementing process stops after L_{rt} is reached.

Once ungated images were reconstructed, we employed the same strategy as in the previous publication (60) for respiratory and cardiac binning.

In the final step, we performed tensor reconstruction for the underlying image series $\mathcal{X}$. We 1) obtained T_1/T_2 basis $\widehat{\mathbf{U}}_{T_1}$ and $\widehat{\mathbf{U}}_{T_2}$ from a pre-simulated dictionary; 2) aggregated the completed training tensor $\widehat{\mathcal{D}}_{tr}$ from 3 historical datasets with training dataset acquisition and performed HOSVD on it for initialization of the core tensor $\mathcal{G}$, cardiac motion basis $\mathbf{U}_c$, and respiratory motion basis $\mathbf{U}_r$; 3) solved the following optimization problem using the alternating strategy developed in CHAPTER 5:

$$\hat{\mathcal{G}}, \widehat{\mathbf{U}}_x, \widehat{\mathbf{U}}_c, \widehat{\mathbf{U}}_r = \arg\min_{\mathcal{G}, \mathbf{U}_x, \mathbf{U}_c, \mathbf{U}_r} \left\| \mathbf{d}_{img} - \Omega\left(\mathbf{F}\mathbf{S}\mathbf{U}_x \mathcal{M}(\mathcal{G} \times_2 \mathbf{U}_c \times_3 \mathbf{U}_r \times_4 \widehat{\mathbf{U}}_{T_1} \times_5 \widehat{\mathbf{U}}_{T_2})\right)\right\|_2^2 + \lambda_1 \|\mathrm{vec}(\mathbf{W}\mathbf{U}_x)\|_1 + \lambda_2 \|\mathrm{vec}(\mathcal{G})\|_1, s.t.\ \mathbf{U}_c^H \mathbf{U}_c = \mathbf{I} \text{ and } \mathbf{U}_r^H \mathbf{U}_r = \mathbf{I}. \quad (6.5)$$

Note Equation (6.5) only involved imaging data, as no training dataset were acquired.

A numerical phantom was created from the XCAT phantom (209) with 20 cardiac phases ($N_2 = 20$) and 6 respiratory phases ($N_3 = 6$). The average heart rate and respiration rate were set to be 75 bpm and 15 bpm, respectively, with 10% standard deviation. Typical T_1/T_2 values at 3T were assigned to different tissue types. The sequence diagram and acquisition scheme as in Figure 6.6 was used to simulate k-space data. The imaging protocol shown in Table 6.1 was used for simulation. For comparison purposes, we also simulated k-space data for the conventional MR Multitasking setup with training data. A comparable noise level to the in-vivo study was added to both cases.

We employed the reconstruction workflow mentioned above for navigator-free MR Multitasking and utilized the joint update approach described in CHAPTER 5 for conventional MR Multitasking. To evaluate the effects of the described realtime reconstruction approach and motion binning on parametric maps, the navigator-free MR Multitasking was also reconstructed

using gold standard motion bins and the results were used for comparison. To evaluate the effects of reduced scan time, the navigator-free MR Multitasking was reconstructed at two scan times (90 s and 50 s).

The reconstructed images at the end-expiration and end-diastolic phase were then fitted to get the T_1 and T_2 maps. The RMSE between the ground truth and the reconstructed maps, as defined in Equation (5.27), were used as the evaluation metric for the entire image and for the myocardium region.

6.3.2.3 Results

Figure 6.7 shows the reconstructed T_1 and T_2 from navigator-free MR Multitasking in a 90-s scan. Compared to the reconstruction with gold standard motion bins, the errors of T_1 and T_2 maps from estimated motion bins using the described strategy were slightly higher but overall comparable. As shown in Figure 6.8, when compared to the conventional Multitasking that acquires training data, the navigator-free version showed lower image RMSE for both T_1 and T_2 maps within both 90-s scan time and 50-s scan time. The T_1 RMSE in the myocardium from navigator-free Multitasking were slightly larger than that of conventional Multitasking, but T_2 RMSE in the myocardium were slightly lower. This was also observed for both scan times.

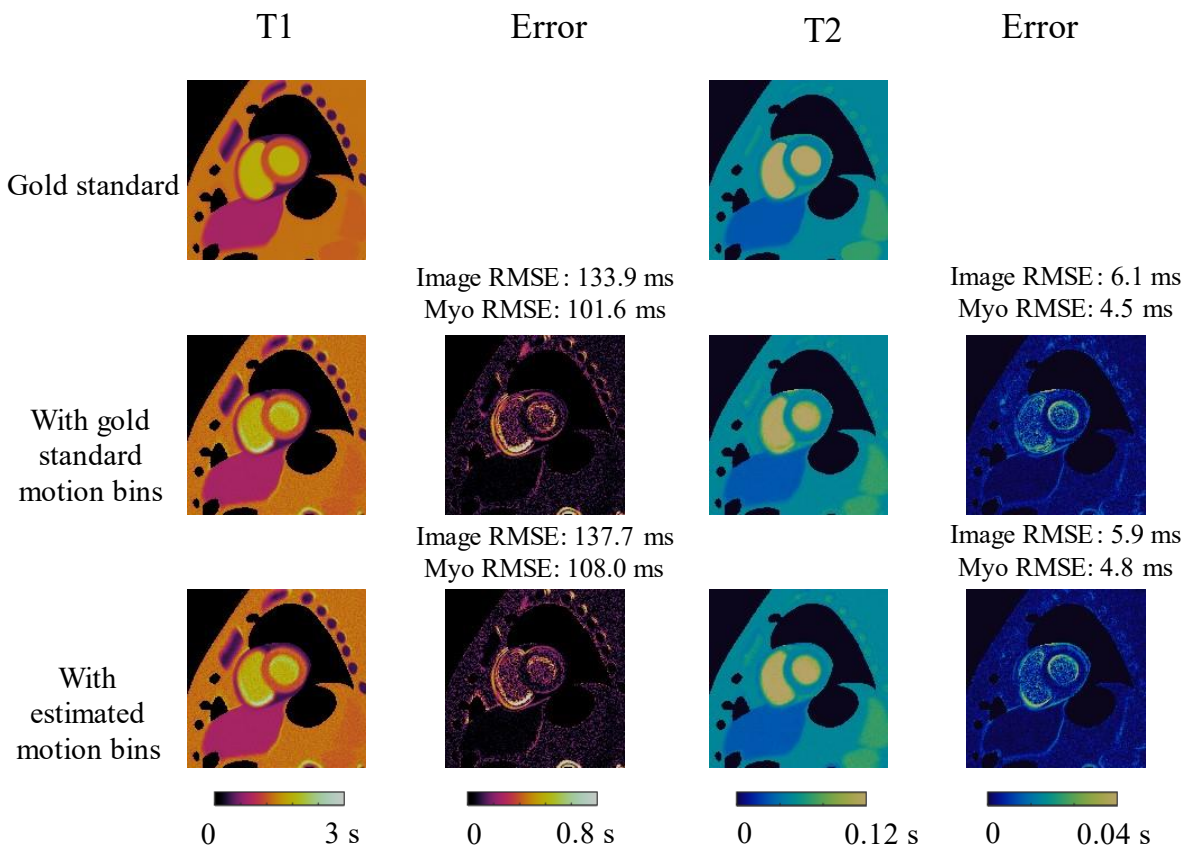

Figure 6.7: The reconstructed T_1 and T_2 maps of navigator-free MR Multitasking using gold standard motion bins and estimated motion bins in the numerical simulation. The performance was overall comparable. Myo: myocardium.

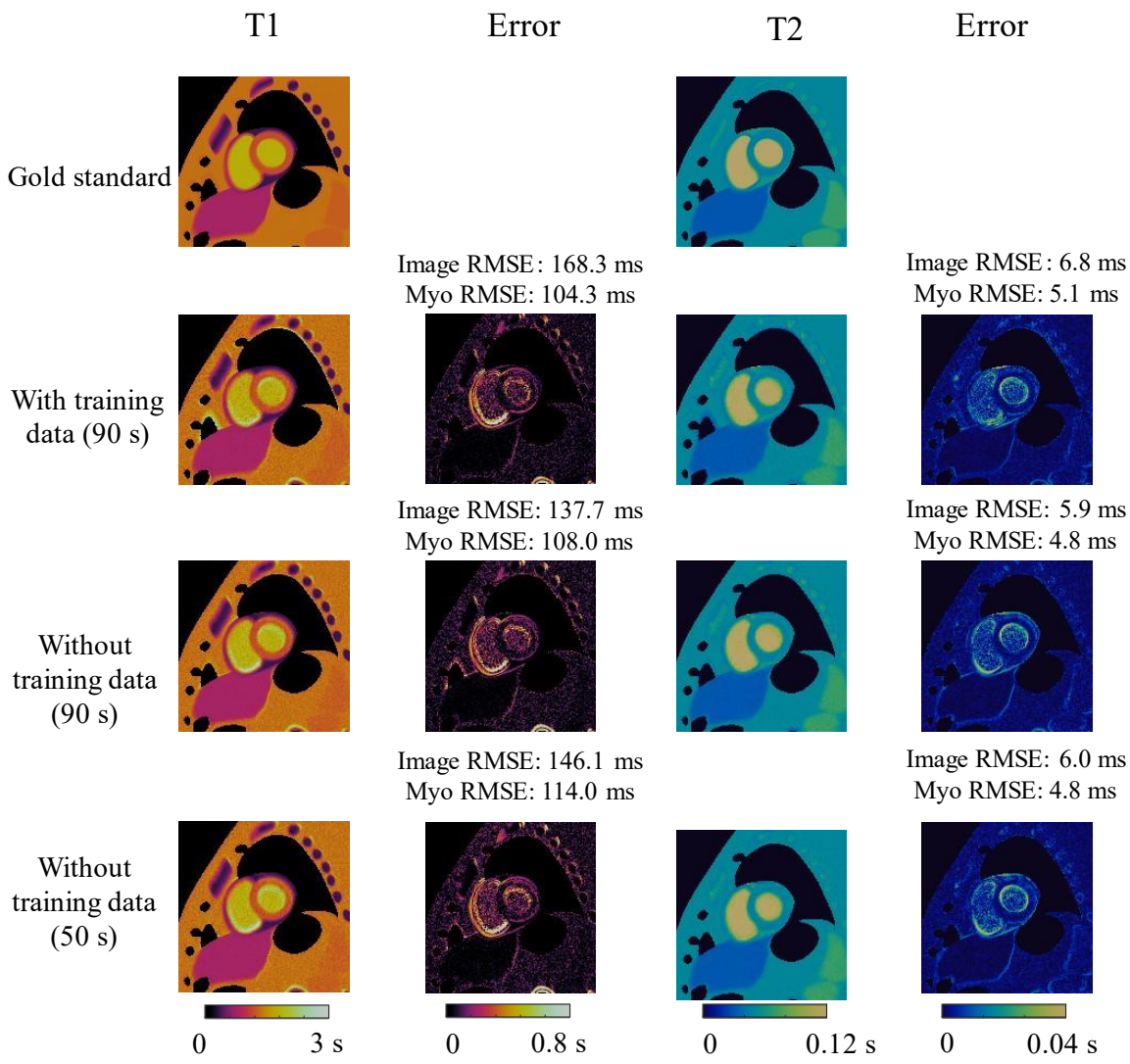

Figure 6.8: The reconstructed T_1 and T_2 maps of MR Multitasking with and without training data acquisition in the numerical simulation. The T_1 and T_2 maps from the version without training data, even truncated, consistently show better image RMSE than the one with training data. Myo: myocardium.

6.3.2.4 Discussion

In cardiovascular MR Multitasking, training data are typically collected every other imaging data readout, meaning 50% of the scan time is spent on collecting training data. This compromises acquisition efficiency as training data provide little spatial information. The dedicated sequence implementation which alternates between training and imaging data acquisition also limits the

portability of MR Multitasking. In this work, we presented preliminary efforts to remove the training data to overcome these limitations. The improved imaging efficiency can be used for reducing scan time or trading for better quantitative performance.

There are two underlying challenges which were addressed in this work: 1) to reconstruct decent realtime images for motion binning; 2) to reconstruct underlying high-dimensional tensor. We evaluated our solution to 1) by performing the reconstruction with gold standard motion bins of the simulation and using those results as a baseline. The findings indicated the imperfections of our proposed realtime reconstruction strategy didn't compromise the T_1 and T_2 maps to a large extent. Our overall solution was evaluated with the comparison between navigator-free Multitasking and conventional Multitasking, which showed superior performance of the navigator-free version in the entire image and its potential for scan time reduction. However, it remained to be further explored whether the myocardial quantification was improved.

In the next step, in-vivo experiments should be performed to validate the technique against conventional references including MOLLI and T_2prep FLASH. And in-vivo comparison needs to be performed between Multitasking with and without training data acquisition in terms of precision and repeatability in the myocardium.

6.4 Final thoughts

Over the past decade, the field of quantitative, multiparametric MRI has witnessed significant growth and innovation in technical development. Breakthroughs such as MR fingerprinting and MR Multitasking are promising to achieve comprehensive tissue characterization with minimal human intervention, improved patient comfort and clinically feasible scan times. These advancements may bring exciting transformation in the way clinical scans are performed and decisions are made. As I look ahead, further developments remain crucial to fully realize the

potential of multiparametric MRI. Improving efficiency, performance metrics (precision, repeatability, reproducibility), resolution, coverage, and ease of use (reconstruction time, computational cost) are essential areas of focus for MR Multitasking. Meanwhile, universal challenges persist concerning the variability of measurements, spanning different magnetic field strengths, imaging sequences, scanner models, and vendors. The intricacies of relaxation times and other parameters introduce complexities in directly comparing quantitative values across diverse settings, necessitating the establishment of "institutional references" for healthy volunteers at each site and potentially on each scanner. This can impede the seamless translation of clinical findings into actionable diagnoses. Harmonizing and standardizing these techniques and establishing cross-technique equivalences are therefore essential to ensure consistent and clinically meaningful quantitative information. Comprehensive clinical evaluations will continue to play a vital role in assessing and refining these techniques. With continued dedication and joint efforts, I envision a future where these techniques will contribute significantly to improving patient care, enhancing disease diagnosis, and advancing medical knowledge.

BIBLIOGRAPHY

1. Bull S, White SK, Piechnik SK, Flett AS, Ferreira VM, Loudon M, et al. Human non-contrast T1 values and correlation with histology in diffuse fibrosis. Heart. 2013;99(13):932-7.

2. Schelbert EB, Messroghli DR. State of the Art: Clinical Applications of Cardiac T1 Mapping. Radiology. 2016;278(3):658-76.

3. Ugander M, Bagi PS, Oki AJ, Chen B, Hsu LY, Aletras AH, et al. Myocardial Edema as Detected by Pre-Contrast T1 and T2 CMR Delineates Area at Risk Associated With Acute Myocardial Infarction. Jacc-Cardiovasc Imag. 2012;5(6):596-603.

4. Messroghli DR, Walters K, Plein S, Sparrow P, Friedrich MG, Ridgway JP, et al. Myocardial T-1 mapping: Application to patients with acute and chronic myocardial infarction. Magn Reson Med. 2007;58(1):34-40.

5. Verhaert D, Thavendiranathan P, Giri S, Mihai G, Rajagopalan S, Simonetti OP, et al. Direct T2 Quantification of Myocardial Edema in Acute Ischemic Injury. Jacc-Cardiovasc Imag. 2011;4(3):269-78.

6. Triadyaksa P, Oudkerk M, Sijens PE. Cardiac T2 * mapping: Techniques and clinical applications. J Magn Reson Imaging. 2020;52(5):1340-51.

7. Langkammer C, Liu T, Khalil M, Enzinger C, Jehna M, Fuchs S, et al. Quantitative Susceptibility Mapping in Multiple Sclerosis. Radiology. 2013;267(2):551-9.

8. Langkammer C, Pirpamer L, Seiler S, Deistung A, Schweser F, Franthal S, et al. Quantitative Susceptibility Mapping in Parkinson's Disease. Plos One. 2016;11(9).

9. Deistung A, Schweser F, Wiestler B, Abello M, Roethke M, Sahm F, et al. Quantitative Susceptibility Mapping Differentiates between Blood Depositions and Calcifications in Patients with Glioblastoma. Plos One. 2013;8(3).

10. Kellman P, Hernando D, Arai AE. Myocardial Fat Imaging. Curr Cardiovasc Imaging Rep. 2010;3(2):83-91.

11. Du G, Lewis MM, Styner M, Shaffer ML, Sen S, Yang QX, et al. Combined R2* and diffusion tensor imaging changes in the substantia nigra in Parkinson's disease. Mov Disord. 2011;26(9):1627-32.

12. Ma S, Wang N, Fan ZY, Kaisey M, Sicotte NL, Christodoulou AG, et al. Three-dimensional whole-brain simultaneous T1, T2, and T1 rho quantification using MR Multitasking: Method and initial clinical experience in tissue characterization of multiple sclerosis. Magn Reson Med. 2021;85(4):1938-52.

13. Dolan RS, Rahsepar AA, Blaisdell J, Suwa K, Ghafourian K, Wilcox JE, et al. Multiparametric Cardiac Magnetic Resonance Imaging Can Detect Acute Cardiac Allograft Rejection After Heart Transplantation. JACC Cardiovasc Imaging. 2019;12(8 Pt 2):1632-41.

14. Godenschweger F, Kagebein U, Stucht D, Yarach U, Sciarra A, Yakupov R, et al. Motion correction in MRI of the brain. Phys Med Biol. 2016;61(5):R32-R56.

15. Chen Y, Liu S, Wang Y, Kang Y, Haacke EM. STrategically Acquired Gradient Echo (STAGE) imaging, part I: Creating enhanced T1 contrast and standardized susceptibility weighted imaging and quantitative susceptibility mapping. Magn Reson Imaging. 2018;46:130-9.

16. Haacke EM, Chen Y, Utriainen D, Wu B, Wang Y, Xia S, et al. STrategically Acquired Gradient Echo (STAGE) imaging, part III: Technical advances and clinical applications of a rapid multi-contrast multi-parametric brain imaging method. Magn Reson Imaging. 2019;65:15-26.

17. Wang Y, Chen Y, Wu D, Wang Y, Sethi SK, Yang G, et al. STrategically Acquired Gradient Echo (STAGE) imaging, part II: Correcting for RF inhomogeneities in estimating T1 and proton density. Magn Reson Imaging. 2018;46:140-50.

18. Metere R, Kober T, Moller HE, Schafer A. Simultaneous Quantitative MRI Mapping of T1, T2* and Magnetic Susceptibility with Multi-Echo MP2RAGE. Plos One. 2017;12(1):e0169265.

19. Sun HF, Cleary JO, Glarin R, Kolbe SC, Ordidge RJ, Moffat BA, et al. Extracting more for less: multi-echo MP2RAGE for simultaneous T-1-weighted imaging, T-1 mapping, R2*mapping, SWI, and QSM from a single acquisition. Magn Reson Med. 2020;83(4):1178-91.

20. Caan MW, Bazin PL, Marques JP, de Hollander G, Dumoulin SO, van der Zwaag W. MP2RAGEME: T1, T2*, and QSM mapping in one sequence at 7 tesla. Human brain mapping. 2019;40(6):1786-98.

21. Jaubert O, Cruz G, Bustin A, Schneider T, Lavin B, Koken P, et al. Water-fat Dixon cardiac magnetic resonance fingerprinting. Magn Reson Med. 2020;83(6):2107-23.

22. Guo R, Chen Z, Wang Y, Herzka DA, Luo J, Ding H. Three-dimensional free breathing whole heart cardiovascular magnetic resonance T1 mapping at 3 T. J Cardiovasc Magn Reson. 2018;20(1):64.

23. van Heeswijk RB, Feliciano H, Bongard C, Bonanno G, Coppo S, Lauriers N, et al. Free-breathing 3 T magnetic resonance T2-mapping of the heart. JACC Cardiovasc Imaging. 2012;5(12):1231-9.

24. Christodoulou AG, Shaw JL, Nguyen C, Yang Q, Xie YB, Wang N, et al. Magnetic resonance multitasking for motion-resolved quantitative cardiovascular imaging. Nat Biomed Eng. 2018;2(4):215-26.

25. Ma S, Nguyen CT, Han F, Wang N, Deng Z, Binesh N, et al. Three-dimensional simultaneous brain T1 , T2 , and ADC mapping with MR Multitasking. Magn Reson Med. 2020;84(1):72-88.

26. Wang N, Gaddam S, Wang LX, Xie YB, Fan ZY, Yang WS, et al. Six-dimensional quantitative DCE MR Multitasking of the entire abdomen: Method and application to pancreatic ductal adenocarcinoma. Magn Reson Med. 2020;84(2):928-42.

27. Bottomley PA, Foster TH, Argersinger RE, Pfeifer LM. temperature, species, excision, and age. Medical Physics. 1984;11(4):4.

28. Rooney WD, Johnson G, Li X, Cohen ER, Kim SG, Ugurbil K, et al. Magnetic field and tissue dependencies of human brain longitudinal 1H2O relaxation in vivo. Magnetic Resonance in Medicine: An Official Journal of the International Society for Magnetic Resonance in Medicine. 2007;57(2):308-18.

29. Messroghli DR, Radjenovic A, Kozerke S, Higgins DM, Sivananthan MU, Ridgway JP. Modified Look‐Locker inversion recovery (MOLLI) for high‐resolution T1 mapping of the heart. Magnetic Resonance in Medicine: An Official Journal of the International Society for Magnetic Resonance in Medicine. 2004;52(1):141-6.

30. Chow K, Flewitt JA, Green JD, Pagano JJ, Friedrich MG, Thompson RB. Saturation recovery single‐shot acquisition (SASHA) for myocardial T1 mapping. Magnet Reson Med. 2014;71(6):2082-95.

31. Blüml S, Schad LR, Stepanow B, Lorenz WJ. Spin‐lattice relaxation time measurement by means of a TurboFLASH technique. Magnet Reson Med. 1993;30(3):289-95.

32. Wang Y, Liu T. Quantitative susceptibility mapping (QSM): Decoding MRI data for a tissue magnetic biomarker. Magn Reson Med. 2015;73(1):82-101.

33. Haacke EM, Liu S, Buch S, Zheng W, Wu D, Ye Y. Quantitative susceptibility mapping: current status and future directions. Magn Reson Imaging. 2015;33(1):1-25.

34. Reeder SB, Cruite I, Hamilton G, Sirlin CB. Quantitative assessment of liver fat with magnetic resonance imaging and spectroscopy. Journal of magnetic resonance imaging. 2011;34(4):729-49.

35. Bonkovsky HL, Jawaid Q, Tortorelli K, LeClair P, Cobb J, Lambrecht RW, et al. Non-alcoholic steatohepatitis and iron: increased prevalence of mutations of the HFE gene in non-alcoholic steatohepatitis. Journal of hepatology. 1999;31(3):421-9.

36. George DK, Goldwurm S, Macdonald GA, Cowley LL, Walker NI, Ward PJ, et al. Increased hepatic iron concentration in nonalcoholic steatohepatitis is associated with increased fibrosis. Gastroenterology. 1998;114(2):311-8.

37. Reeder SB, Robson PM, Yu H, Shimakawa A, Hines CD, McKenzie CA, et al. Quantification of hepatic steatosis with MRI: the effects of accurate fat spectral modeling. Journal of Magnetic Resonance Imaging: An Official Journal of the International Society for Magnetic Resonance in Medicine. 2009;29(6):1332-9.

38. Reeder SB, McKenzie CA, Pineda AR, Yu H, Shimakawa A, Brau AC, et al. Water–fat separation with IDEAL gradient ‐ echo imaging. Journal of Magnetic Resonance Imaging: An Official Journal of the International Society for Magnetic Resonance in Medicine. 2007;25(3):644-52.

39. Hernando D, Haldar J, Sutton B, Ma J, Kellman P, Liang ZP. Joint estimation of water/fat images and field inhomogeneity map. Magnetic Resonance in Medicine: An Official Journal of the International Society for Magnetic Resonance in Medicine. 2008;59(3):571-80.

40. Zhong X, Nickel MD, Kannengiesser SA, Dale BM, Kiefer B, Bashir MR. Liver fat quantification using a multi-step adaptive fitting approach with multi-echo GRE imaging. Magn Reson Med. 2014;72(5):1353-65.

41. Hernando D, Kellman P, Haldar J, Liang ZP. Robust water/fat separation in the presence of large field inhomogeneities using a graph cut algorithm. Magnetic Resonance in Medicine: An Official Journal of the International Society for Magnetic Resonance in Medicine. 2010;63(1):79-90.

42. Yu H, McKenzie CA, Shimakawa A, Vu AT, Brau AC, Beatty PJ, et al. Multiecho reconstruction for simultaneous water‐fat decomposition and T2* estimation. Journal of Magnetic Resonance Imaging: An Official Journal of the International Society for Magnetic Resonance in Medicine. 2007;26(4):1153-61.

43. Bydder M, Yokoo T, Hamilton G, Middleton MS, Chavez AD, Schwimmer JB, et al. Relaxation effects in the quantification of fat using gradient echo imaging. Magnetic resonance imaging. 2008;26(3):347-59.

44. Deoni SC, Rutt BK, Peters TM. Rapid combined T1 and T2 mapping using gradient recalled acquisition in the steady state. Magnetic Resonance in Medicine: An Official Journal of the International Society for Magnetic Resonance in Medicine. 2003;49(3):515-26.

45. Ma D, Gulani V, Seiberlich N, Liu K, Sunshine JL, Duerk JL, et al. Magnetic resonance fingerprinting. Nature. 2013;495(7440):187-92.

46. Tropp JA, Gilbert AC. Signal recovery from random measurements via orthogonal matching pursuit. IEEE Transactions on information theory. 2007;53(12):4655-66.

47. Velasco C, Cruz G, Jaubert O, Lavin B, Botnar RM, Prieto C. Simultaneous comprehensive liver T1, T2, T1ρ, and fat fraction characterization with MR fingerprinting. Magnet Reson Med. 2022;87(4):1980-91.

48. Lima da Cruz GJ, Velasco C, Lavin B, Jaubert O, Botnar RM, Prieto C. Myocardial T1, T2, T2*, and fat fraction quantification via low ‐ rank motion ‐ corrected cardiac MR fingerprinting. Magnet Reson Med. 2022;87(6):2757-74.

49. Su P, Fan H, Liu P, Li Y, Qiao Y, Hua J, et al. MR fingerprinting ASL: Sequence characterization and comparison with dynamic susceptibility contrast (DSC) MRI. NMR in Biomedicine. 2020;33(1):e4202.

50. Cohen O, Huang S, McMahon MT, Rosen MS, Farrar CT. Rapid and quantitative chemical exchange saturation transfer (CEST) imaging with magnetic resonance fingerprinting (MRF). Magnet Reson Med. 2018;80(6):2449-63.

51. West DJ, Cruz G, Teixeira RP, Schneider T, Tournier JD, Hajnal JV, et al. An MR fingerprinting approach for quantitative inhomogeneous magnetization transfer imaging. Magnet Reson Med. 2022;87(1):220-35.

52. Jaubert O, Cruz G, Bustin A, Schneider T, Lavin B, Koken P, et al. Water–fat Dixon cardiac magnetic resonance fingerprinting. Magnet Reson Med. 2020;83(6):2107-23.

53. Yu Z, Zhao T, Assländer J, Lattanzi R, Sodickson DK, Cloos MA. Exploring the sensitivity of magnetic resonance fingerprinting to motion. Magnetic resonance imaging. 2018;54:241-8.

54. Cruz G, Jaubert O, Qi H, Bustin A, Milotta G, Schneider T, et al. 3D free ‐ breathing cardiac magnetic resonance fingerprinting. NMR in Biomedicine. 2020;33(10):e4370.

55. Hamilton JI, Jiang Y, Eck B, Griswold M, Seiberlich N. Cardiac cine magnetic resonance fingerprinting for combined ejection fraction, T-1 and T-2 quantification. Nmr in Biomedicine. 2020;33(8).

56. Jaubert O, Cruz G, Bustin A, Schneider T, Koken P, Doneva M, et al. Free-running cardiac magnetic resonance fingerprinting: Joint T1/T2 map and Cine imaging. Magnetic Resonance Imaging. 2020;68:173-82.

57. Krug J, Rose G, Stucht D, Clifford G, Oster J. Limitations of VCG based gating methods in ultra high field cardiac MRI. J Cardiovasc Magn R. 2013;15(1):1-2.

58. Akçakaya M, Weingärtner S, Basha TA, Roujol S, Bellm S, Nezafat R. Joint myocardial T1 and T2 mapping using a combination of saturation recovery and T2 ‐ preparation. Magnet Reson Med. 2016;76(3):888-96.

59. Kellman P, Xue H, Chow K, Howard J, Chacko L, Cole G, et al. Bright-blood and dark-blood phase sensitive inversion recovery late gadolinium enhancement and T1 and T2 maps in a single free-breathing scan: an all-in-one approach. J Cardiovasc Magn R. 2021;23(1):1-14.

60. Christodoulou AG, Shaw JL, Nguyen C, Yang Q, Xie Y, Wang N, et al. Magnetic resonance multitasking for motion-resolved quantitative cardiovascular imaging. Nat Biomed Eng. 2018;2(4):215-26.

61. Liang Z-P, editor Spatiotemporal imagingwith partially separable functions. 2007 4th IEEE International Symposium on Biomedical Imaging: From Nano to Macro; 2007: IEEE.

62. Tucker LR. Some mathematical notes on three-mode factor analysis. Psychometrika. 1966;31(3):279-311.

63. Kolda TG, Bader BW. Tensor Decompositions and Applications. Siam Rev. 2009;51(3):455-500.

64. Lescher S, Jurcoane A, Veit A, Bahr O, Deichmann R, Hattingen E. Quantitative T1 and T2 mapping in recurrent glioblastomas under bevacizumab: earlier detection of tumor progression compared to conventional MRI. Neuroradiology. 2015;57(1):11-20.

65. Steen RG, Hunte M, Traipe E, Hurh P, Wu S, Bilaniuk L, et al. Brain T1 in young children with sickle cell disease: evidence of early abnormalities in brain development. Magn Reson Imaging. 2004;22(3):299-306.

66. Vrenken H, Geurts JJG, Knol DL, van Dijk LN, Dattola V, Jasperse B, et al. Whole-brain T1 mapping in multiple sclerosis: Global changes of normal-appearing gray and white matter. Radiology. 2006;240(3):811-20.

67. Stevenson VL, Parker GJ, Barker GJ, Birnie K, Tofts PS, Miller DH, et al. Variations in T1 and T2 relaxation times of normal appearing white matter and lesions in multiple sclerosis. J Neurol Sci. 2000;178(2):81-7.

68. Baudrexel S, Nurnberger L, Rub U, Seifried C, Klein JC, Deller T, et al. Quantitative mapping of T1 and T2* discloses nigral and brainstem pathology in early Parkinson's disease. Neuroimage. 2010;51(2):512-20.

69. Barbosa JHO, Santos AC, Tumas V, Liu MJ, Zheng WL, Haacke EM, et al. Quantifying brain iron deposition in patients with Parkinson's disease using quantitative susceptibility mapping, R2 and R2. Magnetic Resonance Imaging. 2015;33(5):559-65.

70. Li X, Harrison DM, Liu H, Jones CK, Oh J, Calabresi PA, et al. Magnetic susceptibility contrast variations in multiple sclerosis lesions. J Magn Reson Imaging. 2016;43(2):463-73.

71. Helms G, Dathe H, Dechent P. Quantitative FLASH MRI at 3T using a rational approximation of the Ernst equation. Magn Reson Med. 2008;59(3):667-72.

72. Ben-Eliezer N, Sodickson DK, Block KT. Rapid and accurate T2 mapping from multi-spin-echo data using Bloch-simulation-based reconstruction. Magn Reson Med. 2015;73(2):809-17.

73. Betts MJ, Acosta-Cabronero J, Cardenas-Blanco A, Nestor PJ, Duzel E. High-resolution characterisation of the aging brain using simultaneous quantitative susceptibility mapping (QSM) and R-2* measurements at 7 T. Neuroimage. 2016;138:43-63.

74. Ghadery C, Pirpamer L, Hofer E, Langkammer C, Petrovic K, Loitfelder M, et al. R2*mapping for brain iron: associations with cognition in normal aging. Neurobiol Aging. 2015;36(2):925-32.

75. Feng X, Deistung A, Reichenbach JR. Quantitative susceptibility mapping (QSM) and R-2* in the human brain at 3 T Evaluation of intra-scanner repeatability. Z Med Phys. 2018;28(1):36-48.

76. Deichmann R, Good CD, Josephs O, Ashburner J, Turner R. Optimization of 3-D MP-RAGE sequences for structural brain imaging. Neuroimage. 2000;12(1):112-27.

77. Marques JP, Kober T, Krueger G, van der Zwaag W, Van de Moortele PF, Gruetter R. MP2RAGE, a self bias-field corrected sequence for improved segmentation and T1-mapping at high field. Neuroimage. 2010;49(2):1271-81.

78. Wang CY, Coppo S, Mehta BB, Seiberlich N, Yu X, Griswold MA. Magnetic resonance fingerprinting with quadratic RF phase for measurement of T-2* simultaneously with delta(f),T-1, and T-2. Magn Reson Med. 2019;81(3):1849-62.

79. Schweser F, Deistung A, Reichenbach JR. Foundations of MRI phase imaging and processing for Quantitative Susceptibility Mapping (QSM). Z Med Phys. 2016;26(1):6-34.

80. Wu DM, Liu SF, Buch S, Ye YQ, Dai YM, Haacke EM. A Fully Flow-Compensated Multiecho Susceptibility-Weighted Imaging Sequence: The Effects of Acceleration and Background Field on Flow Compensation. Magn Reson Med. 2016;76(2):478-89.

81. Xu B, Liu T, Spincemaille P, Prince M, Wang Y. Flow compensated quantitative susceptibility mapping for venous oxygenation imaging. Magn Reson Med. 2014;72(2):438-45.

82. Liang Z-P, editor Spatiotemporal imaging with partially separable functions. 2007 4th IEEE International Symposium on Biomedical Imaging: From Nano to Macro; 2007: IEEE.

83. He JF, Liu QG, Christodoulou AG, Ma C, Lam F, Liang ZP. Accelerated High-Dimensional MR Imaging With Sparse Sampling Using Low-Rank Tensors. Ieee T Med Imaging. 2016;35(9):2119-29.

84. De Lathauwer L, De Moor B, Vandewalle J. A multilinear singular value decomposition. Siam J Matrix Anal A. 2000;21(4):1253-78.

85. Abdul-Rahman HS, Gdeisat MA, Burton DR, Lalor MJ, Lilley F, Moore CJ. Fast and robust three-dimensional best path phase unwrapping algorithm. Appl Optics. 2007;46(26):6623-35.

86. Smith SM. Fast robust automated brain extraction. Hum Brain Mapp. 2002;17(3):143-55.

87. Schweser F, Deistung A, Lehr BW, Reichenbach JR. Quantitative imaging of intrinsic magnetic tissue properties using MRI signal phase: an approach to in vivo brain iron metabolism? Neuroimage. 2011;54(4):2789-807.

88. Haacke EM, Tang J, Neelavalli J, Cheng YCN. Susceptibility Mapping as a Means to Visualize Veins and Quantify Oxygen Saturation. Journal of Magnetic Resonance Imaging. 2010;32(3):663-76.

89. Tang J, Liu S, Neelavalli J, Cheng YCN, Buch S, Haacke EM. Improving Susceptibility Mapping Using a Threshold-Based K-Space/Image Domain Iterative Reconstruction Approach. Magn Reson Med. 2013;69(5):1396-407.

90. Gharabaghi S, Liu SF, Wang Y, Chen YS, Buch S, Jokar M, et al. Multi-Echo Quantitative Susceptibility Mapping for Strategically Acquired Gradient Echo (STAGE) Imaging. Front Neurosci-Switz. 2020;14.

91. Deoni SCL, Rutt BK, Peters TM. Rapid combined T-1 and T-2 mapping using gradient recalled acquisition in the steady state. Magn Reson Med. 2003;49(3):515-26.

92. Shi XF, Kim SE, Jeong EK. Single-Shot T-1 Mapping Using Simultaneous Acquisitions of Spin- and Stimulated-Echo-Planar Imaging (2D ss-SESTEPI). Magn Reson Med. 2010;64(3):734-42.

93. Knight MJ, McCann B, Tsivos D, Dillon S, Coulthard E, Kauppinen RA. Quantitative T2 mapping of white matter: applications for ageing and cognitive decline. Phys Med Biol. 2016;61(15):5587-605.

94. Hattingen E, Jurcoane A, Bahr O, Rieger J, Magerkurth J, Anti S, et al. Bevacizumab impairs oxidative energy metabolism and shows antitumoral effects in recurrent glioblastomas: a P-31/H-1 MRSI and quantitative magnetic resonance imaging study. Neuro-Oncology. 2011;13(12):1349-63.

95. Hilbert T, Sumpf TJ, Weiland E, Frahm J, Thiran JP, Meuli R, et al. Accelerated T-2 mapping combining parallel MRI and model-based reconstruction: GRAPPATINI. Journal of Magnetic Resonance Imaging. 2018;48(2):359-68.

96. Haacke EM, Xu Y, Cheng YC, Reichenbach JR. Susceptibility weighted imaging (SWI). Magn Reson Med. 2004;52(3):612-8.

97. Liu S, Mok K, Neelavalli J, Cheng YC, Tang J, Ye Y, et al. Improved MR venography using quantitative susceptibility-weighted imaging. J Magn Reson Imaging. 2014;40(3):698-708.

98. de Rochefort L, Brown R, Prince MR, Wang Y. Quantitative MR susceptibility mapping using piece-wise constant regularized inversion of the magnetic field. Magn Reson Med. 2008;60(4):1003-9.

99. Chu SC, Xu Y, Balschi JA, Springer CS, Jr. Bulk magnetic susceptibility shifts in NMR studies of compartmentalized samples: use of paramagnetic reagents. Magn Reson Med. 1990;13(2):239-62.

100. Deh K, Kawaji K, Bulk M, Van Der Weerd L, Lind E, Spincemaille P, et al. Multicenter reproducibility of quantitative susceptibility mapping in a gadolinium phantom using MEDI+0 automatic zero referencing. Magn Reson Med. 2019;81(2):1229-36.

101. Wansapura JP, Holland SK, Dunn RS, Ball WS. NMR relaxation times in the human brain at 3.0 tesla. Jmri-J Magn Reson Im. 1999;9(4):531-8.

102. Stanisz GJ, Odrobina EE, Pun J, Escaravage M, Graham SJ, Bronskill MJ, et al. T1, T2 relaxation and magnetization transfer in tissue at 3T. Magnetic Resonance in Medicine: An Official Journal of the International Society for Magnetic Resonance in Medicine. 2005;54(3):507-12.

103. Weiskopf N, Suckling J, Williams G, Correia MM, Inkster B, Tait R, et al. Quantitative multi-parameter mapping of R1, PD*, MT, and R2* at 3T: a multi-center validation. Front Neurosci-Switz. 2013;7:95.

104. Lu HZ, Nagae-Poetscher LM, Golay X, Lin D, Pomper M, van Zijl PCM. Routine clinical brain MRI sequences for use at 3.0 Tesla. Journal of Magnetic Resonance Imaging. 2005;22(1):13-22.

105. Wang XQ, Voit D, Roeloffs V, Uecker M, Frahm J. Fast Interleaved Multislice T1 Mapping: Model-Based Reconstruction of Single-Shot Inversion-Recovery Radial FLASH. Comput Math Method M. 2018;2018.

106. Gelman N, Ewing JR, Gorell JM, Spickler EM, Solomon EG. Interregional variation of longitudinal relaxation rates in human brain at 3.0 T: Relation to estimated iron and water contents. Magn Reson Med. 2001;45(1):71-9.

107. Gelman N, Gorell JM, Barker PB, Savage RM, Spickler EM, Windham JP, et al. MR imaging of human brain at 3.0 T: Preliminary report on transverse relaxation rates and relation to estimated iron content. Radiology. 1999;210(3):759-67.

108. Cicchetti DV. Guidelines, criteria, and rules of thumb for evaluating normed and standardized assessment instruments in psychology. Psychological assessment. 1994;6(4):284.

109. Lim IAL, Faria AV, Li X, Hsu JTC, Airan RD, Mori S, et al. Human brain atlas for automated region of interest selection in quantitative susceptibility mapping: Application to determine iron content in deep gray matter structures. Neuroimage. 2013;82:449-69.

110. Chai C, Yan S, Chu ZQ, Wang T, Wang LJ, Zhang MJ, et al. Quantitative measurement of brain iron deposition in patients with haemodialysis using susceptibility mapping. Metab Brain Dis. 2015;30(2):563-71.

111. He NY, Ling HW, Ding B, Huang J, Zhang Y, Zhang ZP, et al. Region-specific disturbed iron distribution in early idiopathic Parkinson's disease measured by quantitative susceptibility mapping. Human Brain Mapping. 2015;36(11):4407-20.

112. Kim D, Wisnowski JL, Nguyen CT, Haldar JP. Probing in Vivo Microstructure with T 1-T 2 Relaxation Correlation Spectroscopic Imaging. Proc IEEE Int Symp Biomed Imaging. 2018;2018:675-8.

113. Istratov AA, Vyvenko OF. Exponential analysis in physical phenomena. Rev Sci Instrum. 1999;70(2):1233-57.

114. Epstein CL, Schotland J. The bad truth about Laplace's transform. Siam Rev. 2008;50(3):504-20.

115. Kim D, Wisnowski JL, Nguyen CT, Haldar JP. Multidimensional correlation spectroscopic imaging of exponential decays: From theoretical principles to in vivo human applications. NMR Biomed. 2020;33(12):e4244.

116. Sati P, Oh J, Constable RT, Evangelou N, Guttmann CR, Henry RG, et al. The central vein sign and its clinical evaluation for the diagnosis of multiple sclerosis: a consensus statement from the North American Imaging in Multiple Sclerosis Cooperative. Nat Rev Neurol. 2016;12(12):714-22.

117. Ellingson BM, Bendszus M, Boxerman J, Barboriak D, Erickson BJ, Smits M, et al. Consensus recommendations for a standardized Brain Tumor Imaging Protocol in clinical trials. Neuro Oncol. 2015;17(9):1188-98.

118. Traboulsee A, Simon JH, Stone L, Fisher E, Jones DE, Malhotra A, et al. Revised Recommendations of the Consortium of MS Centers Task Force for a Standardized MRI Protocol and Clinical Guidelines for the Diagnosis and Follow-Up of Multiple Sclerosis. AJNR Am J Neuroradiol. 2016;37(3):394-401.

119. Zhu DC, Penn RD. Full‐brain T1 mapping through inversion recovery fast spin echo imaging with time‐efficient slice ordering. Magnetic Resonance in Medicine: An Official Journal of the International Society for Magnetic Resonance in Medicine. 2005;54(3):725-31.

120. Jiang Y, Ma D, Keenan KE, Stupic KF, Gulani V, Griswold MA. Repeatability of magnetic resonance fingerprinting T1 and T2 estimates assessed using the ISMRM/NIST MRI system phantom. Magn Reson Med. 2017;78(4):1452-7.

121. McPhee KC, Wilman AH. Limitations of skipping echoes for exponential T2 fitting. J Magn Reson Imaging. 2018;48(5):1432-40.

122. Wang K, Doneva M, Amthor T, Keil VC, Karasan E, Tan F, et al., editors. High Fidelity Direct-Contrast Synthesis from Magnetic Resonance Fingerprinting in Diagnostic Imaging. ISMRM; 2020; Paris2020.

123. Tanenbaum LN, Tsiouris AJ, Johnson AN, Naidich TP, DeLano MC, Melhem ER, et al. Synthetic MRI for Clinical Neuroimaging: Results of the Magnetic Resonance Image Compilation (MAGiC) Prospective, Multicenter, Multireader Trial. Am J Neuroradiol. 2017;38(6):1103-10.

124. Chen Y, Fang Z, Hung S-C, Chang W-T, Shen D, Lin W. High-resolution 3D MR Fingerprinting using parallel imaging and deep learning. NeuroImage. 2020;206:116329.

125. Kim TH, Setsompop K, Haldar JP. LORAKS Makes Better SENSE: Phase-Constrained Partial Fourier SENSE Reconstruction Without Phase Calibration. Magn Reson Med. 2017;77(3):1021-35.

126. Kustner T, Bustin A, Jaubert O, Hajhosseiny R, Masci PG, Neji R, et al. Isotropic 3D Cartesian single breath-hold CINE MRI with multi-bin patch-based low-rank reconstruction. Magn Reson Med. 2020;84(4):2018-33.

127. Pham CH, Tor-Diez C, Meunier H, Bednarek N, Fablet R, Passat N, et al. Multiscale brain MRI super-resolution using deep 3D convolutional networks. Comput Med Imag Grap. 2019;77.

128. Chen Y, Shi F, Christodoulou AG, Xie Y, Zhou Z, Li D, editors. Efficient and accurate MRI super-resolution using a generative adversarial network and 3D multi-level densely

connected network. International Conference on Medical Image Computing and Computer-Assisted Intervention; 2018: Springer.

129. Afacan O, Erem B, Roby DP, Roth N, Roth A, Prabhu SP, et al. Evaluation of motion and its effect on brain magnetic resonance image quality in children. Pediatr Radiol. 2016;46(12):1728-35.

130. Wang N, Christodoulou AG, Xie YB, Wang ZJ, Deng ZX, Zhou B, et al. Quantitative 3D dynamic contrast-enhanced (DCE) MR imaging of carotid vessel wall by fast T1 mapping using Multitasking. Magn Reson Med. 2019;81(4):2302-14.

131. Han P, Zhang R, Wagner S, Xie YB, Cingolani E, Marban E, et al. Electrocardiogram-less, free-breathing myocardial extracellular volume fraction mapping in small animals at high heart rates using motion-resolved cardiovascular magnetic reesonance multitasking: a feasibility study in a heart failure with preserved ejection fraction rat model. J Cardiovasc Magn R. 2021;23(1).

132. Hu ZH, Christodoulou AG, Wang N, Shaw JL, Song SS, Maya MM, et al. Magnetic resonance multitasking for multidimensional assessment of cardiovascular system: Development and feasibility study on the thoracic aorta. Magnet Reson Med. 2020;84(5):2376-88.

133. Messroghli DR, Moon JC, Ferreira VM, Grosse-Wortmann L, He T, Kellman P, et al. Clinical recommendations for cardiovascular magnetic resonance mapping of T1, T2, T2* and extracellular volume: A consensus statement by the Society for Cardiovascular Magnetic Resonance (SCMR) endorsed by the European Association for Cardiovascular Imaging (EACVI). J Cardiovasc Magn Reson. 2017;19(1):75.

134. Kim PK, Hong YJ, Im DJ, Suh YJ, Park CH, Kim JY, et al. Myocardial T1 and T2 Mapping: Techniques and Clinical Applications. Korean J Radiol. 2017;18(1):113-31.

135. Haaf P, Garg P, Messroghli DR, Broadbent DA, Greenwood JP, Plein S. Cardiac T1 Mapping and Extracellular Volume (ECV) in clinical practice: a comprehensive review. J Cardiovasc Magn Reson. 2016;18(1):89.

136. Puntmann VO, Voigt T, Chen Z, Mayr M, Karim R, Rhode K, et al. Native T1 mapping in differentiation of normal myocardium from diffuse disease in hypertrophic and dilated cardiomyopathy. JACC Cardiovasc Imaging. 2013;6(4):475-84.

137. Carpenter JP, Roughton M, Pennell DJ, Myocardial Iron in Thalassemia I. International survey of T2* cardiovascular magnetic resonance in beta-thalassemia major. Haematologica. 2013;98(9):1368-74.

138. Aydinok Y, Porter JB, Piga A, Elalfy M, El-Beshlawy A, Kilinc Y, et al. Prevalence and distribution of iron overload in patients with transfusion-dependent anemias differs across geographic regions: results from the CORDELIA study. Eur J Haematol. 2015;95(3):244-53.

139. Kenchaiah S, Ding J, Carr JJ, Allison MA, Budoff MJ, Tracy RP, et al. Pericardial Fat and the Risk of Heart Failure. J Am Coll Cardiol. 2021;77(21):2638-52.

140. Goldfarb JW, Roth M, Han J. Myocardial Fat Deposition after Left Ventricular Myocardial Infarction: Assessment by Using MR Water-Fat Separation Imaging. Radiology. 2009;253(1):65-73.

141. Messroghli DR, Radjenovic A, Kozerke S, Higgins DM, Sivananthan MU, Ridgway JP. Modified Look-Locker inversion recovery (MOLLI) for high-resolution T1 mapping of the heart. Magn Reson Med. 2004;52(1):141-6.

142. Chow K, Flewitt JA, Green JD, Pagano JJ, Friedrich MG, Thompson RB. Saturation recovery single-shot acquisition (SASHA) for myocardial T(1) mapping. Magn Reson Med. 2014;71(6):2082-95.

143. Giri S, Chung YC, Merchant A, Mihai G, Rajagopalan S, Raman SV, et al. T2 quantification for improved detection of myocardial edema. J Cardiovasc Magn Reson. 2009;11:56.

144. Hermann I, Kellman P, Demirel OB, Akcakaya M, Schad LR, Weingartner S. Free-breathing simultaneous T 1 , T 2 , and T 2 * quantification in the myocardium. Magn Reson Med. 2021;86(3):1226-40.

145. Cruz G, Jaubert O, Qi H, Bustin A, Milotta G, Schneider T, et al. 3D free-breathing cardiac magnetic resonance fingerprinting. NMR Biomed. 2020;33(10):e4370.

146. Qi H, Bustin A, Cruz G, Jaubert O, Chen H, Botnar RM, et al. Free-running simultaneous myocardial T1/T2 mapping and cine imaging with 3D whole-heart coverage and isotropic spatial resolution. Magn Reson Imaging. 2019;63:159-69.

147. Qi H, Jaubert O, Bustin A, Cruz G, Chen H, Botnar R, et al. Free-running 3D whole heart myocardial T1 mapping with isotropic spatial resolution. Magn Reson Med. 2019;82(4):1331-42.

148. Santelli C, Nezafat R, Goddu B, Manning WJ, Smink J, Kozerke S, et al. Respiratory bellows revisited for motion compensation: preliminary experience for cardiovascular MR. Magn Reson Med. 2011;65(4):1097-102.

149. Nacif MS, Zavodni A, Kawel N, Choi EY, Lima JA, Bluemke DA. Cardiac magnetic resonance imaging and its electrocardiographs (ECG): tips and tricks. Int J Cardiovasc Imaging. 2012;28(6):1465-75.

150. Shaw JL, Yang Q, Zhou ZW, Deng ZX, Nguyen C, Li DB, et al. Free-breathing, non-ECG, continuous myocardial T-1 mapping with cardiovascular magnetic resonance multitasking. Magn Reson Med. 2019;81(4):2450-63.

151. Cao T, Ma S, Wang N, Gharabaghi S, Xie Y, Fan Z, et al. Three-dimensional simultaneous brain mapping of T1, T2, T2* and magnetic susceptibility with MR Multitasking. Magn Reson Med. 2021.

152. Wang N, Cao T, Han F, Xie Y, Zhong X, Ma S, et al. Free-breathing multitasking multi-echo MRI for whole-liver water-specific T1, proton density fat fraction, and R2* quantification. Magn Reson Med. 2021.

153. Hernando D, Kellman P, Haldar JP, Liang ZP. Robust Water/Fat Separation in the Presence of Large Field Inhomogeneities Using a Graph Cut Algorithm. Magn Reson Med. 2010;63(1):79-90.

154. Liang Z-P. Spatiotemporal imaging with partially separable functions. Proc IEEE Int Symp Biomed Imaging. 2007:988-91.

155. He J, Liu Q, Christodoulou AG, Ma C, Lam F, Liang Z-P. Accelerated high-dimensional MR imaging with sparse sampling using low-rank tensors. IEEE Trans Med Imaging. 2016;35(9):2119-29.

156. Hu Z, Christodoulou AG, Wang N, Shaw JL, Song SS, Maya MM, et al. Magnetic resonance multitasking for multidimensional assessment of cardiovascular system: Development and feasibility study on the thoracic aorta. Magn Reson Med. 2020;84(5):2376-88.

157. Wang N, Gaddam S, Wang L, Xie Y, Fan Z, Yang W, et al. Six-dimensional quantitative DCE MR Multitasking of the entire abdomen: Method and application to pancreatic ductal adenocarcinoma. Magn Reson Med. 2020;84(2):928-48.

158. Cao T, Wang N, Kwan AC, Lee HL, Mao X, Xie Y, et al. Free‐breathing, non‐ECG, simultaneous myocardial T1, T2, T2*, and fat‐fraction mapping with motion‐resolved cardiovascular MR multitasking. Magn Reson Med. 2022;88(4):1748-63.

159. Yu HZ, Shimakawa A, McKenzie CA, Brodsky E, Brittain JH, Reeder SB. Multiecho Water-Fat Separation and Simultaneous R-2* Estimation With Multifrequency Fat Spectrum Modeling. Magn Reson Med. 2008;60(5):1122-34.

160. Liu CY, McKenzie CA, Yu H, Brittain JH, Reeder SB. Fat quantification with IDEAL gradient echo imaging: Correction of bias from T-1 and noise. Magn Reson Med. 2007;58(2):354-64.

161. Roy C, Slimani A, de Meester C, Amzulescu M, Pasquet A, Vancraeynest D, et al. Age and sex corrected normal reference values of T1, T2 T2* and ECV in healthy subjects at 3T CMR. J Cardiovasc Magn Reson. 2017;19(1):72.

162. Idilman IS, Aniktar H, Idilman R, Kabacam G, Savas B, Elhan A, et al. Hepatic steatosis: quantification by proton density fat fraction with MR imaging versus liver biopsy. Radiology. 2013;267(3):767-75.

163. Procter AJ, Sun JY, Malcolm PN, Toms AP. Measuring liver fat fraction with complex-based chemical shift MRI: the effect of simplified sampling protocols on accuracy. BMC Med Imaging. 2019;19(1):14.

164. Yu H, McKenzie CA, Shimakawa A, Vu AT, Brau AC, Beatty PJ, et al. Multiecho reconstruction for simultaneous water-fat decomposition and T2* estimation. J Magn Reson Imaging. 2007;26(4):1153-61.

165. Alam MH, Auger D, McGill LA, Smith GC, He T, Izgi C, et al. Comparison of 3 T and 1.5 T for T2* magnetic resonance of tissue iron. J Cardiovasc Magn Reson. 2016;18(1):40.

166. Cerqueira MD, Weissman NJ, Dilsizian V, Jacobs AK, Kaul S, Laskey WK, et al. Standardized myocardial segmentation and nomenclature for tomographic imaging of the heart -

A statement for healthcare professionals from the Cardiac Imaging Committee of the Council on Clinical Cardiology of the American Heart Association. Circulation. 2002;105(4):539-42.

167. da Cruz GJL, Velasco C, Lavin B, Jaubert O, Botnar RM, Prieto C. Myocardial T1, T2, T2*, and fat fraction quantification via low-rank motion-corrected cardiac MR fingerprinting. Magn Reson Med. 2022.

168. Sievers B, Wiesner M, Kiria N, Speiser U, Schoen S, Strasser RH. Influence of the trigger technique on ventricular function measurements using 3-Tesla magnetic resonance imaging: comparison of ECG versus pulse wave triggering. Acta Radiol. 2011;52(4):385-92.

169. Kellman P, Hansen MS. T1-mapping in the heart: accuracy and precision. J Cardiovasc Magn Reson. 2014;16:2.

170. Meloni A, Positano V, Keilberg P, De Marchi D, Pepe P, Zuccarelli A, et al. Feasibility, reproducibility, and reliability for the T*2 iron evaluation at 3 T in comparison with 1.5 T. Magn Reson Med. 2012;68(2):543-51.

171. Reeder SB, Faranesh AZ, Boxerman JL, McVeigh ER. In vivo measurement of T* 2 and field inhomogeneity maps in the human heart at 1.5 T. Magn Reson Med. 1998;39(6):988-98.

172. Fischer K, Yamaji K, Luescher S, Ueki Y, Jung B, von Tengg-Kobligk H, et al. Feasibility of cardiovascular magnetic resonance to detect oxygenation deficits in patients with multi-vessel coronary artery disease triggered by breathing maneuvers. J Cardiovasc Magn R. 2018;20.

173. Gottbircht M, Kramer CM, Salerno M. Native T1 and Extracellular Volume Measurements by Cardiac MRI in Healthy Adults: A Meta-Analysis. Radiology. 2019;290(2):317-26.

174. Liu CY, Redheuil A, Ouwerkerk R, Lima JA, Bluemke DA. Myocardial fat quantification in humans: Evaluation by two-point water-fat imaging and localized proton spectroscopy. Magn Reson Med. 2010;63(4):892-901.

175. von Knobelsdorff-Brenkenhoff F, Prothmann M, Dieringer MA, Wassmuth R, Greiser A, Schwenke C, et al. Myocardial T-1 and T-2 mapping at 3 T: reference values, influencing factors and implications. J Cardiovasc Magn R. 2013;15.

176. Puntmann VO, Peker E, Chandrashekhar Y, Nagel E. T1 Mapping in Characterizing Myocardial Disease A Comprehensive Review. Circ Res. 2016;119(2):277-99.

177. Messroghli DR, Niendorf T, Schulz-Menger J, Dietz R, Friedrich MG. T1 mapping in patients with acute myocardial infarction. J Cardiovasc Magn Reson. 2003;5(2):353-9.

178. Dastidar AG, Harries I, Pontecorboli G, Bruno VD, De Garate E, Moret C, et al. Native T1 mapping to detect extent of acute and chronic myocardial infarction: comparison with late gadolinium enhancement technique. Int J Cardiovas Imag. 2019;35(3):517-27.

179. Hinojar R, Varma N, Child N, Goodman B, Jabbour A, Yu CY, et al. T1 Mapping in Discrimination of Hypertrophic Phenotypes: Hypertensive Heart Disease and Hypertrophic Cardiomyopathy Findings From the International T1 Multicenter Cardiovascular Magnetic Resonance Study. Circ-Cardiovasc Imag. 2015;8(12).

180. Hinojar R, Puntmann VO. Native T1 in Discrimination of Acute and Convalescent Stages in Patients With Clinical Diagnosis of Myocarditis A Proposed Diagnostic Algorithm Using CMR. Jacc-Cardiovasc Imag. 2015;8(1):38-46.

181. Fontana M, Banypersad SM, Treibel TA, Maestrini V, Sado DM, White SK, et al. Native T1 Mapping in Transthyretin Amyloidosis. Jacc-Cardiovasc Imag. 2014;7(2):157-65.

182. Banypersad SM, Fontana M, Maestrini V, Sado DM, Captur G, Petrie A, et al. T1 mapping and survival in systemic light-chain amyloidosis. Eur Heart J. 2015;36(4):244-51.

183. Mao X, Lee H, Ma S, Hu Z, Han F, Xie Y, et al., editors. Simultaneous Multi-slice Cardiac MR Multitasking for Motion-Resolved, Non-ECG, Free-Breathing Joint T1-T2 Mapping. ISMRM & SMRT Annual Meeting & Exhibition; 2021; An Online Experiene.

184. Chen Y, Shi F, Christodoulou AG, Xie Y, Zhou Z, Li D. Efficient and accurate MRI super-resolution using a Generative Adversarial Network and 3D Multi-level Densely Connected Network. Med Image Comput Comput Assist Interv. 2018:91-9.

185. Chen Y, Shaw JL, Xie Y, Li D, Christodoulou AG. Deep learning within *a priori* temporal feature spaces for large-scale dynamic MR image reconstruction: Application to 5-D cardiac MR Multitasking. Med Image Comput Comput Assist Interv. 2019;11765:495-504.

186. Han H, Song AW, Truong TK. Integrated parallel reception, excitation, and shimming (iPRES). Magn Reson Med. 2013;70(1):241-7.

187. Feng L, Axel L, Chandarana H, Block KT, Sodickson DK, Otazo R. XD‐GRASP: golden‐angle radial MRI with reconstruction of extra motion‐state dimensions using compressed sensing. Magn Reson Med. 2016;75(2):775-88.

188. Cheng JY, Zhang T, Alley MT, Uecker M, Lustig M, Pauly JM, et al. Comprehensive multi-dimensional MRI for the simultaneous assessment of cardiopulmonary anatomy and physiology. Scientific reports. 2017;7(1):1-15.

189. Bustin A, Lima da Cruz G, Jaubert O, Lopez K, Botnar RM, Prieto C. High‐dimensionality undersampled patch‐based reconstruction (HD‐PROST) for accelerated multi‐contrast MRI. Magn Reson Med. 2019;81(6):3705-19.

190. Yaman B, Weingartner S, Kargas N, Sidiropoulos ND, Akcakaya M. Low-rank tensor models for improved multidimensional MRI: application to dynamic cardiac T1 mapping. Ieee T Comput Imag. 2020;6:194-207.

191. Lam F, Peng X, Liang Z-P. High-dimensional MR spatiospectral imaging by integrating physics-based modeling and data-driven machine learning: current progress and future directions. IEEE Signal Processing Magazine. 2023;40(2):101-15.

192. Lustig M, Donoho D, Pauly JM. Sparse MRI: The application of compressed sensing for rapid MR imaging. Magnetic Resonance in Medicine: An Official Journal of the International Society for Magnetic Resonance in Medicine. 2007;58(6):1182-95.

193. Ma C, Clifford B, Liu Y, Gu Y, Lam F, Yu X, et al. High‐resolution dynamic 31P‐MRSI using a low‐rank tensor model. Magn Reson Med. 2017;78(2):419-28.

194. Haldar JP, Liang Z-P, editors. Low-rank approximations for dynamic imaging. 2011 IEEE International Symposium on Biomedical Imaging: From Nano to Macro; 2011: IEEE.

195. Christodoulou AG, Hitchens TK, Wu YL, Ho C, Liang Z-P. Improved subspace estimation for low-rank model-based accelerated cardiac imaging. IEEE Transactions on Biomedical Engineering. 2014;61(9):2451-7.

196. Gandy S, Recht B, Yamada I. Tensor completion and low-n-rank tensor recovery via convex optimization. Inverse problems. 2011;27(2):025010.

197. Recht B, Fazel M, Parrilo PA. Guaranteed minimum-rank solutions of linear matrix equations via nuclear norm minimization. Siam Rev. 2010;52(3):471-501.

198. Fazel M, Hindi H, Boyd SP, editors. A rank minimization heuristic with application to minimum order system approximation. Proceedings of the 2001 American Control Conference(Cat No 01CH37148); 2001: IEEE.

199. Boyd S, Parikh N, Chu E, Peleato B, Eckstein J. Distributed optimization and statistical learning via the alternating direction method of multipliers. Foundations and Trends® in Machine learning. 2011;3(1):1-122.

200. Gribonval R, Schnass K. Dictionary identification—sparse matrix-factorization via $\ell_1 $-minimization. IEEE Transactions on Information Theory. 2010;56(7):3523-39.

201. Caiafa CF, Cichocki A. Multidimensional compressed sensing and their applications. Wiley Interdisciplinary Reviews: Data Mining and Knowledge Discovery. 2013;3(6):355-80.

202. Selesnick I. Penalty and shrinkage functions for sparse signal processing. Connexions. 2012;11.

203. Schönemann PH. A generalized solution of the orthogonal procrustes problem. Psychometrika. 1966;31(1):1-10.

204. Sidiropoulos ND, De Lathauwer L, Fu X, Huang K, Papalexakis EE, Faloutsos C. Tensor decomposition for signal processing and machine learning. IEEE Transactions on Signal Processing. 2017;65(13):3551-82.

205. Ravishankar S, Bresler Y. Efficient blind compressed sensing using sparsifying transforms with convergence guarantees and application to magnetic resonance imaging. SIAM Journal on Imaging Sciences. 2015;8(4):2519-57.

206. Lingala SG, Jacob M. Blind compressive sensing dynamic MRI. Ieee T Med Imaging. 2013;32(6):1132-45.

207. Deng ZX, Pang JN, Yang WS, Yue Y, Sharif B, Tuli R, et al. Four-dimensional MRI using three-dimensional radial sampling with respiratory self-gating to characterize temporal phase-resolved respiratory motion in the abdomen. Magn Reson Med. 2016;75(4):1574-85.

208. Rosenzweig S, Scholand N, Holme HCM, Uecker M. Cardiac and respiratory self-gating in radial MRI using an adapted singular spectrum analysis (SSA-FARY). Ieee T Med Imaging. 2020;39(10):3029-41.

209. Segars WP, Sturgeon G, Mendonca S, Grimes J, Tsui BM. 4D XCAT phantom for multimodality imaging research. Medical physics. 2010;37(9):4902-15.

210. Varela‐Mattatall G, Baron CA, Menon RS. Automatic determination of the regularization weighting for wavelet‐based compressed sensing MRI reconstructions. Magn Reson Med. 2021;86(3):1403-19.

211. Aharon M, Elad M, Bruckstein A. K-SVD: An algorithm for designing overcomplete dictionaries for sparse representation. IEEE Transactions on signal processing. 2006;54(11):4311-22.

212. Uecker M, Lai P, Murphy MJ, Virtue P, Elad M, Pauly JM, et al. ESPIRiT—an eigenvalue approach to autocalibrating parallel MRI: where SENSE meets GRAPPA. Magn Reson Med. 2014;71(3):990-1001.

213. Ng AC, Strudwick M, van der Geest RJ, Ng AC, Gillinder L, Goo SY, et al. Impact of epicardial adipose tissue, left ventricular myocardial fat content, and interstitial fibrosis on myocardial contractile function. Circulation: Cardiovascular Imaging. 2018;11(8):e007372.

214. Chahine Y, Askari-Atapour B, Kwan KT, Anderson CA, Macheret F, Afroze T, et al. Epicardial adipose tissue is associated with left atrial volume and fibrosis in patients with atrial fibrillation. Frontiers in Cardiovascular Medicine. 2022;9:1045730.

215. Ardissino M, McCracken C, Bard A, Antoniades C, Neubauer S, Harvey NC, et al. Pericardial adiposity is independently linked to adverse cardiovascular phenotypes: a CMR study

of 42 598 UK Biobank participants. European Heart Journal-Cardiovascular Imaging. 2022;23(11):1471-81.

216. Bonou M, Mavrogeni S, Kapelios CJ, Markousis-Mavrogenis G, Aggeli C, Cholongitas E, et al. Cardiac adiposity and arrhythmias: the role of imaging. Diagnostics. 2021;11(2):362.

217. Conte M, Petraglia L, Cabaro S, Valerio V, Poggio P, Pilato E, et al. Epicardial adipose tissue and cardiac arrhythmias: focus on atrial fibrillation. Frontiers in Cardiovascular Medicine. 2022;9:932262.

218. Clauss S, Bleyer C, Schuettler D, Tomsits P, Renner S, Klymiuk N, et al. Animal models of arrhythmia: classic electrophysiology to genetically modified large animals. Nature Reviews Cardiology. 2019;16(8):457-75.

219. Rutt BK, Lee DH. The impact of field strength on image quality in MRI. Journal of Magnetic Resonance Imaging. 1996;6(1):57-62.

220. Lee KJ, Lee HL, Hennig J, Leupold J. Use of simulated annealing for the design of multiple repetition time balanced steady‐state free precession imaging. Magn Reson Med. 2012;68(1):220-6.

221. Ma D, Gulani V, Seiberlich N, Liu K, Sunshine JL, Duerk JL, et al. Magnetic resonance fingerprinting. Nature. 2013;495(7440):187-92.

222. Meloni A, Martini N, Positano V, D'Angelo G, Barison A, Todiere G, et al. Myocardial T1 Values at 1.5 T: Normal Values for General Electric Scanners and Sex‐Related Differences. Journal of Magnetic Resonance Imaging. 2021;54(5):1486-500.

223. Hanson CA, Kamath A, Gottbrecht M, Ibrahim S, Salerno M. T2 relaxation times at cardiac MRI in healthy adults: a systematic review and meta-analysis. Radiology. 2020;297(2):344-51.

224. Haldar JP, Hernando D. Rank-constrained solutions to linear matrix equations using powerfactorization. IEEE Signal Processing Letters. 2009;16(7):584-7.